NUMERICAL SHOCK PROPAGATION USING GEOMETRICAL SHOCK DYNAMICS

Thesis by
Donald William Schwendeman

In Partial Fulfillment of the Requirements

for the Degree of

Doctor of Philosophy

California Institute of Technology

Pasadena, California

1986

(Submitted April 30, 1986)

Acknowledgments

I would like to thank my advisor, Professor G. B. Whitham, for his helpful advice and for many useful discussions concerning the work presented in this thesis. As a result, the work has been enjoyable and I have learned a great deal. I would also like to thank the faculty, fellow students and secretaries of the Applied Mathematics Department. Their friendship has made my stay at Caltech both interesting and enjoyable. A special note of thanks is due to Professor H. B. Keller for his original support and to Bill Henshaw and Noel Smyth for their contributions to this work.

Financial support for my graduate study has been generously provided by Caltech through teaching assistantships and institute fellowships. Additional support has been given by the Department of Energy under contract DE-AM03-76SR00767 and by the Office of Naval Research under contract N00014-75-C-0702 through research assistantships. The calculations in this thesis were performed on the Caltech Applied Mathematics IBM 4341 computer. This thesis was typeset in TEX on the IBM 4341 and printed on the HP TEX system.

My deepest thanks go to my loving wife, Claudia, for her caring support over the years. I would also like to thank my family and especially my parents, who have always encouraged me to seek the best in myself.

Abstract

Various numerical schemes are developed to calculate the motion of shock waves in gases based on Whitham's theory of geometrical shock dynamics. The basic numerical scheme is used to study the propagation of two-dimensional shock waves along walls and in channels, and the self-focusing of initially curved shock-fronts. This scheme is extended to treat shock wave motion in non-uniform media. The extended scheme is used to examine shock wave refraction at both planar and curved interfaces separating gases with different properties. Precursor-irregular refraction patterns are obtained using geometrical shock dynamics. A general numerical scheme designed to propagate a shock surface in three dimensions is presented. Three-dimensional shock focusing and shock propagation in a curved pipe are considered primarily to demonstrate the use of the three-dimensional numerical scheme. The reflection of planar shock waves from curved walls is studied. The motion of the shock is determined using the combined theories of regular reflection and geometrical shock dynamics. A numerical scheme based on the combined theories is discussed. The numerical scheme is used to calculate the reflection and subsequent focusing of weak planar shock waves. Some of the present results are compared with other solutions to the equations of geometrical shock dynamics obtained using different methods. Recent experimental investigations are discussed and compared with our results calculated using geometrical shock dynamics.

Table of Contents

List of Figures and Tables

Chapter 2. Two-dimensional Shock Propagation

Chapter 3. Shock Propagation in Non-uniform Media

Chapter 4. Three-dimensional Shock Propagation

Chapter 5. Reflection of a Planar Shock Wave

CHAPTER 1

Overview

The numerical solution of hyperbolic differential equations and the associated problem of numerical shock fitting has received much attention in the recent literature. The main numerical difficulties in their solution lie in the method of fitting the shock and in the fact that the exact determination of the motion of the shock requires the calculation of the whole flow field behind the shock. In many problems, one is most interested in the motion of the shock and not the details of the flow field. Also, most of the numerical work has dealt with smooth shocks, leaving open the more difficult problem of situations in which the shock becomes non-smooth, as in Mach reflection.

In the present work, we are interested in the numerical propagation of shock waves in gases. Rather than solve the gas dynamic equations directly, we determine the motion of the shock, using the approximate theory of geometrical shock dynamics, as developed by Whitham [1957, 1958, 1959]. By the use of this approximate theory, the motion of the shock can be determined without explicitly calculating the flow field behind. The coupling with the flow field behind the shock is incorporated in the analytic formulation of the shock propagation equations, which are then solved numerically. Furthermore, the equations of geometrical shock dynamics are nonlinear and hyberbolic; thus, discontinuities in the shockfront appear naturally as shock-shocks. The presence of shock-shocks is significant in that they signal the formation of a Mach stem and reflected shock for the actual shock, the shock-shock being the position of the triple-point.

We begin with a brief review of the theory of geometrical shock dynamics in the first part of Chapter 2. Next, we discuss the basic numerical scheme developed to calculate the motion of shock waves in two space dimensions. In the last part of Chapter 2, we present numerical results for three fundamental shock propagation problems. These problems are (a) shock wave diffraction, (b) shock wave propagation in channels and (c) shock wave focusing. For all problems presented in Chapter 2, it is assumed that the gas ahead of the shock is uniform. The three problems are motivated primarily by theoretical and experimental results obtained by other investigators for the same problems. By comparing our numerical results found using geometrical shock dynamics with the experimental results, we are able to assess the accuracy of the approximate theory. In general, we find that geometrical shock dynamics predicts the motion of the actual shock with good accuracy in each case.

We acknowledge the earlier work of W. D. Henshaw and N. F. Smyth. The former developed the first numerical scheme and both considered some of the applications discussed in Chapter 2. These results were all improved and the numerical scheme was refined in various ways by the present author. Then, the further applications to the full range of problems in Chapter 2 were made. These combined results will appear in Henshaw et al. [1986]. The work reported in Chapters 3, 4 and 5 concerns completely new developments for shock wave propagation. The problems considered in these chapters are shock wave motion in non-uniform media and in three dimensions and shock wave reflection from a curved wall.

Shock wave propagation in non-uniform media is discussed in Chapter 3. Numerically, the extension to non-uniform media affects only the calculation of the local shock velocity. For a uniform medium, the local velocity (or Mach number) is related to the local expansion or compression along the shockfront by the so-called

A-M relation. The generalized A-M relation for non-uniform media contains additional terms representing the fluid non-uniformities ahead of the moving shock. The numerical treatment of these additional terms in the A-M relation is incorporated into the basic numerical scheme introduced in Chapter 2. We illustrate the effect of a non-uniform medium ahead of the moving shock by considering two shock refraction problems in the last part of Chapter 3.

The general problem of the shock wave propagation in three space dimensions is examined in Chapter 4. In this case, we are interested in the motion of the shockfront surface as opposed to the shockfront curve. A numerical scheme designed to propagate the shock surface is described in the first part of Chapter 4. This scheme is analogous to the basic numerical scheme presented in Chapter 2. However, the details of its implementation are new and in general more complicated than the basic numerical scheme. In particular, the mesh refinement on the shock surface is more difficult. In order to demonstrate the use of the general numerical scheme, we calculate the shockfront surfaces for two specific problems. We consider shock wave focusing in three dimensions and shock wave propagation around a 90° bend in a pipe with a circular cross section. These two problems provide a good test of the numerical scheme and show interesting shock wave propagation processes not seen in the two-dimensional problems.

In Chapter 5, we consider planar shock wave reflection by a curved wall. This problem requires an additional method for treating the reflection process at the reflector. We use the theory of regular reflection to obtain boundary conditions at the reflector surface. A modified A-M relation is introduced in order to incorporate the boundary conditions at the reflector surface into the approximate theory of geometrical shock dynamics. The combined theory is described is the first part of Chapter 5. Next, we discuss the modifications in the two-dimensional numerical scheme required to calculate the motion of the shock for this problem.

The specific problem of planar shock wave reflection from a parabolic reflector is examined in the end of Chapter 5. We calculate the reflected shock and subsequent focusing for *weak* shocks primarily. These results may be compared with extensive experimental results for the same problem. The comparison for weak shocks is particularly interesting since there was some earlier indication that shock dynamics may not be at its best for weak shocks. The focusing mechanisms for weak shocks are particularly complicated. Consequently, this case is an extreme test for any simple approximate theory. Accordingly, any deficiencies found in the application to weak shock problems would not necessarily be true the stronger range. In fact, we find that geometrical shock dynamics approximates the focusing of weak shocks with surprising overall accuracy.

An important simplification in geometrical shock dynamics is that the shockfront can be calculated directly without explicit knowledge of the flow field behind the shock. Numerically, this implies that only $O(N)$ operations (e.g., multiplications) are required at each time step to propagate a shockfront in *two dimensions*, where $1/N$ is average point spacing along the shockfront. A numerical scheme which determines the shocks from a calculation of the entire two-dimensional flow field would require at least $O(N^2)$ operations per time step to gain the same shockfront resolution. These two-dimensional flow calculations are possible but time-consuming given the current state of computing machines. For *three-dimensional* shock propagation, we require $O(N^2)$ operations per time step. These calculations are also time-consuming but possible, whereas the corresponding calculations for the entire three-dimensional flow field are not possible (again given the present available computers).

Another computational difficulty for entire flow calculations involves the determination of the shocks. One method proposed by Glimm et al. [1981] and Chern et al. [1986] tracks the shocks as an independent computational element

separate from the computation of the flow field away from the shocks. The smooth solution in the region away from the shocks can be calculated on a coarse grid. We point out this particular method since it provides an interesting comparison with the present numerical method for geometrical shock dynamics. Both methods track the shockfront. However, the motion of the shockfront is determined differently. The dynamics of the shockfront for front tracking is determined with the aid of the flow solution calculated on the coarse grid, whereas the dynamics of the shockfront for geometrical shock dynamics is specified by the A-M relation. Of course, it should be stressed that Glimm's front tracking method calculates exact solutions to the equations of gas dynamics (apart from numerical errors) and geometrical shock dynamics is a method for obtaining the shocks approximately with the possibility of handling much more complicated cases.

Finally, we note that the method of geometrical shock dynamics is not limited to shock waves and can be used for the propagation of any wavefront for which there is a known relation between the local speed of propagation and the local amplitude. For example, Miles [1977] applied geometrical shock dynamics to the propagation of a soliton around corners. The numerical method presented here can also be used for these problems.

CHAPTER 2

Two-dimensional Shock Propagation

2.1 Introduction

We first study shock wave propagation in two space dimensions. The motion of the shock will be determined using the approximate theory of geometrical shock dynamics as originally presented in Whitham [1957]. This theory provides a method of calculating the motion of the shock without explicit knowledge of the flow behind the shock. We discuss briefly the main elements of the approximate theory of geometrical shock dynamics in section 2.2. This serves as a useful introduction to the theory and gives the basis for the numerical scheme developed later.

Geometrical shock dynamics propagates a shock along rays normal to the shockfront with the local speed of propagation depending on the local Mach number. This local Mach number, in turn, depends on the local area of the ray tube. Numerically, this procedure is performed by representing the shockfront by a discrete set of points and propagating each point along approximate normals with a speed determined by the discrete area-Mach number relation. In expansive regions of the shockfront, points are automatically inserted to maintain a good shockfront resolution. Shock-shocks are fitted in compressive regions of the shockfront by deleting points. A smoothing scheme is added to dampen high frequency numerical fluctuations in the shockfront. The overall procedure is performed rapidly

with good accuracy for a wide variety of problems. The details of this numerical scheme are presented in section 2.3.

All the calculations in the present work use the area-Mach number relation that was developed for the case of an ideal gas with constant specific heats. However, other equations of state could be incorporated by changing to an appropriate area-Mach number relation. For these cases, the main numerical scheme would remain the same.

In section 2.4, we compare results obtained using our numerical scheme with exact and numerical solutions and experimental data. We consider the following three fundamental shock propagation problems: (a) shock wave diffraction, (b) shock wave propagation in channels and (c) shock wave focusing.

Exact solutions using geometrical shock dynamics were found by Whitham for some shock wave diffraction problems. Results calculated numerically are compared with these exact solutions. Bryson & Gross [1961] obtained numerical and experimental results for shock wave diffraction by cones, cylinders and spheres. Their numerical results used the method of characteristics in contrast to the numerical scheme developed in section 2.3. Shockfronts calculated using our numerical scheme are compared with these results as well.

Edwards, Fearnley & Nettleton [1983] experimentally studied the propagation of initially plane shock waves in channels with a 90° circular bend. Results were obtained for the Mach number on the convex and concave walls and a description of the shock geometry was discussed. We compare our numerical calculations with their results.

Sturtevant & Kulkarny [1976] experimentally determined the behavior of focusing weak shock waves by reflecting plane shock waves from a concave wall. Depending on the initial Mach number and curvature of the wall, the shock either

focused to form a crossed and folded front similar to that which occurs for geometrical acoustics or the shock remained uncrossed. We find the approximate theory of geometrical shock dynamics is able to predict this observation with reasonable accuracy. We also compare the Mach number (and thus the pressure jump) of the focusing shockfronts with the experimental data.

2.2 Geometrical Shock Dynamics

Whitham [1957, 1958, 1959] developed an approximate theory for shock propagation analagous to geometrical acoustics. In this theory, called *geometrical shock dynamics*, the shock propagates on rays normal to the shockfront, with the speed of propagation depending on the local compression or expansion along the shock. This theory is summarized in Whitham [1974].

(a) The A-M relation

For shock propagation in a uniform medium, Whitham shows that the local Mach number and ray tube area are related by

$$\frac{A}{A_0} = \frac{f(M)}{f(M_0)}, \tag{2.2.1}$$

where M_0 and A_0 are the initial Mach number and ray tube area, respectively. In the case of an ideal gas with constant specific heats, the function $f(M)$ is taken to be

$$f(M) = \exp\left(-\int \frac{M\,\lambda(M)}{M^2-1}\,dM\right), \tag{2.2.2}$$

where

$$\lambda(M) = \left(1 + \frac{2}{\gamma+1}\frac{1-\mu^2}{\mu}\right)\left(1 + 2\mu + \frac{1}{M^2}\right),$$

$$\mu^2 = \frac{(\gamma-1)M^2+2}{2\gamma M^2-(\gamma-1)},$$

γ being the ratio of specific heats (= 1.4 for air). We refer to equation (2.2.1) as the *A-M relation.* The integral in expression (2.2.2) may be evaluated explicitly. However, a numerical evaluation is more convenient. Approximations to (2.2.2) may also be obtained in the limits of weak and strong shocks. For weak shocks

$$f(M) = (M-1)^{-2} \qquad \text{as } M \to 1, \tag{2.2.3}$$

and for strong shocks

$$f(M) = M^{-n} \qquad \text{as } M \to \infty, \tag{2.2.4}$$

where $n = 1 + \frac{2}{\gamma} + \sqrt{\frac{2\gamma}{\gamma-1}} = 5.0743$ for $\gamma = 1.4$.

Whitham's *characteristic rule* applied to the one-dimensional formulation for flow in a channel with slowly varying cross-sectional area $A(x)$ provides the simplest derivation of the A-M relation. It is assumed that a shock is traveling down the channel with a Mach number $M(x)$. The exact nonlinear differential relation that holds on the C_+ characteristic is given by

$$\frac{dp}{dx} + \rho u \frac{du}{dx} + \frac{\rho a^2 u}{u+a} \frac{1}{A} \frac{dA}{dx} = 0, \tag{2.2.5}$$

where p, ρ, u and a $(= \sqrt{\gamma p/\rho})$ are the pressure, density, velocity and local sound speed, respectively. At the moving shock, the quantities p, ρ, u and a are eliminated from (2.2.5) in favor of M using the normal shock conditions. This procedure results in a differential relation between A and M at the shock, which is given by

$$\frac{M\lambda(M)}{M^2-1} \frac{dM}{dx} + \frac{1}{A} \frac{dA}{dx} = 0. \tag{2.2.6}$$

We may then integrate (2.2.6) to obtain the A-M relation (2.2.1).

The A-M relation given by (2.2.1) holds for a uniform medium ahead of the propagating shock. It is also possible to obtain a more general A-M relation for non-uniform media. In this case, we assume that the shock is propagating into a

prescribed equilibrium distribution of $p_0(x)$, $\rho_0(x)$, $a_0(x)$ and $\gamma(x)$. A body force is required to maintain an equilibrium variation in pressure. This requirement gives

$$\frac{1}{\rho_0}\frac{dp_0}{dx} = \mathcal{F}, \tag{2.2.7}$$

where $\mathcal{F}$ is an acceleration due to some body force (gravity, for example). With the added body force, the differential relation that holds on the C_+ becomes

$$\frac{dp}{dx} + \rho u\frac{du}{dx} + \frac{\rho a^2 u}{u+a}\frac{1}{A}\frac{dA}{dx} = \frac{\rho a}{u+a}\mathcal{F}. \tag{2.2.8}$$

We can eliminate $\mathcal{F}$ using (2.2.7), which gives

$$\frac{dp}{dx} + \rho u\frac{du}{dx} + \frac{\rho a^2 u}{u+a}\frac{1}{A}\frac{dA}{dx} = \frac{a}{u+a}\frac{\rho}{\rho_0}\frac{dp_0}{dx}. \tag{2.2.9}$$

Substituting the normal shock conditions into (2.2.9) results in a differential relation of the form

$$\frac{M\lambda(M,x)}{M^2-1}\frac{dM}{dx} + \frac{1}{A}\frac{dA}{dx} = S(M,x), \tag{2.2.10}$$

where $S(M,x)$ is a source term which contains the gradients of the fluid non-uniformities. Specifically, we have

$$S(M,x) = -g(M,x)\frac{1}{a_0}\frac{da_0}{dx} - h(M,x)\frac{1}{p_0}\frac{dp_0}{dx} - k(M,x)\frac{d\gamma}{dx}, \tag{2.2.11}$$

where

$$g(M,x) = 1 + \frac{2\mu(M^2-1)}{(\gamma-1)M^2+2},$$

$$h(M,x) = \frac{1}{2\gamma(M^2-1)}\left(2(M^2-1) + \mu\big(2\gamma M^2 - (\gamma-1)\big) - \frac{(\gamma+1)^2\mu M^2}{(\gamma-1)M^2+2}\right),$$

$$k(M,x) = \frac{g(M,x)}{\gamma(\gamma+1)}(\mu-\gamma).$$

The differential form of the A-M relation given by (2.2.10) for non-uniform media is the same relation as that reported by Catherasoo & Sturtevant [1983]. A relation of the same form was also obtained by Collins & Chen [1971], but there

is some difference in the coefficients. In Chapter 3, we use a discrete version of (2.2.10) as part of a numerical scheme to calculate the motion of shock waves in non-uniform media.

(b) Two-dimensional formulation

We shall first deal with two-dimensional motion, primarily. Three-dimensional problems are examined in Chapter 4. The two-dimensional formulation may be extended to axisymmetric motion without much change and we treat some of these cases also.

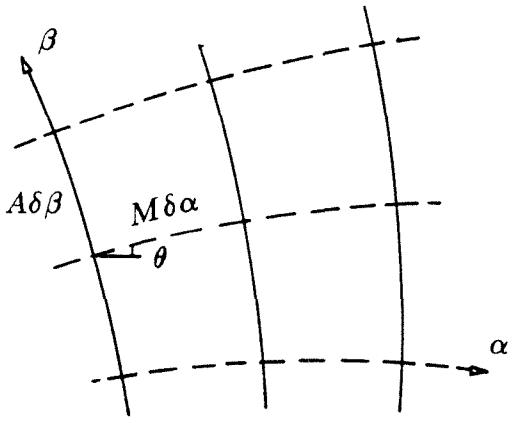

FIGURE 2.1. Coordinate system (α, β). Shock positions given by α = constant (solid lines) and rays given by β = constant (dashed lines).

In two dimensions, it is convenient to introduce an orthogonal curvilinear coordinate system (α, β) where successive shock positions are described by curves α = constant and rays by β = constant (figure 2.1). The shockfront is described by its local Mach number $M(\alpha, \beta)$ and its ray inclination angle $\theta(\alpha, \beta)$ referenced

to a fixed direction, the x-axis, say. It follows from a geometrical argument that the system of equations describing the propagation of the shockfront is

$$\begin{aligned} \frac{\partial \theta}{\partial \beta} - \frac{A'(M)}{M}\frac{\partial M}{\partial \alpha} &= 0, \\ \frac{\partial \theta}{\partial \alpha} + \frac{1}{A(M)}\frac{\partial M}{\partial \beta} &= 0, \end{aligned} \tag{2.2.12}$$

where a uniform medium is assumed so that $A = A(M)$ is given by (2.2.1). The characteristic form of (2.2.12) is

$$\left(\frac{\partial}{\partial \alpha} \pm c\,\frac{\partial}{\partial \beta}\right)\left(\theta \pm \omega(M)\right) = 0, \tag{2.2.13}$$

where

$$c^2(M) = -\frac{M}{A\,A'} = \frac{1}{A^2}\left(\frac{M^2-1}{\lambda}\right),$$

$$\omega(M) = \int_1^M \frac{dM}{A\,c} = \int_1^M \left(\frac{\lambda(M)}{M^2-1}\right)^{1/2} dM.$$

Therefore,

$$\theta \pm \omega(M) = \text{constant on characteristics } C_\pm \;:\; \frac{d\beta}{d\alpha} = \pm c. \tag{2.2.14}$$

The characteristics defined by $C_\pm$ in (2.2.14) are curves on which information (θ and M) propagates along the shock. These curves are not to be confused with the characteristic curve C_+ used in the derivation of the A-M relation.

(c) Shock-shocks

The system (2.2.12) is hyperbolic and represents a wave motion for disturbances propagating on the shock. Since this system of equations is hyperbolic and nonlinear, the shockfronts can develop discontinuities in slope and Mach number, these being called *shock-shocks*. Shock-shocks correspond physically to the formation of Mach stems, the shock-shock discontinuity being the position of the

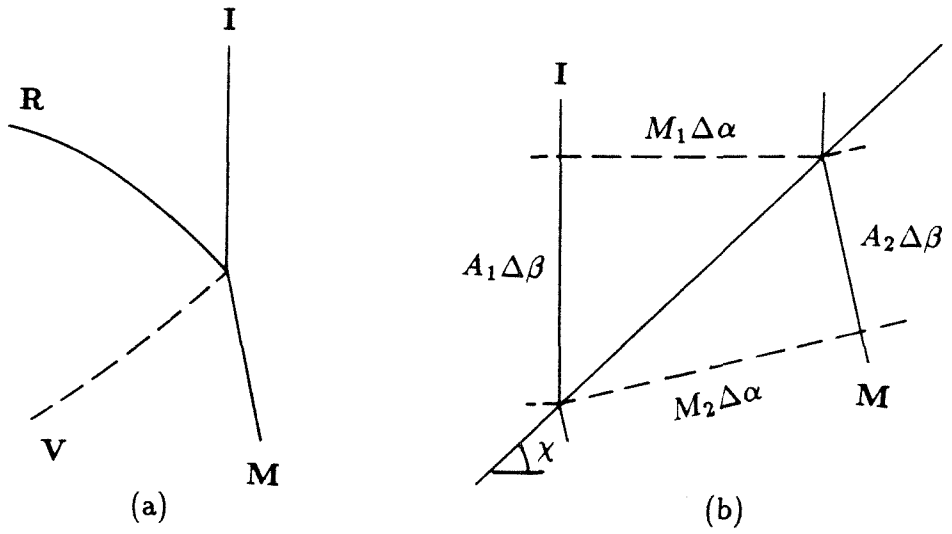

FIGURE 2.2. (a) Mach reflection : incident shock **I**, Mach stem **M**, reflected shock **R** and vortex sheet **V**. (b) Shock-shock geometry.

triple-point. In Mach reflection there is also a reflected shock **R** and a vortex sheet **V** as shown in figure 2.2a, but they do not appear explicitly in geometrical shock dynamics. Only the leading fronts appear as in figure 2.2b. The change in direction and Mach number at the shock-shock implies their existence.

In the case where a shock-shock develops, it is possible to treat the shock-shock as a discontinuity in M and θ. Given the shock-shock geometry in figure 2.2b, the following two geometric relations must hold:

$$\tan(\theta_2 - \theta_1) = \frac{\left(M_2^2 - M_1^2\right)^{1/2}\left(A_1^2 - A_2^2\right)^{1/2}}{A_2\, M_2 + A_1\, M_1}, \tag{2.2.15}$$

$$\tan\left(\chi - \theta_i\right) = \frac{A_i}{M_i}\left(\frac{M_2^2 - M_1^2}{A_1^2 - A_2^2}\right)^{1/2}, \qquad i = 1 \text{ or } 2. \tag{2.2.16}$$

Equations (2.2.15) and (2.2.16) relate the Mach number, ray tube area and ray inclination angle ahead of the shock-shock (state 1) with the the conditions behind (state 2) in terms of χ, the angle of the shock-shock line with the x-axis.

It is convenient to assume that the A-M relation still holds even for the abrupt change in Mach number and ray tube area at the shock-shock. This assumption is reasonable for moderate shock-shocks where the change in Mach number and ray tube area is not too large. For strong shock-shocks, the dependence of A_2 on M_2 in (2.2.15) and (2.2.16) may not be accurately given by the A-M relation, since the relation was derived assuming a gradual change in ray tube area. It is possible to obtain an alternate relationship between A and M across the shock-shock based on a three-shock geometry, where we now include the reflected shock **R** (as in figure 2.2a). However, this is an added complication which does not appear to be worthwhile in view of the overall approximate theory.

The characteristic solution (2.2.14) along with jump conditions (2.2.15) and (2.2.16) may be used to construct solutions in some simple cases. Solutions found in this manner are completely analagous to solutions found in one-dimensional gas dynamics or shallow water waves, for example. Later, the accuracy of the approximate solution obtained numerically will be checked with some of these exact solutions.

2.3 Basic Numerical Scheme

In this section, we present the basic numerical scheme developed to calculate successive shockfronts using the theory of geometrical shock dynamics. The scheme is advantageous in its simplicity and its application to a wide variety of problems. The simplicity of the scheme will become clear shortly. Later, we will apply the numerical procedure to calculate shocks for many cases.

The numerical procedure is basically a leap-frog time marching scheme. A sketch of the time marching scheme is provided in figure 2.3. The shockfront is given by a discrete set of points. Each point is advanced along its normal with a speed specified by the discrete version of the A-M relation. In expansive regions

of the shockfront, we insert points in order to maintain an approximately uniform point distribution. In compressive regions, we fit shock-shocks into the front by deleting points. A smoothing procedure is employed to dampen high frequency numerical errors in the shockfront position.

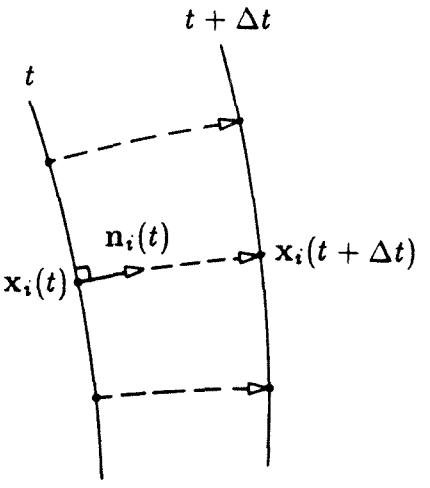

FIGURE 2.3. Basic time marching scheme. Shockfront positions at t and $t + \Delta t$ (solid lines) and approximate rays (dashed lines).

The numerical scheme is based on an approximate integration along rays. On a ray

$$\frac{\partial x}{\partial \alpha} = M \cos\theta \qquad \text{and} \qquad \frac{\partial y}{\partial \alpha} = M \sin\theta. \tag{2.3.1}$$

We write (2.3.1) in vector form and eliminate α in favor of time t using $\alpha = a_0 t$ where a_0 is some undisturbed sound speed. Then (2.3.1) become

$$\frac{\partial}{\partial t}\mathbf{x}(\beta, t) = a_0 M(\beta, t)\,\mathbf{n}(\beta, t), \tag{2.3.2}$$

where $\mathbf{x} = (x, y)$ is the shockfront position and $\mathbf{n} = (\cos\theta, \sin\theta)$ is the normal to the shockfront.

We approximate the shockfront position by a discrete set of points $\mathbf{x}_j(t)$, $j = 1, \ldots, N$. Let $M_i(t)$ and $\mathbf{n}_i(t)$ approximate the Mach number and shockfront normal at $\mathbf{x}_i(t)$, respectively. Then (2.3.2) becomes

$$\frac{d}{dt}\,\mathbf{x}_i(t) = M_i(t)\,\mathbf{n}_i(t), \qquad i = 1, \ldots, N, \tag{2.3.3}$$

where we set $a_0 = 1$ in all the calculations for this chapter. System (2.3.3) is a nonlinear system of O.D.E.'s and may be numerically integrated in a number of ways. We choose to use a two-step leap-frog scheme

$$\mathbf{x}_i(t + \Delta t) = \mathbf{x}_i(t - \Delta t) + 2\Delta t\, M_i(t)\,\mathbf{n}_i(t), \qquad i = 1, \ldots, N, \tag{2.3.4}$$

where $t = n\Delta t$, $n = 0, \ldots, T/\Delta t$. Scheme (2.3.4) is explicit and second-order accurate in time. Furthermore, leap-frog adds no numerical dissipation which is a desirable property since system (2.3.2) is hyperbolic.

The Mach number $M_i(t)$ in (2.3.4) is found by solving the approximate A-M relation

$$\frac{A_i(t)}{A_i(0)} = \frac{f\big(M_i(t)\big)}{f\big(M_i(0)\big)} \qquad \text{for } i = 1, \ldots, N. \tag{2.3.5}$$

Inverting the function $f(M)$ gives

$$M_i(t) = f^{-1}\left(f\big(M_i(0)\big)\,\frac{A_i(t)}{A_i(0)}\right), \qquad \text{for } i = 1, \ldots, N. \tag{2.3.6}$$

The inverse function f^{-1} may be found explicity in the limit of weak shocks (2.2.3) or strong shocks (2.2.4); however, we solve (2.3.6) numerically in general. The approximate area $A_i(t)$ in equation (2.3.6) is given by a centered scheme about the point $\mathbf{x}_i(t)$ in the interior and a one-sided scheme at the endpoints

$$A_i(t) = \frac{1}{2}\begin{cases} s_{i+1}(t) - s_i(t), & \text{if } i = 1; \\ s_{i+1}(t) - s_{i-1}(t), & \text{if } i = 2, \ldots, N-1; \\ s_i(t) - s_{i-1}(t), & \text{if } i = N, \end{cases} \tag{2.3.7}$$

where $s_i(t)$ is the discrete arclength given by

$$s_i(t) = \begin{cases} 0, & \text{if } i = 1; \\ s_{i-1}(t) + \left|\mathbf{x}_i(t) - \mathbf{x}_{i-1}(t)\right|, & \text{if } i = 2, \ldots, N. \end{cases} \tag{2.3.8}$$

For the case of axisymmetric flow, we need only change the definition of $A_i(t)$ in the numerical scheme. The approximate area in this case is

$$A_i(t) = \frac{\pi}{2} \begin{cases} (y_{i+1} + y_i)(s_{i+1} - s_i), & \text{if } i = 1; \\ 2\, y_i\, (s_{i+1} - s_{i-1}), & \text{if } i = 2, \ldots, N-1; \\ (y_i + y_{i-1})(s_i - s_{i-1}), & \text{if } i = N. \end{cases} \tag{2.3.9}$$

The normal to the shockfront $\mathbf{n}_i(t)$, which is required in (2.3.4), is determined by differentiating two cubic splines fitted to the data $\big(s_j(t), x_j(t)\big)$ and $\big(s_j(t), y_j(t)\big)$, $j = 1, \ldots, N$. Let $\tilde{x}(s)$ and $\tilde{y}(s)$ denote these two cubic spline interpolants, respectively. The smooth curve $\big(\tilde{x}(s), \tilde{y}(s)\big)$ is an approximation to the shockfront at time t. Therefore, $\mathbf{n}_i(t)$ is given by

$$\mathbf{n}_i(t) = \frac{\big(\tilde{y}'(s_i), -\tilde{x}'(s_i)\big)}{\Big[\big(\tilde{x}'(s_i)\big)^2 + \big(\tilde{y}'(s_i)\big)^2\Big]^{1/2}}, \qquad i = 1, \ldots, N, \tag{2.3.10}$$

where the primes denote differentiation with respect to s.

The shockfront position $\mathbf{x}_i(0)$ and the Mach number $M_i(0)$ are determined by the initial data given at $t = 0$. The parameters N and Δt are chosen by the general rules:

$$\Delta s_{avg} = \frac{1}{N} \sum_{i=2}^{N} \Delta s_i(0) = \frac{s_N(0)}{N} = K_1 \ll 1, \tag{R1}$$

$$\frac{\Delta t}{\Delta s_{min}} = \frac{\Delta t}{\min\limits_{\substack{2 \le i \le N \\ 0 \le t \le T}} \Delta s_i(t)} = \frac{\Delta t}{d \Delta s_{avg}} < K_2 = O(1), \tag{R2}$$

where $\Delta s_i(t) = s_i(t) - s_{i-1}(t)$ and d is a minimum tolerance on $\Delta s_i(t)$ which we discuss in detail later. Usually we take constants K_1 and K_2 equal to 0.01 and 0.2, respectively. Rule (R1) provides an adequate resolution of the shockfront. Rule (R2) is the Courant-Friedrichs-Lewy condition and gives stability for all cases

run. The shockfront at $t = \Delta t$ is determined using a second order one-step explicit scheme which provides the necessary initial information to begin the two-step leap-frog scheme.

The numerical scheme as described previously may be used in the absence of wall boundaries. These pure initial value problems occur in the case of self-focusing shock waves, for example.

In the presence of wall boundaries, the appropriate boundary conditions must be applied. Walls coincide with rays in the theory of geometrical shock dynamics; therefore, at wall boundaries the shock must be normal to the walls. Figure 2.4 illustrates how this boundary condition is implemented numerically. Points interior to the boundaries are calculated using the leap-frog scheme. The point at the boundary is then determined such that the line segment between the endpoint and its neighboring internal point is normal to the wall. Examples of these initial boundary value problems are shock wave diffraction and shock waves in channels.

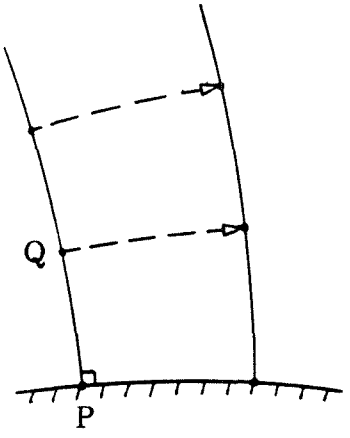

FIGURE 2.4. Numerical boundary conditions at a wall. Line segment PQ is normal to the wall at point P.

The numerical scheme provides for the insertion and deletion of points, as points tend to spread out in expansive regions or cluster in compressive regions of the shockfront. The point spacing $\Delta s_i(t)$ is checked periodically and we require

$$d \leq \frac{\Delta s_i(t)}{\Delta s_{avg}} \equiv \sigma_i(t) \leq D \qquad \text{for all } i = 2, \ldots, N, \tag{C1}$$

where $d = 1/2$ and $D = 3/2$ usually. If $\sigma_i(t) < d$, point $\mathbf{x}_i(t)$ is removed and if $\sigma_i(t) > D$, point $\mathbf{x}_{i-1/2}(t)$ is added using the cubic spline interpolant evaluated at $\frac{1}{2}\big(s_i(t) + s_{i-1}(t)\big)$. We preserve the area ratio $A_i(t)/A_i(0)$ in (2.3.6) by removing or adding the points at $t = 0$ as well. In either case if condition (C1) fails, the leap-frog scheme is restarted as previously described for $t = 0$.

We find it desirable to insert points in order to maintain the initially prescribed shockfront resolution (rule (R1)). Deleting points insures numerical stability at each time step (rule (R2)). Furthermore, rays tend to cross as shock-shocks form in compressive regions of the shockfront. By deleting points, shock-shocks are effectively fitted into the shockfront.

A simple two-step smoothing procedure is added to the numerical scheme in order to dampen the high frequency errors in $\mathbf{x}_i(t)$. After every n_s time steps (usually 10 to 50) we let

$$\frac{1}{2}\big(\mathbf{x}_{i+1}(t) + \mathbf{x}_{i-1}(t)\big) \rightarrow \mathbf{x}_i(t), \tag{2.3.11}$$

where we scan i even, then i odd, for $1 < i < N$. The numerical scheme is then restarted using the smoothed shockfront as initial conditions. The smoothing scheme (2.3.11) is one Jacobi iteration applied to the discrete system of equations

$$D^2\mathbf{x}_i(t) \equiv \mathbf{x}_{i-1}(t) - 2\mathbf{x}_i(t) + \mathbf{x}_{i+1}(t) = 0, \qquad 1 < i < N. \tag{2.3.12}$$

This iteration is effective in damping high frequency fluctuations in $\mathbf{x}_i(t)$. The overall shockfront given by the lower frequencies is essentially unchanged by this procedure.

2.4 Three Fundamental Shock Propagation Problems

Succesive shockfront positions are calculated numerically for the cases of shock wave diffraction, shock waves in channels and focusing shock waves. We establish the accuracy of our numerical scheme by comparing solutions obtained numerically with exact solutions found by Whitham and with numerical solutions found by Bryson & Gross [1961] using the method of characteristics for shock wave diffraction. We then compare the numerical calculations with experimental data for all three cases. Many important features of the flows presented in the experiments, namely, shockfront positions, triple-point positions (i.e., shock-shocks) and wall Mach numbers, are well represented in the numerical calculations. This demonstrates the usefulness of the geometrical shock dynamics approximation.

(a) Shock wave diffraction

A simple solution may be constructed using characteristics (2.2.14) for shock wave diffraction by a convex wall (Whitham [1974]). On a C_- characteristic

$$\theta - \omega(M) = \text{ constant.} \tag{2.4.1}$$

Since all C_- characteristics originate from the undisturbed region, $\theta = 0$ and $M = M_0$, we have

$$\theta - \omega(M) = -\omega(M_0) = \text{ constant everywhere.} \tag{2.4.2}$$

In particular, the wall Mach number M_w, perhaps the most important quantity for this problem, may be found given the wall inclination angle θ_w. Using (2.4.2) at the wall gives

$$\omega(M_w) = \theta_w + \omega(M_0). \tag{2.4.3}$$

For the purpose of testing our numerical scheme we use the strong shock approximation (2.2.4) which gives M_w explicitly

$$M_w = M_0\, e^{b\theta_w}, \tag{2.4.4}$$

where $b = n^{-1/2} = 0.44393$ for $\gamma = 1.4$. Whitham goes on to complete the solution for this problem; however, we stop here since we are primarily interested in comparing M_w.

We plot the value of M_w/M_0 versus $-\theta_w$ using relation (2.4.4) in figure 2.5a. The expanding shockfronts around a 45° convex wall are calculated numerically and shown in figure 2.5b. From our calculations, we determine M_w/M_0 at evenly spaced intervals of time and plot these values versus $-\theta_w$ as well. We see that the agreement between the exact curve and the numerical values is good.

For shock wave diffraction by a wedge it is also possible to obtain an exact solution. Here we use the jump conditions (2.2.15) and (2.2.16) with $M_1 = M_0$, $\theta_1 = 0$ and $M_2 = M_w$, $\theta_2 = \theta_w$

$$\tan\theta_w = \frac{\left(M_w^2 - M_0^2\right)^{1/2}\left(A^2(M_0) - A^2(M_w)\right)^{1/2}}{A(M_w)\,M_w + A(M_0)\,M_0}, \tag{2.4.5}$$

$$\tan(\chi - \theta_w) = \frac{A(M_w)}{M_w}\left(\frac{M_w^2 - M_0^2}{A^2(M_0) - A^2(M_w)}\right)^{1/2}, \tag{2.4.6}$$

where χ is the angle of the shock-shock line and $A = A(M)$ is the A-M relation (2.2.1). Again we use the strong shock approximation which gives

$$\tan\theta_w = \frac{(m^{-2} - 1)^{1/2}(1 - m^{2n})^{1/2}}{m^{n-1} + 1}, \tag{2.4.7}$$

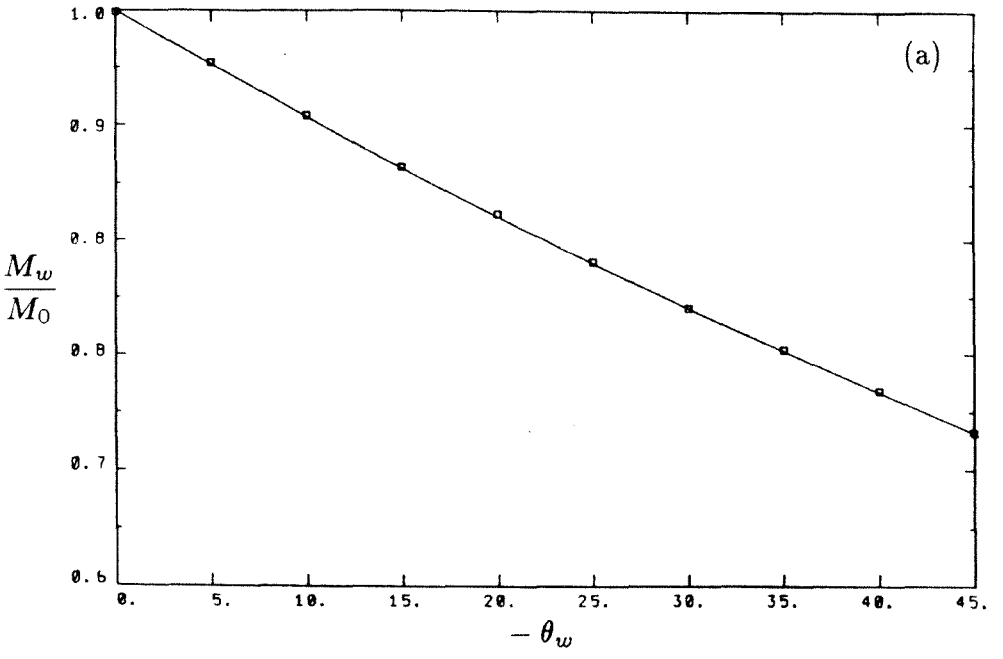

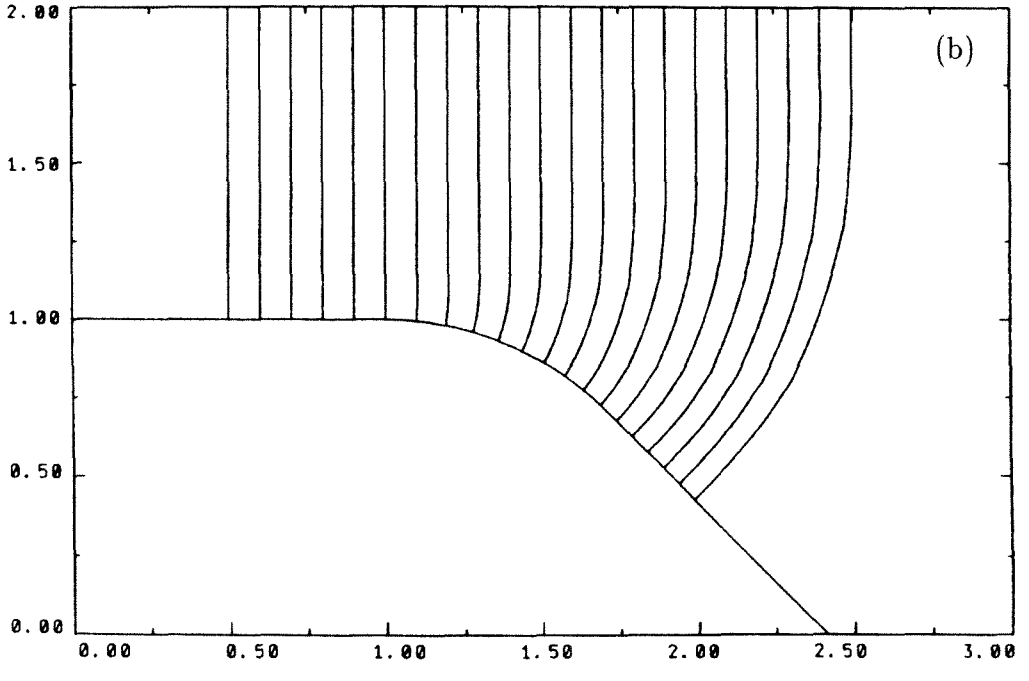

FIGURE 2.5. Shock wave diffraction by a convex wall: (a) M_w/M_0 versus $-\theta_w$; (b) expanding shockfronts around a 45° circular convex wall.

$$\tan(\chi - \theta_w) = m^n \left(\frac{1 - m^2}{1 - m^{2n}} \right)^{1/2}, \tag{2.4.8}$$

where $m = M_0/M_w$. Equation (2.4.7) gives m implicitly in terms of θ_w. Equation (2.4.8) then gives $\chi = \chi(\theta_w)$.

We plot $\chi(\theta_w) - \theta_w$ versus θ_w in figure 2.6a. Successive shockfronts are calculated for $\theta_w = 10°, 20°, \ldots, 70°$, and χ is determined for each from their graphs. Again we note the good agreement with the exact solution for all values of θ_w. A representitive calculation for $\theta_w = 30°$ is displayed in figure 2.6b. The position of the shock-shock is easily seen for $\theta_w = 30°$ which was the case for all values of θ_w run.

Another interesting case is shock wave diffraction by a smooth concave wall. In figure 2.7, we show the calculation for a 30° circular bend. The shock-shock in this case forms gradually as the shockfront is compressed by the wall. Farther downstream where the wall is straight, the shock-shock moves linearly away from the wall similarly to the wedge case. In fact, far downstream the angle between the shock-shock line and the wall is the same as for the 30° wedge.

Bryson & Gross [1961] obtained both numerical and experimental results for the diffraction of shock waves by cones, cylinders and spheres. Their numerical solutions also employed the theory of geometrical shock dynamics, but their numerical solutions used the method of characteristics based on (2.2.14) together with the jump conditions (2.2.15) and (2.2.16) in contrast to the more flexible numerical scheme presented here. They found their solutions predicted shockfront and triple-point positions quite well for all their experiments.

As a further test of our numerical scheme, we calculated shockfronts for all the examples presented by Bryson & Gross. We display our results only for cylinders and spheres, as the comparison for cones was essentially the same as for wedges.

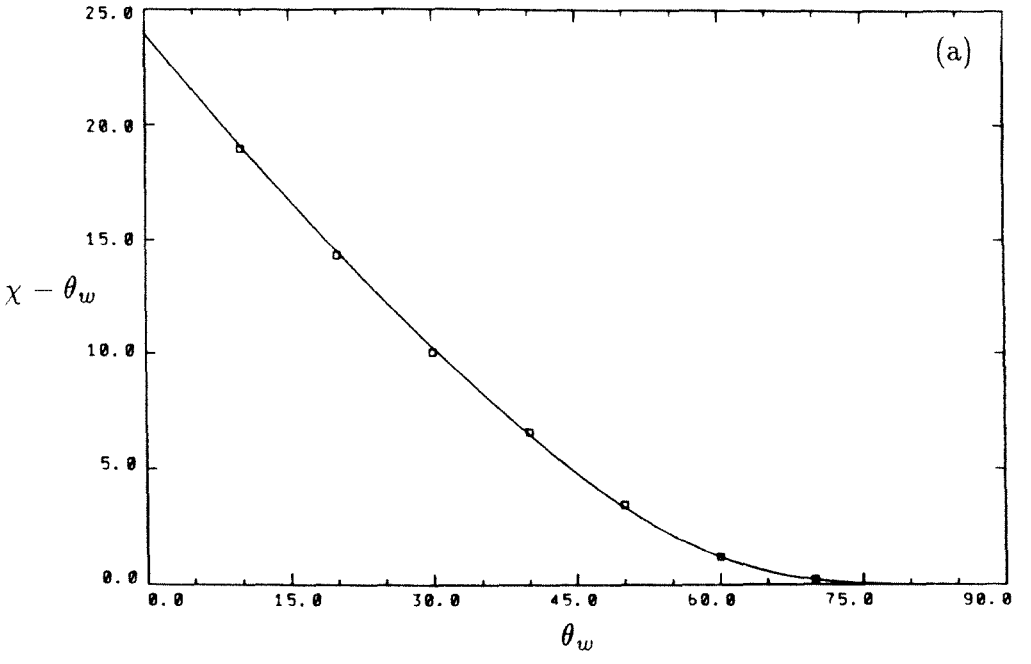

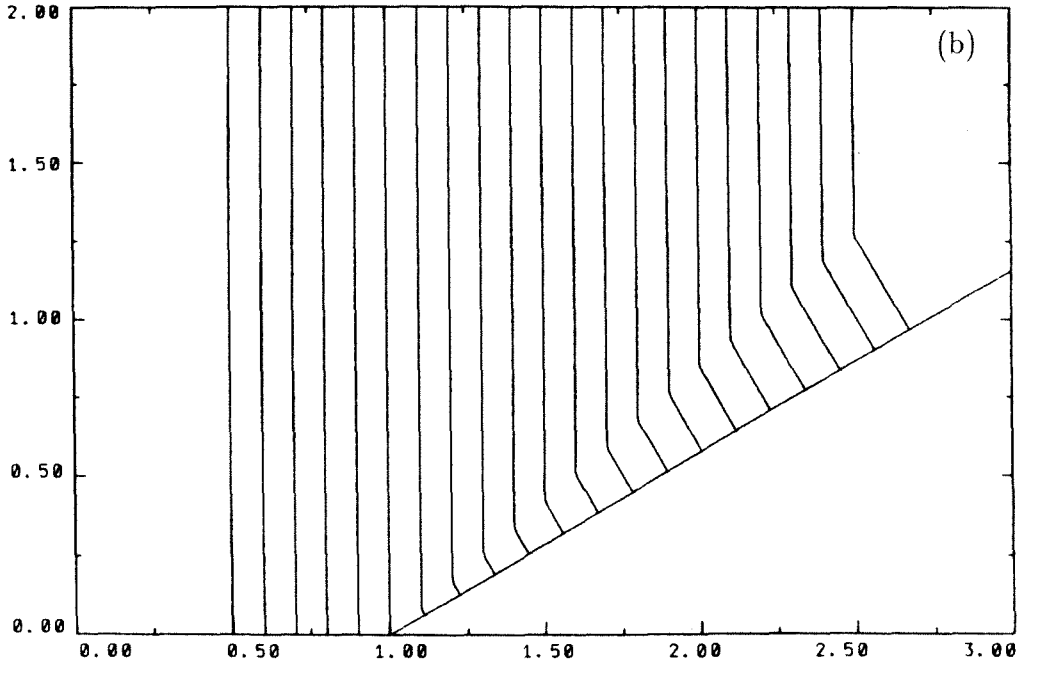

FIGURE 2.6. Shock wave diffraction by a wedge: (a) $\chi(\theta_w) - \theta_w$ versus θ_w; (b) shockfronts diffracted by a 30° wedge.

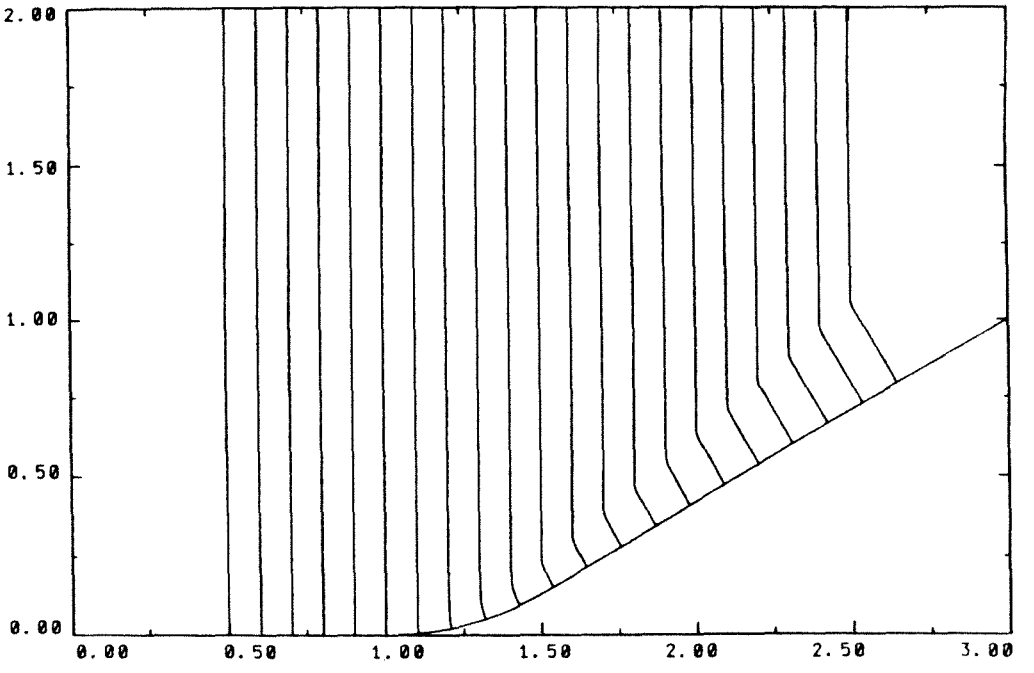

FIGURE 2.7. Shock wave diffraction by a 30° circular concave wall.

We calculate shock wave diffraction by a cylinder for $M_0 = 2.81$. The results of this calculation are shown in figure 2.8. In this case, we use the true A-M relation (2.3.5) (without assuming an approximate weak or strong shock limit) and invert $f(M)$ numerically. This will be done from now on unless specifically stated otherwise. The most interesting feature of this problem is the two loci of shock-shock positions that originate from the front and back of the cylinder and continue downstream. The shock-shock positions are determined numerically by searching for the maximum change in Mach number in the two regions of the shockfront where we know the shock-shock exists. The two loci of shock-shock positions are displayed in figure 2.8 by the two dashed lines.

In figure 2.9, we compare the loci of shock-shock positions obtained numerically with experimental data found by Bryson & Gross. We show only representive

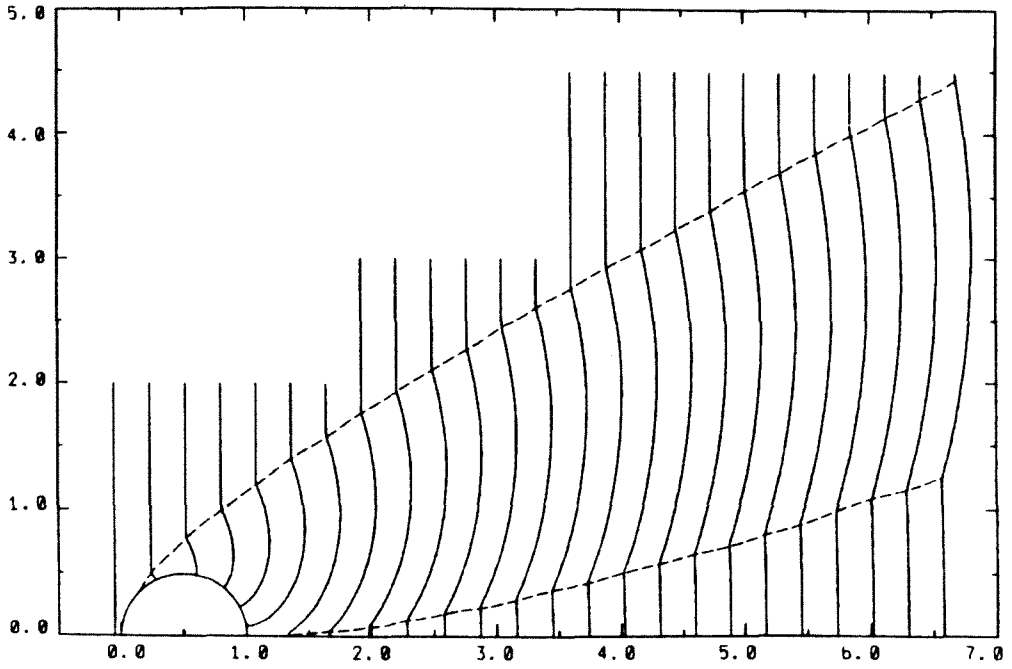

FIGURE 2.8. Shock wave diffraction by a cylinder for $M_0 = 2.81$. Shockfronts given by solid lines and loci of shock-shock positions given by dashed lines.

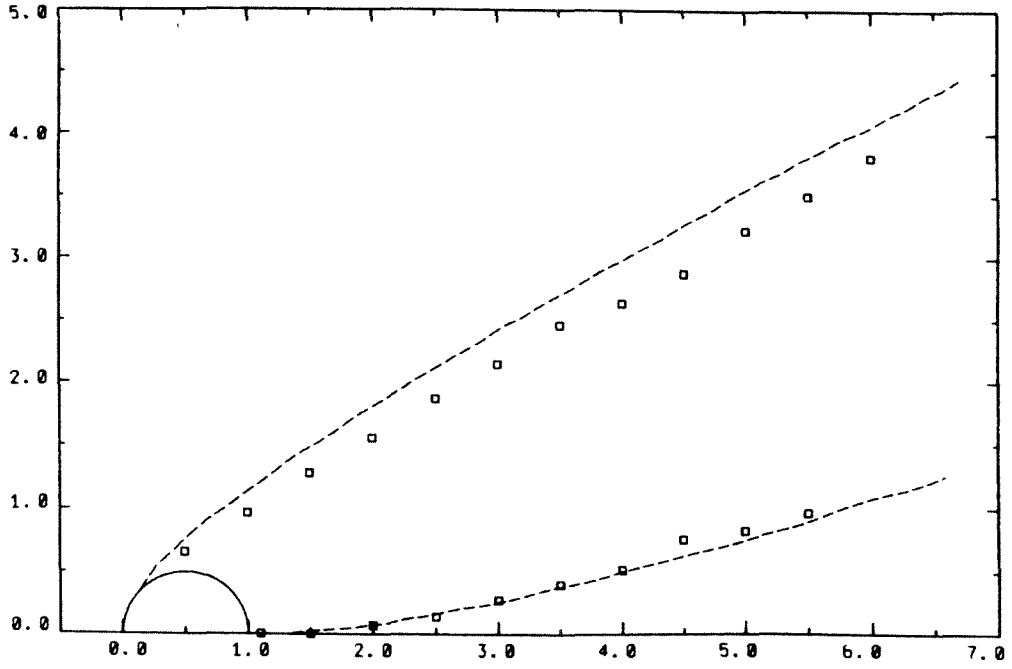

FIGURE 2.9. Shock wave diffraction by a cylinder. Numerical loci of shock-shock positions and experimental triple-point positions.

data points from the clusters of points given by Bryson & Gross. A sufficient number of points are displayed in order to indicate a trend in the data. The shock-shock positions calculated numerically are in good agreement with the experimental data for both loci of shock-shock positions. Bryson & Gross also obtain good agreement using their numerical solution found by the method of characteristics. However, there is some small systematic discrepancy between the present numerical results and those of Bryson & Gross. We suspect this discrepancy is a result of various approximations used by Bryson & Gross in order to construct their solution.

Finally, successive shockfronts are calculated for diffraction by a sphere at $M_0 = 2.85$ and are shown in figure 2.10. For this axisymmetric calculation, the alternate definition of $A_i(t)$ given by (2.3.9) is used in the numerical scheme. The shockfront pattern is much the same as for the cylinder case and we calculate the loci of shock-shock positions for the sphere as well.

The experimental shock-shock positions are shown along with the calculated positions in figure 2.11. For the sphere, the numerical results predict the experimental data very well for both the front and back loci of shock-shock positions. Bryson & Gross noted this fact also for the front locus of shock-shock positions. However, they were unable to obtain a solution using characteristics for the back locus of shock-shock positions. The experimental shock-shock positions for $M_0 = 4.41$ are also shown in figure 2.11. These data points are also in good agreement with the calculations. This indicates the relative insensitivity of the shock-shock positions for high Mach numbers (i.e., strong shocks).

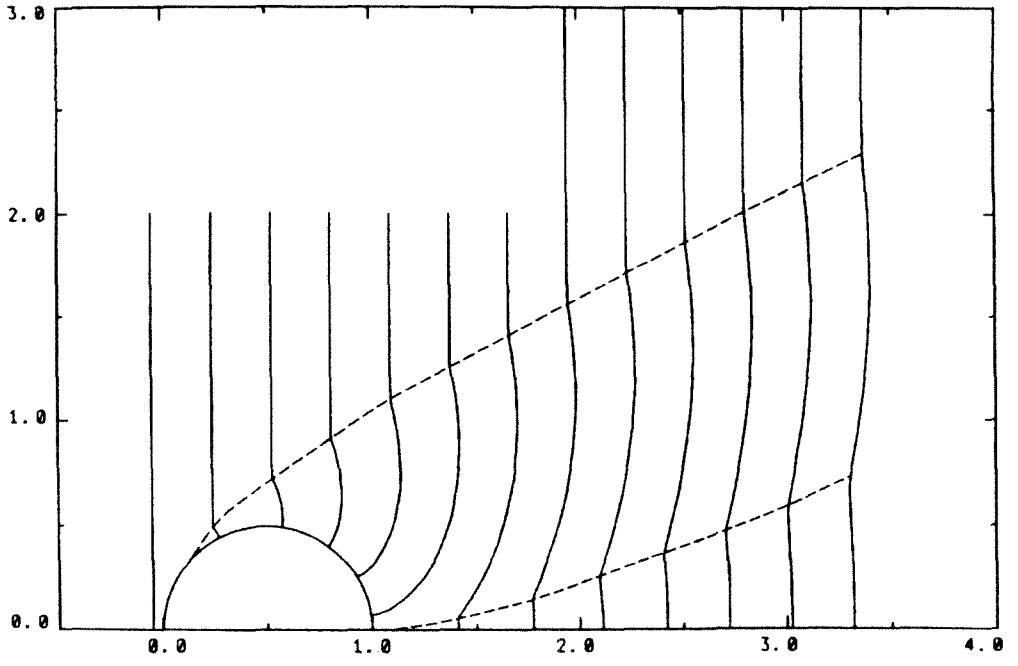

FIGURE 2.10. Shock wave diffraction by a sphere for $M_0 = 2.85$. Shockfronts given by solid lines and loci of shock-shock positions given by dashed lines.

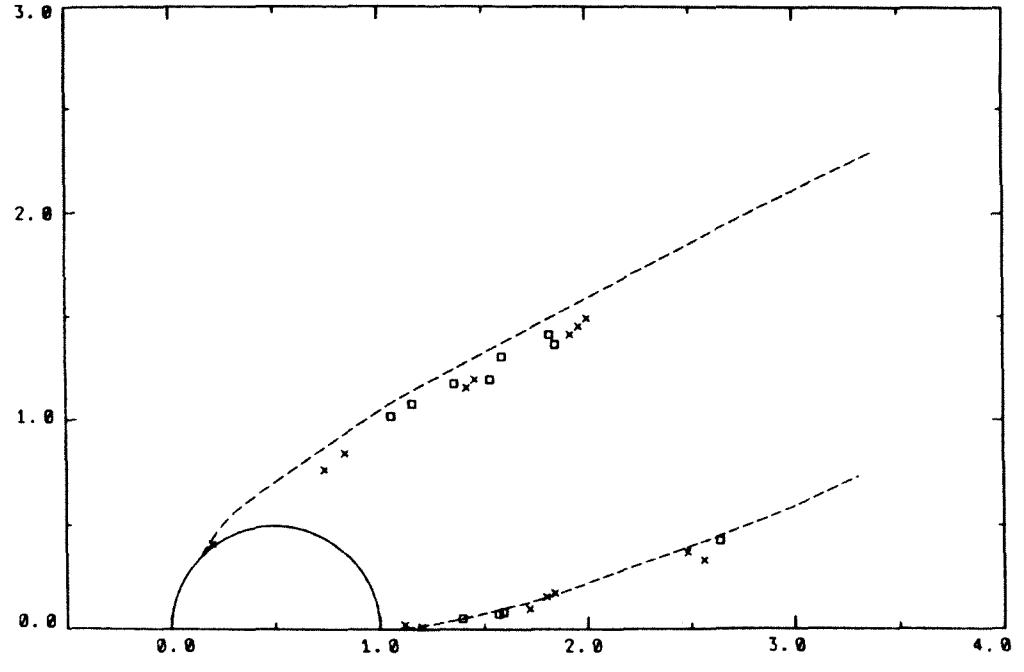

FIGURE 2.11. Shock wave diffraction by a sphere. Numerical loci of shock-shock positions and experimental triple-point positions (□ for $M_0 = 2.85$ and × for $M_0 = 4.41$)

(b) Shock wave propagation in channels

A natural extension of the case of shock wave diffraction is the case of shock waves in channels. We have seen, in the case of shock wave diffraction, that many solutions were availible to compare with our numerical solutions. To our knowledge, there are no solutions availible for the case of shock waves in channels. The added constraint of an additional wall boundary makes solutions obtained using the method of characteristics more difficult. This second wall boundary presents no additional problems in our numerical scheme since two boundaries are treated as easily as one boundary.

Edwards, Fearnley & Nettleton [1983] experimentally determined the behavior of shock waves propagating around 90° circular bends in channels with nearly rectangular cross section. Two bends were used, one having an inner radius of 48.9 mm. and an outer radius of 101.1 mm. and the other having an inner radius of 123.9 mm. and an outer radius of 176.1 mm. Let us refer to the channel with the smaller radius as channel 1 and the channel with the larger radius as channel 2. The experiments were performed for initial Mach numbers M_0 between 1.2 and 2.9. The experimental results consisted of a description of the shock wave pattern in the channels and measurements of wall Mach numbers M_w on the inner and outer walls.

In figure 2.12, we display a typical calculation for channel 1 (sharp bend). The shockfront expands around the inner wall in a similar fashion to the convex wall diffraction in part (a). At the outer wall, the shockfront compresses and forms a shock-shock. These two features are essentially independent until the expanding shockfront reaches the shock-shock. The shock-shock is then weakened and turned towards the inner wall. For channel 1, the shock-shock reaches the inner wall in the straight region of the channel after the bend for all Mach numbers considered. The shock-shock reflects off the inner wall and proceeds towards the outer wall.

This shock-shock reflection from wall to wall continues for some distance down the channel although it is not displayed in figure 2.12.

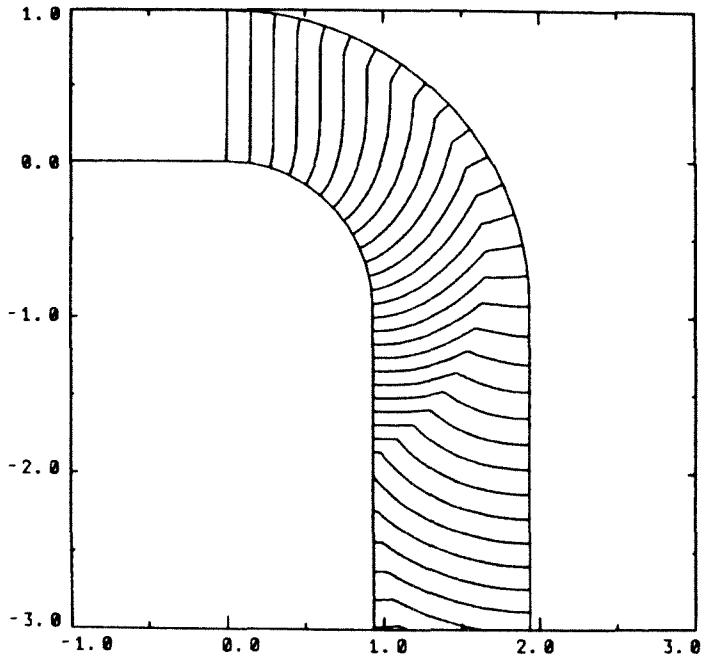

FIGURE 2.12. Shock wave propagation in channel 1 for $M_0 = 2.1$.

A typical calculation for channel 2 (shallow bend) is shown in figure 2.13. Many of the features are the same as for channel 1 except that the shock-shock may reach the inner wall before or after the bend, depending on the initial Mach number. For the particular value of M_0 shown, the shock-shock is seen to reach the inner wall at the end of the bend. The clear shock-shock reflection observed for channel 1 is not seen here since the angle between the incident shock-shock and the wall is small and the strength of the shock-shock is weaker. For $M_0 = 1.2$, the shock-shock reaches the inner wall after the bend; however, its strength is so weak that a clear reflection is still not observed.

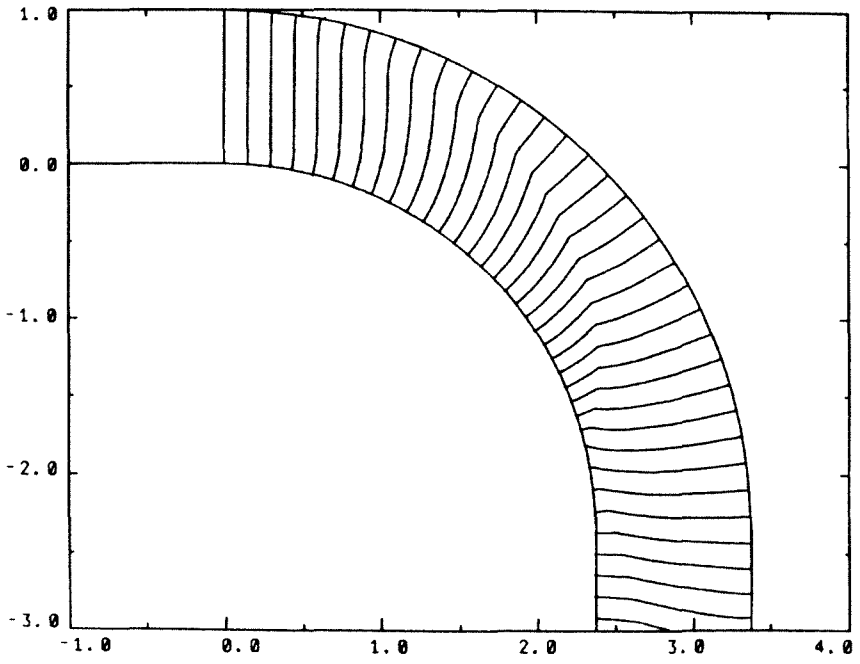

FIGURE 2.13. Shock wave propagation in channel 2 for $M_0 = 1.9$.

Edwards, Fearnley & Nettleton observed that the shock wave did not recover to a planar front within the bend for channel 1, which is in agreement with our calculations. Conversely, for channel 2, they found that recovery to the planar front did occur within the bend. Our calculations tend to support this observation. The shockfront recovers to a nearly planar front in all our calculations for channel 2.

Measurements of M_w versus distance along the wall are given by Edwards, Fearnley & Nettleton for the cases of $M_0 = 1.7$, 2.1, and 2.7 for channel 1 and $M_0 = 1.2$, 1.9, and 2.9 for channel 2. These cases are calculated numerically and we also determine the values of M_w. We compare the experimental data with the numerical values in figures 2.14 and 2.15. There are two sets of data in each figure corresponding to M_w from each wall. The set with $M_w/M_0 > 1$ comes from the outer wall and the set with $M_w/M_0 < 1$ comes from the inner wall. For each set,

the distance is measured from the beginning of the bend along the corresponding wall with the same scale used in figures 2.12 and 2.13.

The comparison for channel 1 is shown in figure 2.14. The Mach number on the inner wall in found experimentally to decrease to $0.6\,M_0$. We see that the calculations support these measurements. Both numerical and experimental results show the decrease in M_w around the bend and a constant M_w in the straight portion after the bend. On the outer wall, the experimental data show an increase in M_w to $1.3\,M_0$. Geometrical shock dynamics predicts a slightly larger increase to $1.4\,M_0$. Edwards, Fearnley & Nettleton predict a larger increase as well using a rough approximation to Whitham's theory which ignores the presence of the inner wall. This is an adequate approximation until the expanding shockfront from the inner wall reaches the shock-shock. In agreement with experimental measurements, we find the Mach number on the outer wall decreases as a result of this interaction. When the shock-shock reaches the inner wall, a large jump in M_w is observed in our calculations. Unfortunately, no experimental measurements were given to compare with this result.

Figure 2.15 shows the results for channel 2. For the shallow bend, M_w decreases to $0.7\,M_0$ on the inner wall in both experiments and our calculations. M_w increases to $1.15\,M_0$ on the outer wall in the experiments, whereas our calculations predict a slightly higher value. For $M_0 = 1.2$, the Mach number on the inner wall attains a constant value in the straight portion as in channel 1. For $M_0 = 1.9$ and $M_0 = 2.9$, a constant value is not reached since the shock-shock meets the inner wall before the end of the bend. The experimental evidence tends to support these observations as well.

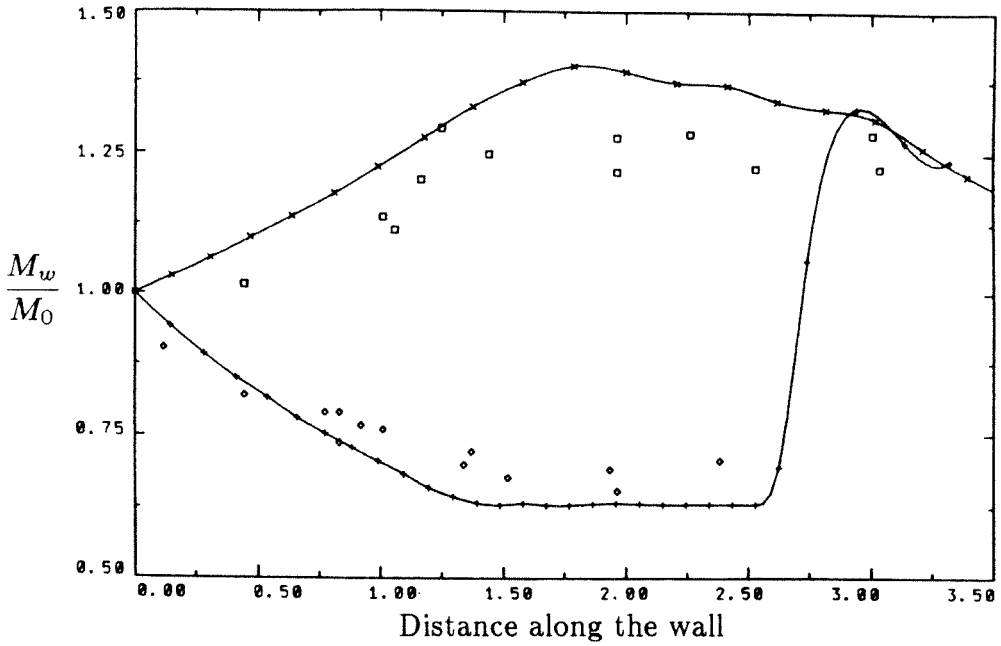

(a) $M_0 = 1.7$

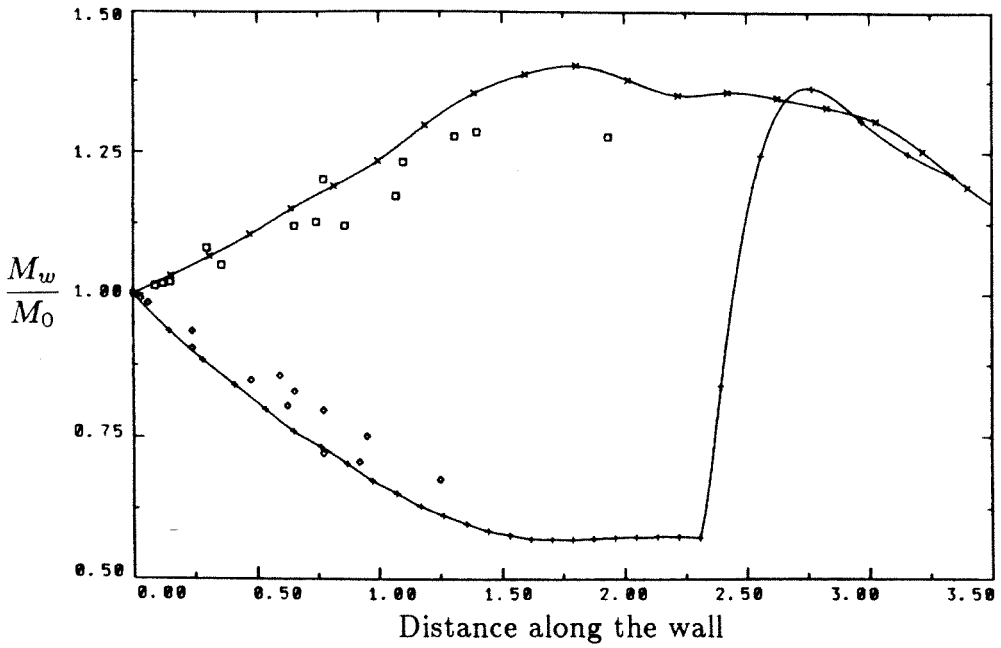

(b) $M_0 = 2.1$

FIGURE 2.14. M_w/M_0 versus distance along the wall for channel 1.

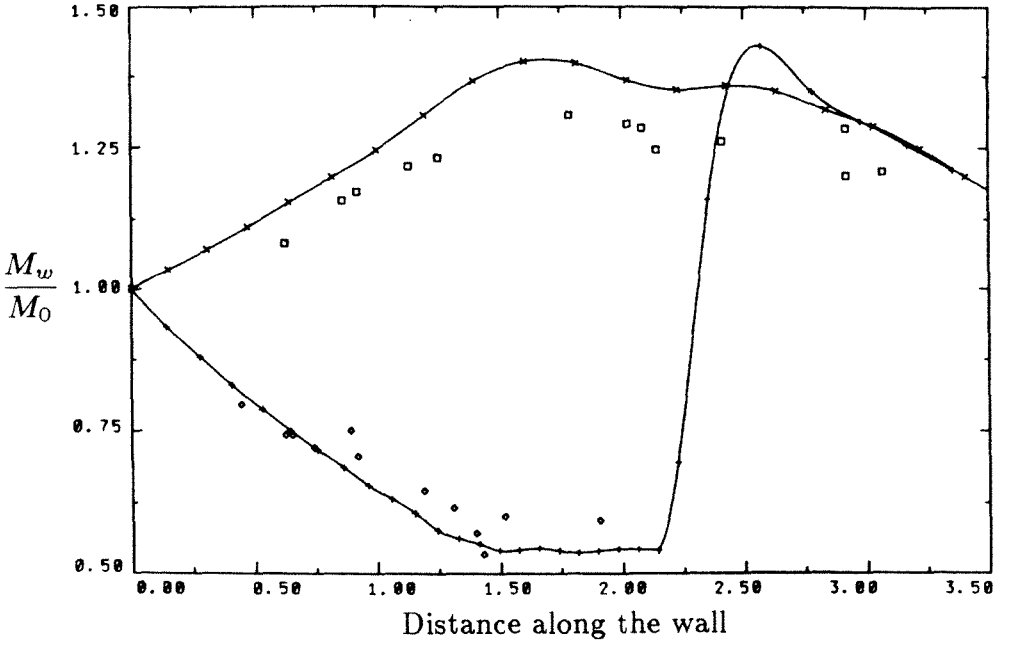

(c) $M_0 = 2.7$

FIGURE 2.14. (cont.). M_w/M_0 versus distance along the wall for channel 1.

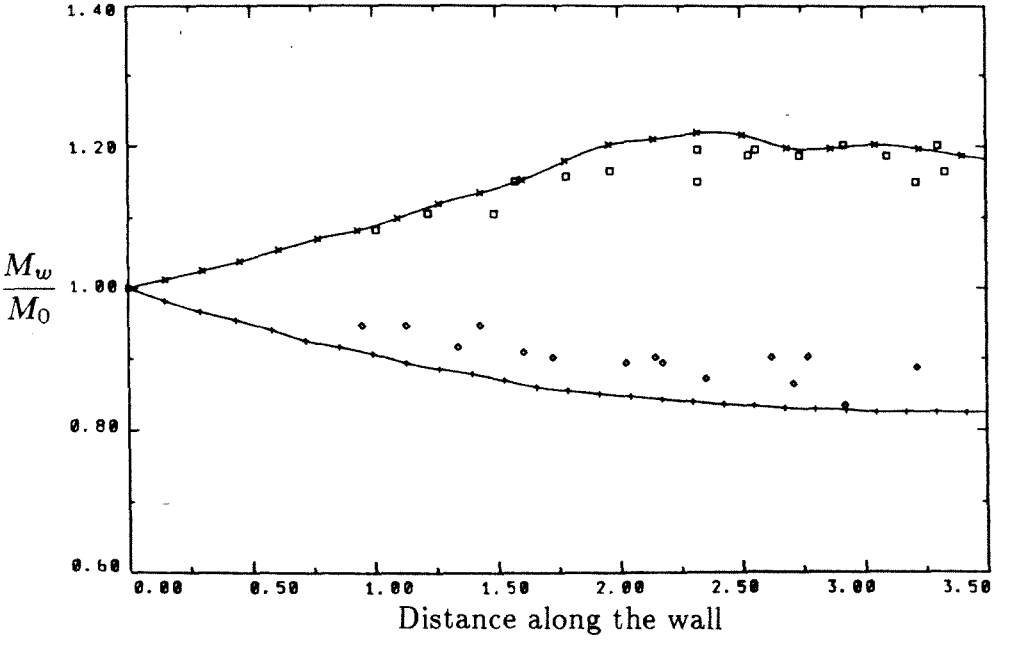

(a) $M_0 = 1.2$

FIGURE 2.15. M_w/M_0 versus distance along the wall for channel 2.

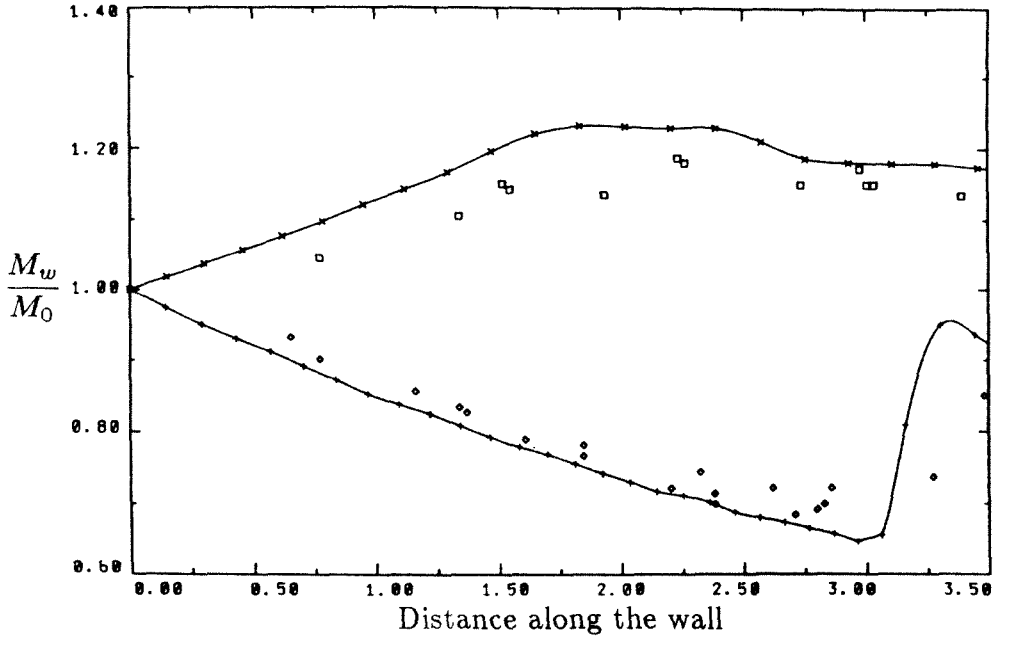

(b) $M_0 = 1.9$

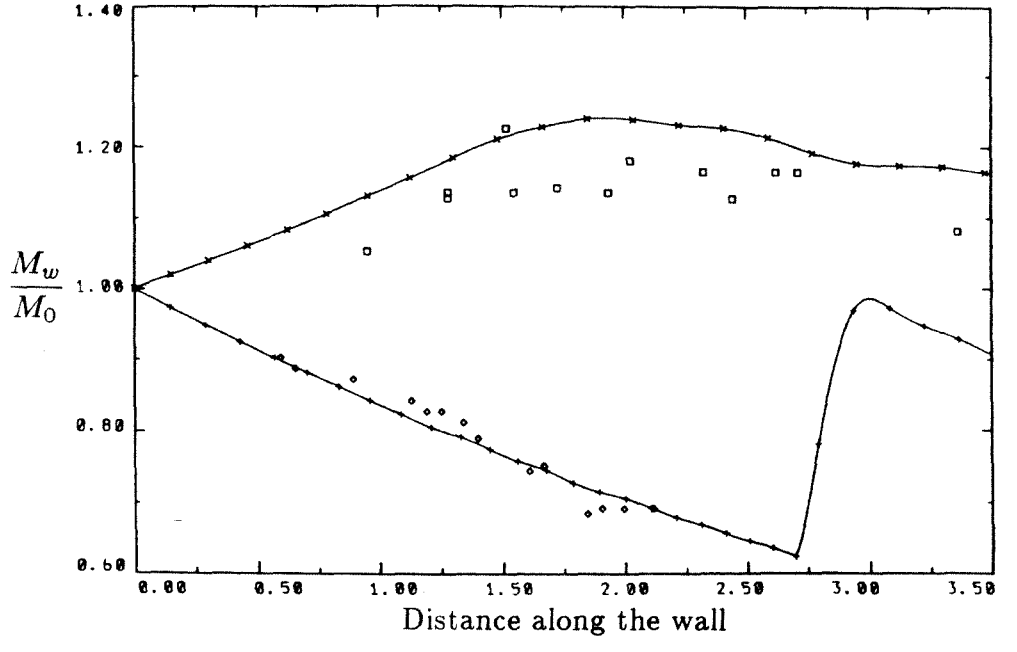

(c) $M_0 = 2.9$

FIGURE 2.15. (cont.). M_w/M_0 versus distance along the wall for channel 2.

(c) Shock wave focusing

We are interested in examining the focusing process as determined by geometrical shock dynamics. We numerically experiment with a variety of initial shapes and initial Mach numbers to study how these influences affect the focusing shock wave patterns calculated. Most of our calculations are motivated by experiments; however, we point out other interpretations as well. Overall, we find reasonable agreement with experimental observations. The results discussed here give a good first look at the focusing process. A more extensive study may be found in Chapter 5.

Sturtevant & Kulkarny [1976] experimentally studied the behavior of focusing weak shock waves. Initially, plane shock waves with M_0 between 1.005 (sound pulse) and 1.5 (comparatively strong shock) were propagated in a shock tube and brought to a focus by reflecting off various concave reflectors at one end of the shock tube. Depending on the initial Mach number of the incident shock wave and minimum radius of curvature of the reflected front, the shock either focused down upon itself and became crossed and folded, as in geometrical acoustics, or the shock did not focus down to a point. In the latter case, a pair of shock-shocks formed with a Mach stem-like section between the shock-shocks. They found the crossed pattern was preferred for lower initial Mach numbers or for reflected shockfronts with a smaller minimum radius of curvature.

To compare this experimentally determined behavior with that predicted by geometrical shock dynamics, two families of initially curved shockfronts were propagated numerically. The first family of initial shockfronts are given by

$$x = \frac{1}{R}\left(\frac{y^2}{y^2+2}\right), \tag{2.4.9}$$

where R is the minimum radius of curvature. For R positive, the curve given by (2.4.9) obtains a minimum of $x = 0$ on the axis of symmetry ($y = 0$) and

asymptotes to a maximum of $x = 1/R$ for $y \to \pm\infty$. Successive shockfronts calculated using the one-parameter family in (2.4.9) as initial conditions give a general picture of the focusing process determined by geometrical shock dynamics. These results also show good qualitative agreement with experiment. We refer to all curves given by equation (2.4.9) as profile 1. The second family of initial shockfront shapes labeled profile 2 is displayed in figure 2.16. The choice of profile 2 was motivated primarily to compare more closely with experimental data. (See later.) However, the results for profile 2 may also be viewed in the more general context as an example of a planar front with an inward bulge. The time evolution of these fronts illustrates the stability process for a planar shock wave as given by geometrical shock dynamics.

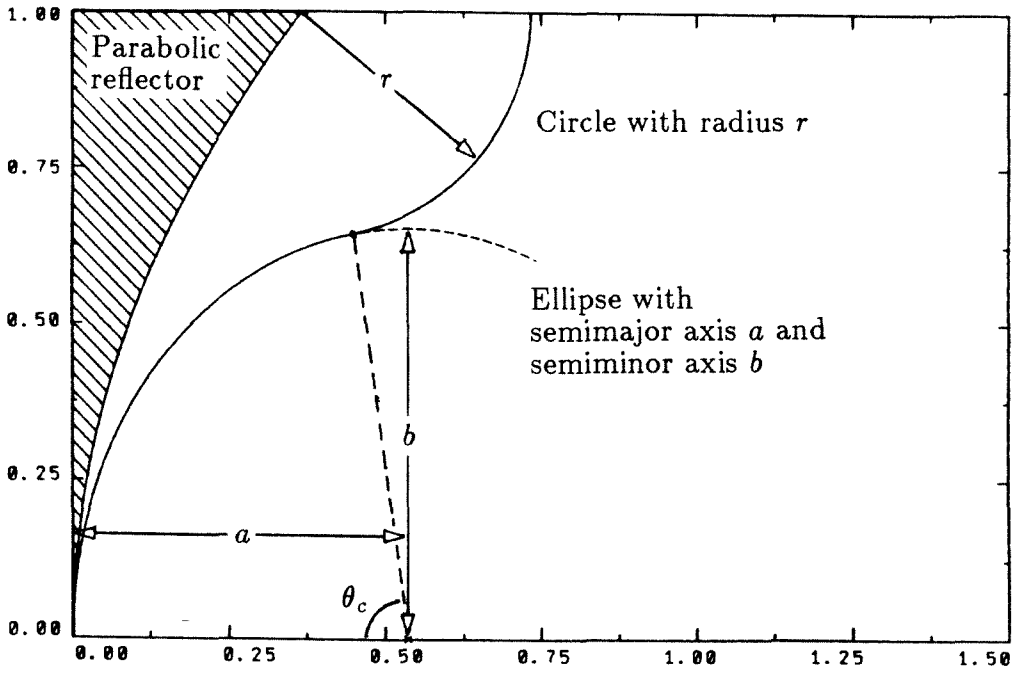

FIGURE 2.16. Profile 2 for $b/a = 1.22$ and $\theta_c = 80°$ given by the solid curve.

We first discuss the results obtained using profile 1. These calculations are performed in the absence of wall boundaries with the free ends of the shockfront initially at $y = \pm 4$. This domain is large enough so that the free ends do not affect the focusing process near the axis of symmetry. In the subsequent plots of the shockfronts calculated using profile 1, we display only the portion of the shockfronts near the axis of symmetry, since the focusing process is of main interest.

In geometrical acoustics, folded wavefronts occur and Sturtevant & Kulkarny's experiments show that this can continue for weak shocks. Geometrical shock dynamics, and the numerical version described here, show only the leading parts of the fronts. In particular, the numerical point removal procedure eliminates the overlap. This is done since the removed points would not describe the overlap correctly and would interfere with the continuation of the subsequent numerical steps. To show this and partially test whether this removal results in any error in the calculation of the motion of the shock, we compare the results of the numerical geometrical shock dynamics scheme for initial Mach number 1 (a sound wave) with the exact results given by geometrical acoustics.

Figure 2.17 shows the results for the propagation of a sound wave using geometrical acoustics and shock dynamics. The geometrical acoustics plot (figure 2.17a) was obtained directly by drawing the curves (including folds) at various distances out along the normals to the initial curve. The shock dynamics plot (figure 2.17b) was obtained by the numerical scheme using the weak shock A-M relation with $M_0 = 1$. It can be seen that these curves for the leading fronts are identical. The folds and the caustic do not appear explicitly in the geometrical shock dynamics plot. This gives verification that the elimination of the crossed and folded portion of the shockfront does not result in significant error in the remaining portion of the shockfront. The resulting discontinuity in the shockfront corresponds to the regular reflection of the expansion waves propagated along

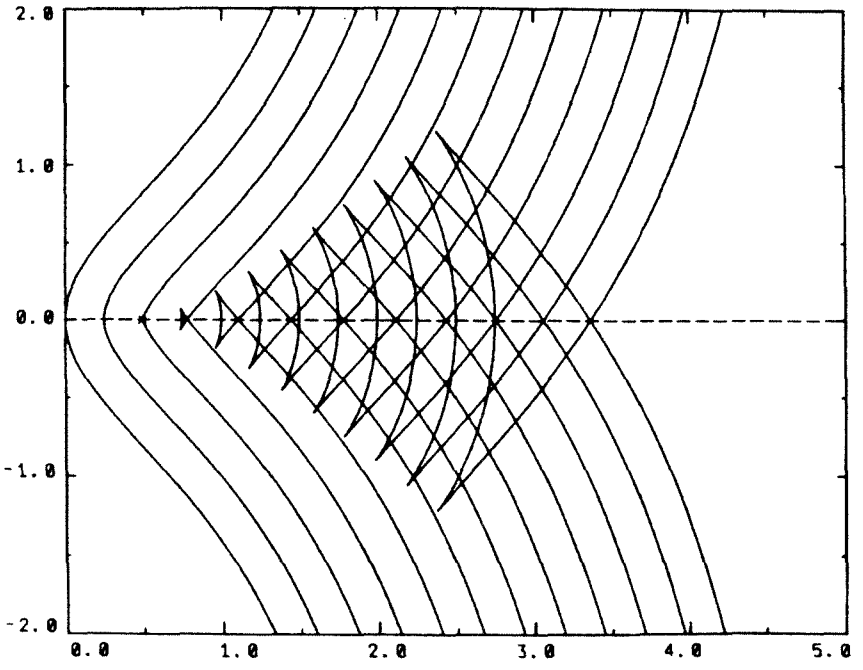

(a) Geometrical acoustics

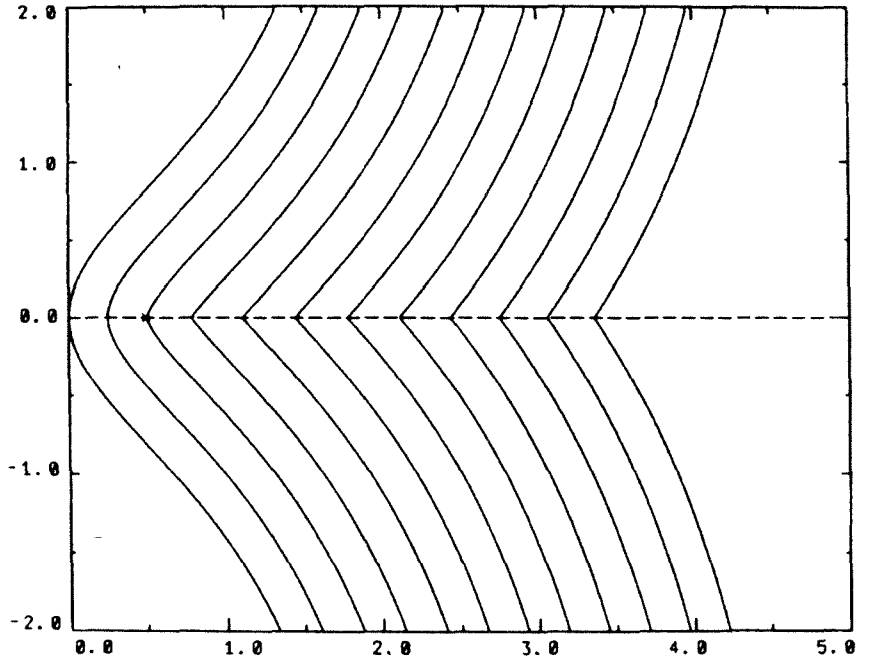

(b) Geometrical shock dynamics

FIGURE 2.17. Shock wave focusing for profile 1 with $R = 0.5$.

the shock when these waves meet. We note that the theory of geometrical shock dynamics does not allow for regular reflection explicitly and only permits Mach reflection. However, in cases where the Mach stem is very small (e.g., figure 2.17b), we treat these cases as regular reflection.

Successive shockfronts calculated using profile 1 with various values of R and M_0 are shown in figures 2.18 and 2.19. It can be seen from these plots that geometrical shock dynamics gives the same qualitative behavior as that observed by Sturtevant & Kulkarny. Expansion waves form on the shockfront and these move along the front and towards each other. For initial Mach numbers near 1, these expansion waves interact to give regular reflection initially, with Mach reflection occurring and a Mach stem forming at larger times. This change from regular to Mach reflection occurs when the angle between the interacting waves is large enough so that regular reflection can no longer occur. For larger initial Mach numbers, no regular reflection occurs and a Mach stem is formed from the start of the interaction. Furthermore, as the minimum radius of curvature of the initial shockfront increases, the transition point to total Mach reflection occurs at lower Mach numbers. It is interesting to note that for Mach numbers as low as 1.3, the behavior of the shock wave is qualitatively similar to that for strong shocks.

A more detailed comparison with the experimental data is obtained using profile 2 (figure 2.16). In the experiments performed by Sturtevant & Kulkarny, curved shockfronts were produced by reflecting plane shock waves by a curved reflector. The reflected wave then propagated into the uniform flow entrained by the incident shock. To compare more closely with these results, we require some initial shockfront shape that approximates the actual curved front as it leaves the reflector surface. The initial shockfront is then propagated numerically into a

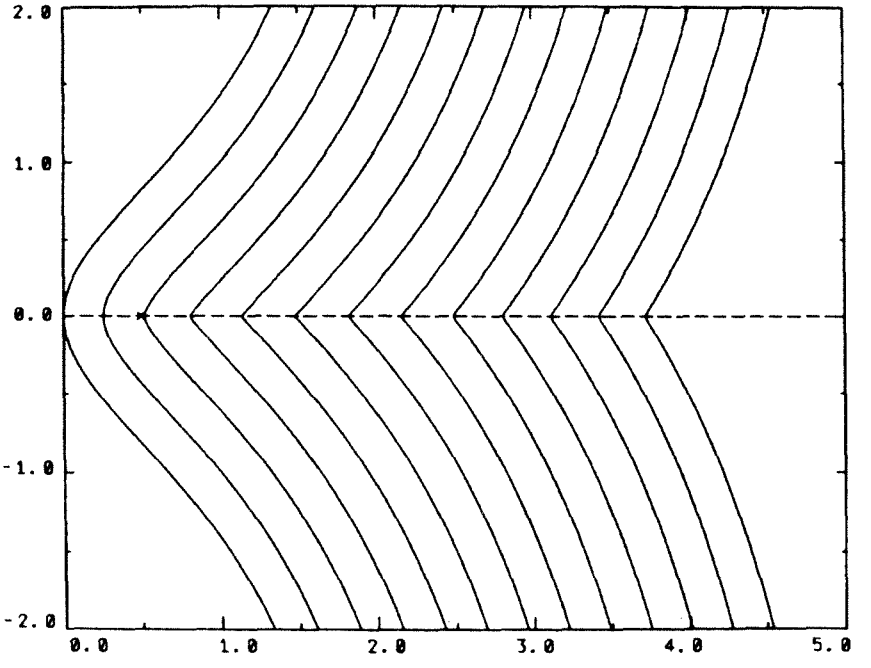

(a) $M_0 = 1.02$

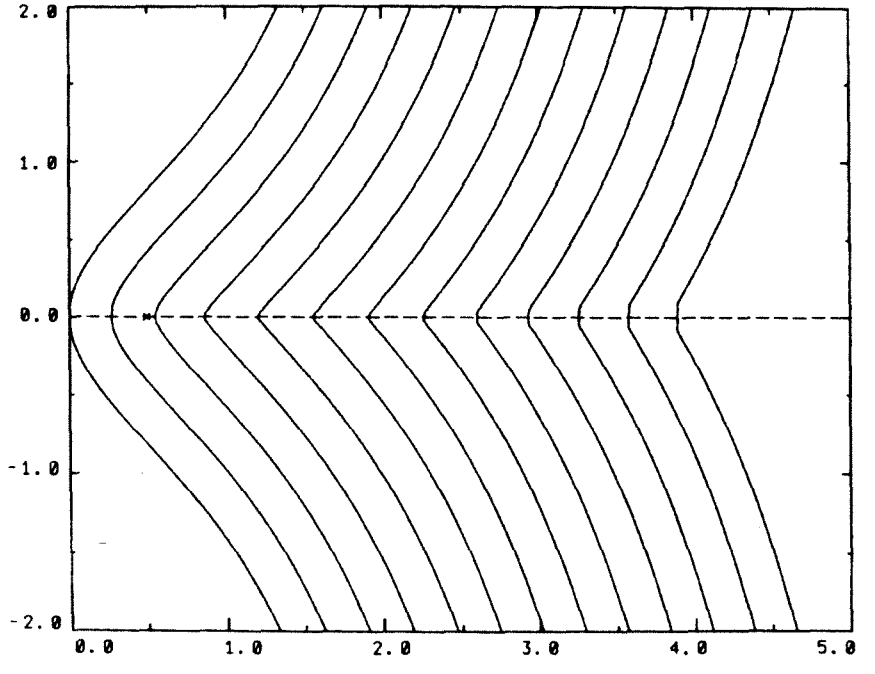

(b) $M_0 = 1.06$

FIGURE 2.18. Shock wave focusing for profile 1 with $R = 0.5$.

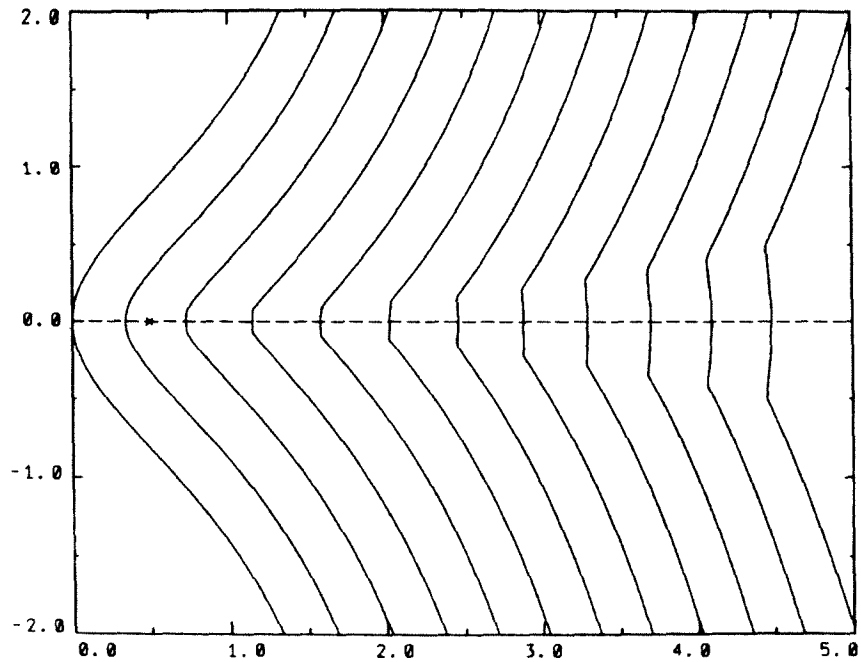

(c) $M_0 = 1.30$

FIGURE 2.18. (cont.). Shock wave focusing for profile 1 with $R = 0.5$.

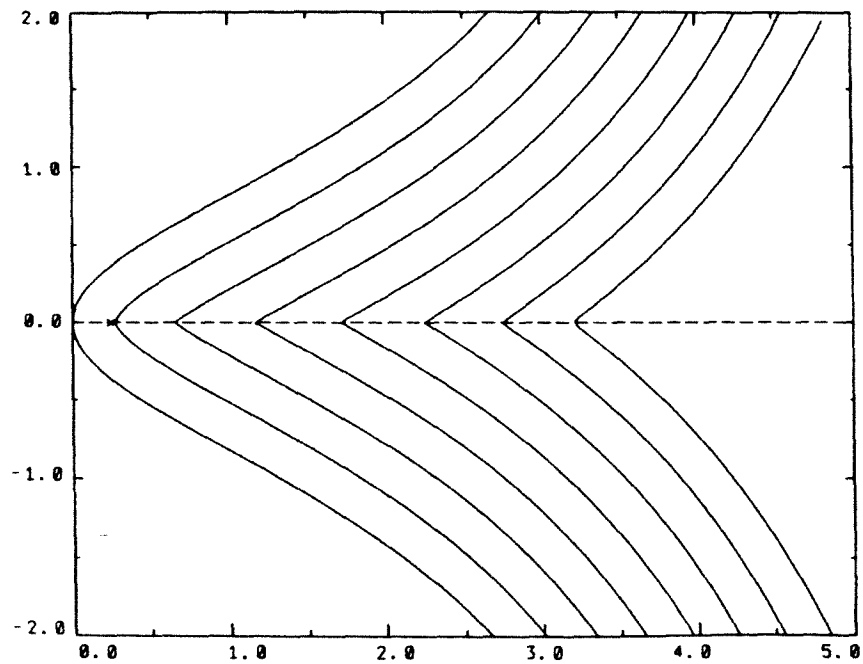

(a) $R = 0.25$

FIGURE 2.19. Shock wave focusing for profile 1 with $M_0 = 1.06$.

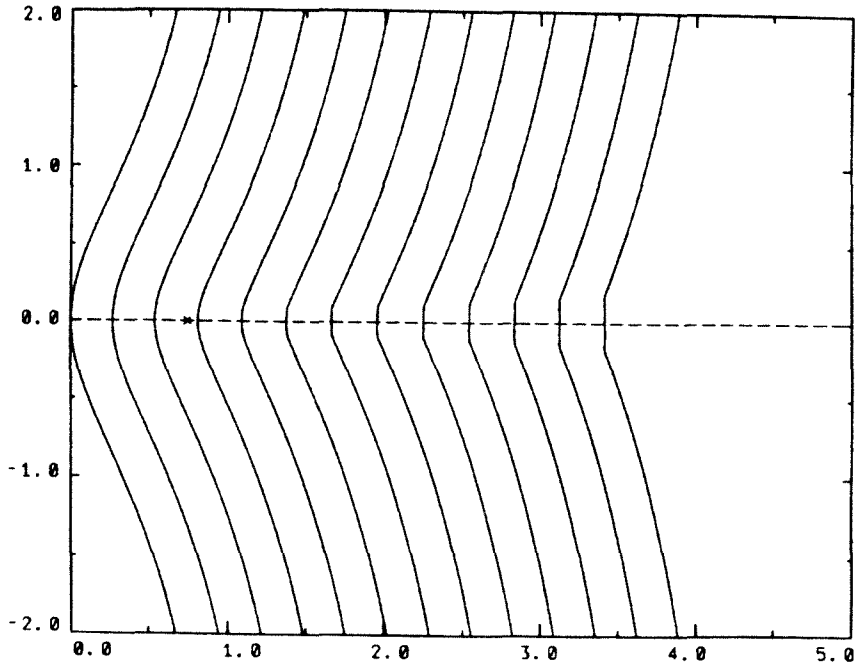

(b) $R = 0.75$

FIGURE 2.19. (cont.). Shock wave focusing for profile 1 with $M_0 = 1.06$.

uniform flow with Mach number M_1 given by

$$M_1 = \frac{2}{\gamma + 1} \frac{M_0^2 - 1}{M_0}. \tag{2.4.10}$$

The reflected shockfront shape as given by geometrical acoustics is a reasonable first approximation to the actual reflected wave for weak incident shocks. For the case of a parabolic reflector, profile 2 with $b/a = 1$ is this approximate reflected curve. We note, however, the actual reflected shock wave has a variable shock strength. The diffracted waves from the corners of the reflector are weaker than the incident shock wave; thus, they travel more slowly than the incident shock. Also, the outer portions of the incident shock wave reflect first and travel back into the flow entrained by the incident shock. These effects combine to give a flatter reflected shock wave than the reflected wave given by geometrical acoustics. The

aspect ratio b/a of the ellipse in figure 2.16 is used to model the flattening of the actual reflected shock wave.

The quantity b/a was found to have a large effect on the peak Mach number near the focus. We plot the Mach number versus distance on the axis of symmetry for different values of b/a in figure 2.20. For each curve the distance is normalized with respect to the radius of the inner circle ($b/a = 1$) for $\theta_c = 80°$. As expected, the peak Mach number decreases as b/a increases. Sturtevant & Kulkarny measured a peak relative shock strength of $\sigma = 4.9$ for $M_0 = 1.1$ and $\theta_c = 80°$. The relative shock strength is related to the Mach number by

$$\sigma \equiv \frac{z(M)}{z(M_0)}, \tag{2.4.11}$$

where $z(M)$ is the pressure ratio p_2/p_1 of the shock given by

$$z(M) = 1 + \frac{2\gamma}{\gamma + 1}(M^2 - 1). \tag{2.4.12}$$

We find that the initial curve for $b/a = 1.25$ gives the best agreement with experiment.

We also studied the effect of a nonconstant initial Mach number distribution on the peak Mach number. We experimented with different smooth Mach number distributions. In each case, the initial Mach number on the axis of symmetry was set equal to M_0 and decayed off the axis to a Mach number greater than or equal to 1. For weak shocks, our experiments showed a relatively small change in the peak Mach number for a variety of initial distributions.

Some typical views of the focusing shockfront patterns calculated using profile 2 are shown in figure 2.21. We found the general shockfront pictures did not depend significantly on the quantity b/a or the initial Mach number distribution. For simplicity, we take $b/a = 1$ and $M_0 =$ constant. Similar features seen in

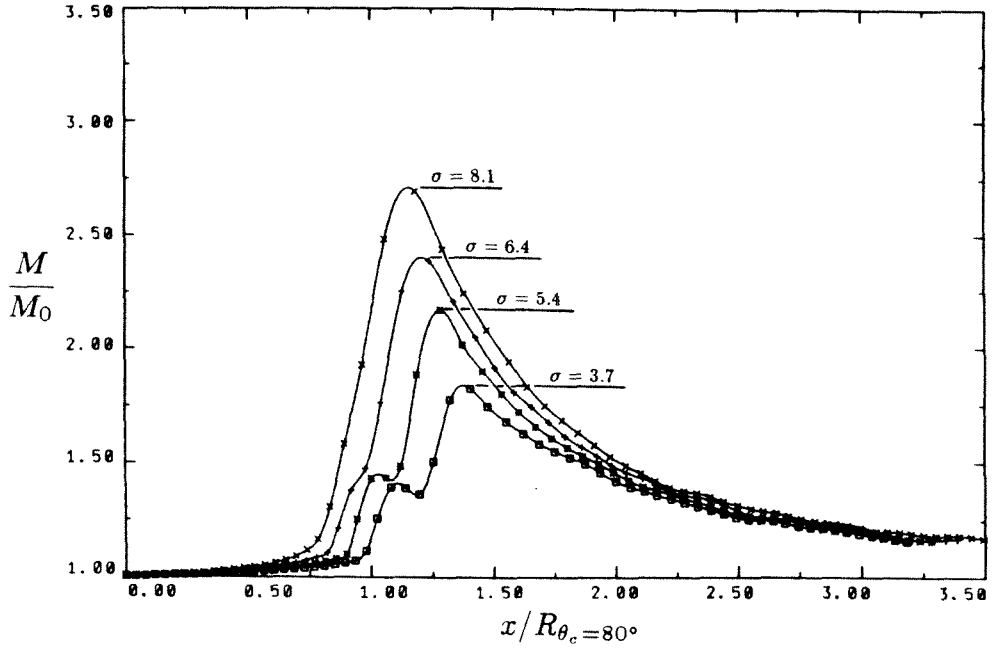

FIGURE 2.20. Mach number versus distance on the axis of symmetry for profile 2 with $\theta_c = 80°$, $M_0 = 1.1$ and $M_1 = .16$: × for $b/a = 1.0$, + for $b/a = 1.10$, ▪ for $b/a = 1.22$ and □ for $b/a = 1.34$.

figures 2.18 and 2.19 are observed in figure 2.21. For $M_0 = 1.1$, a single shock-shock forms near the focus before a transition to a pair of shock-shocks occurs farther downstream. A slightly larger M_0 shows a small Mach stem which forms initially just before the focus (figure 2.21b). The stem decreases in size as it passes the focus, then increases rapidly. An enlargement of the shockfronts near the focus is shown in figure 2.21c. This view clearly shows the narrowing Mach stem for $M_0 = 1.3$. Sturtevant & Kulkarny observed a similar narrowing Mach stem phenomenon, although their narrowing occurred for a slightly lower M_0.

It is also interesting to show the focusing shockfronts for $M_0 \gg 1$ (figure 2.21d). In this case, we consider the shockfront traveling into a gas at rest ($M_1 = 0$). This result is shown for completeness and is not meant to be compared with the experimental data obtained for weak shocks. Here, a Mach stem forms

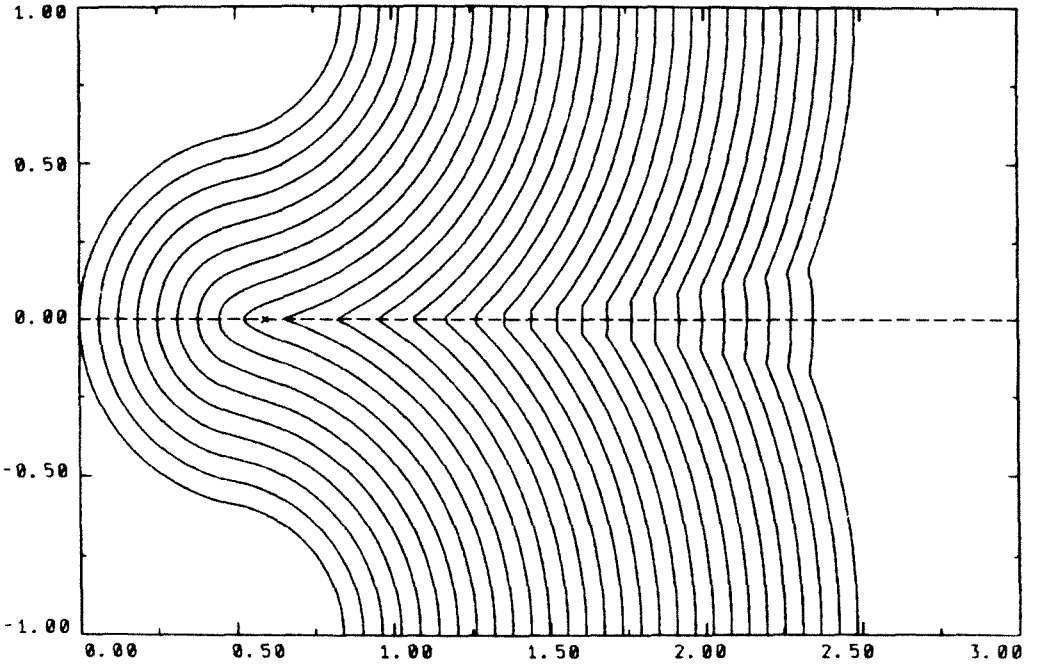

(a) $M_0 = 1.1$ and $M_1 = .16$

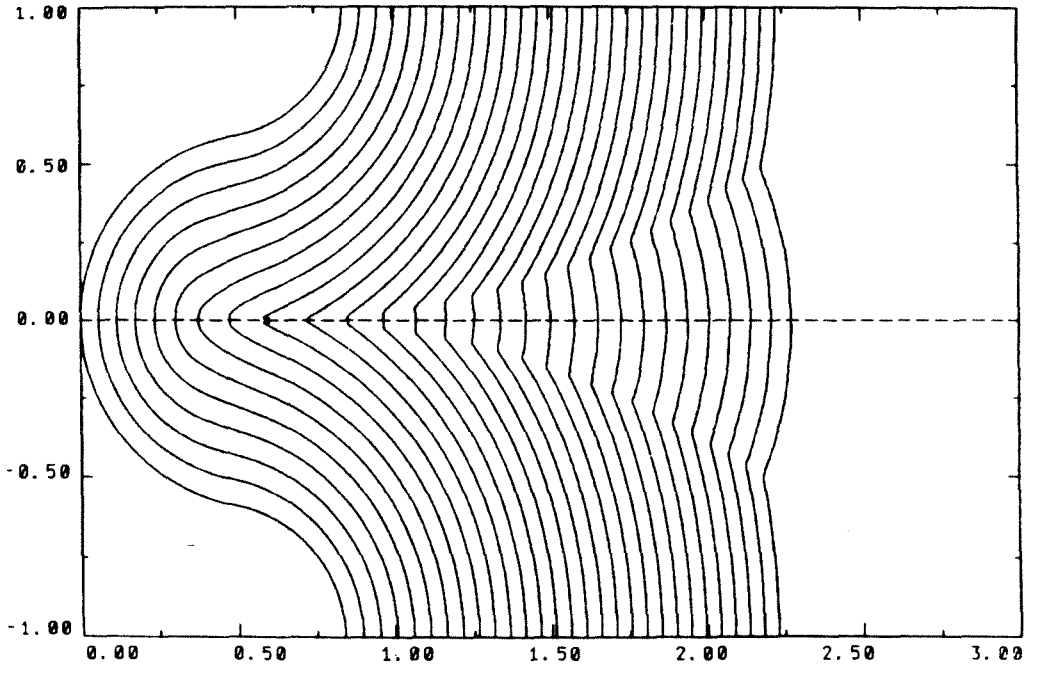

(b) $M_0 = 1.3$ and $M_1 = .44$

FIGURE 2.21. Shock wave focusing for profile 2 with $b/a = 1$ and $\theta_c = 80°$.

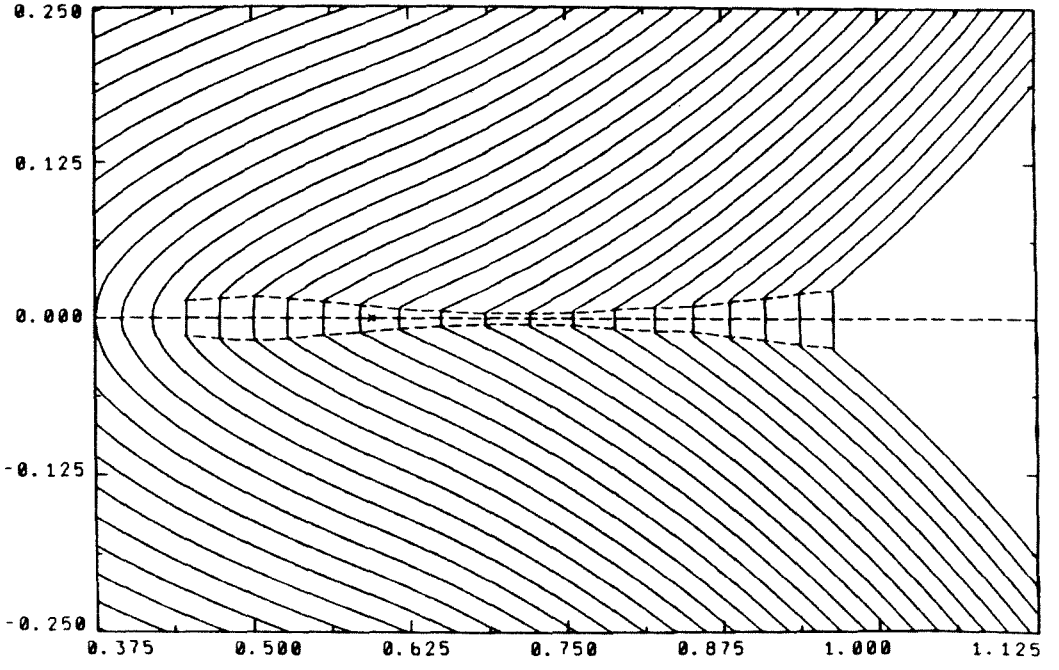

(c) $M_0 = 1.3$ and $M_1 = .44$ (narrowing Mach stem)

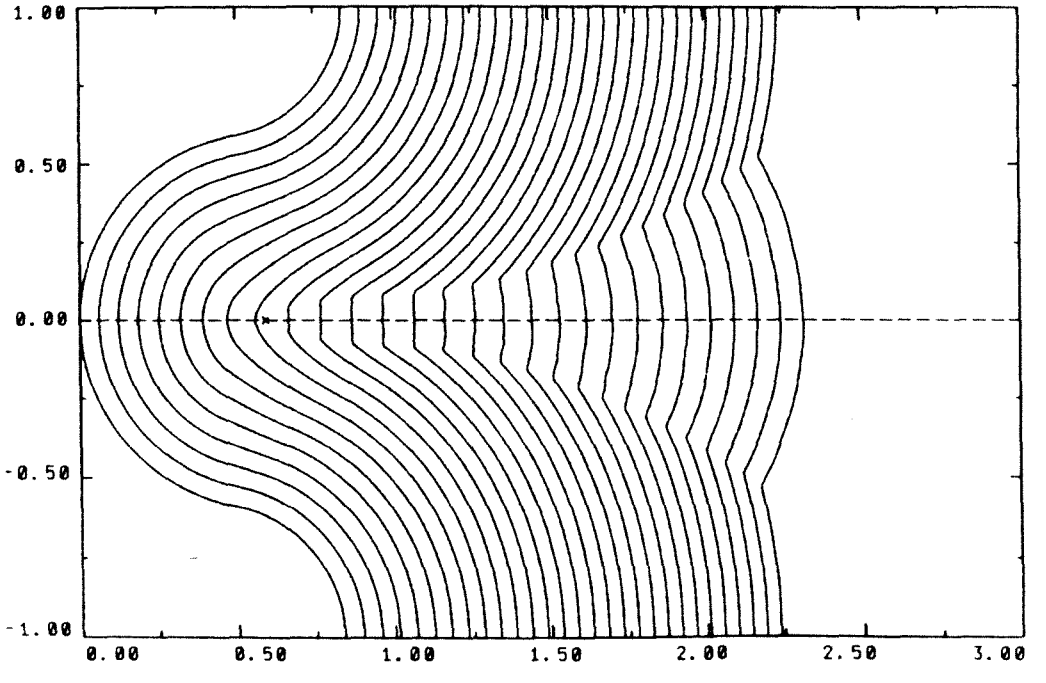

(d) $M_0 \gg 1$ and $M_1 = 0$

FIGURE 2.21. (cont.). Shock wave focusing for profile 2 with $b/a = 1$ and $\theta_c = 80°$.

initially and increases in size (without narrowing) as the shockfront propagates downstream.

In all the cases shown in figure 2.21, the curved shockfront far downstream is approaching a planar front. We see in these examples the stability mechanism for a planar front as determined by geometrical shock dynamics.

A further study of the Mach number versus distance gives added insight into the focusing process for profile 2. In figure 2.22, we see the effect of varying M_0 and θ_c on these curves. For $b/a = 1$, the radius of inner circle is related to θ_c by

$$R(\theta_c) = \frac{1}{2}\left(\frac{\cos\theta_c + 1}{\sin\theta_c}\right). \tag{2.4.13}$$

Linear theory (geometrical acoustics) gives a perfect point focus at a distance equal to $R(\theta_c)$ on the axis of symmetry for profile 2. The focus position determined by the peak Mach number always occurs after the focus for the nonlinear theory (geometrical shock dynamics). We also observe the formation of a shoulder before the peak in the family of curves for increasing M_0, in particular for $M_0 = 1.3$ (figure 2.22a). This shoulder corresponds to the initial formation of a Mach stem. For $M_0 = 1.3$, the stem decreases in length as it passes the linear focus point before it eventually increases in length. The peak in Mach number following the shoulder is a result of the narrowing stem.

The shoulder formation is a useful feature of the Mach number versus distance curves since it signals the transition from the basic single shock-shock pattern near the focus to the Mach stem pattern. The three curves in figure 2.22b are chosen to show this transition. The curve for $\theta_c = 80°$ is a typical curve corresponding to the single shock-shock pattern which we interpret as the actual shock wave being crossed at the focus. The presence of a shoulder followed by a peak in Mach number indicates that the focused pattern for $\theta_c = 70°$ is a transition case. For $\theta_c = 60°$, the peak has disappeared and only the shoulder remains. The Mach

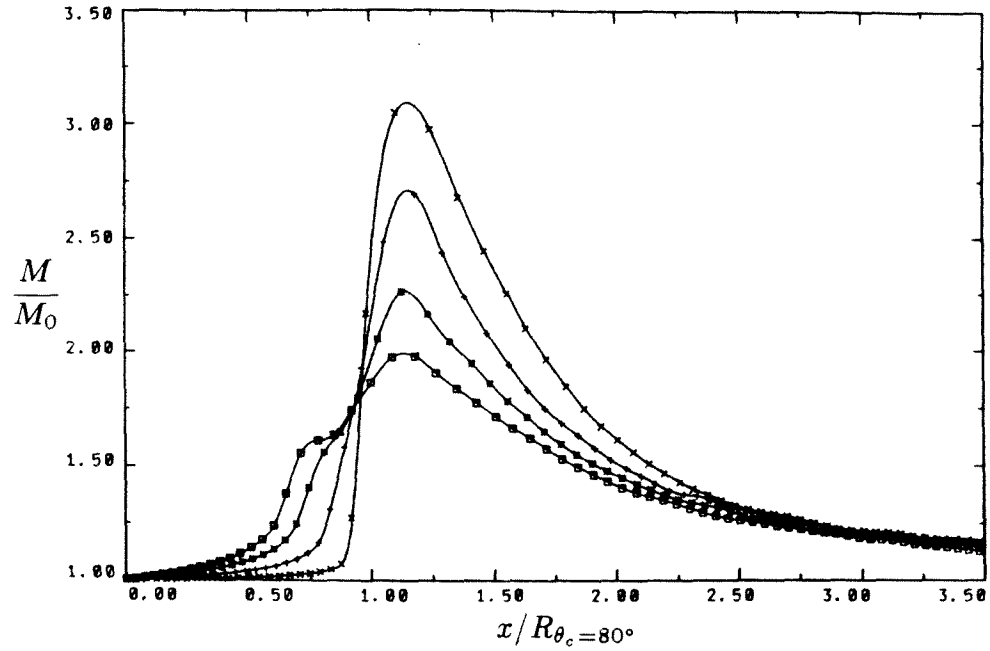

(a) $\theta_c = 80°$: × for $M_0 = 1.03$, + for $M_0 = 1.1$, ▪ for $M_0 = 1.2$ and □ for $M_0 = 1.3$.

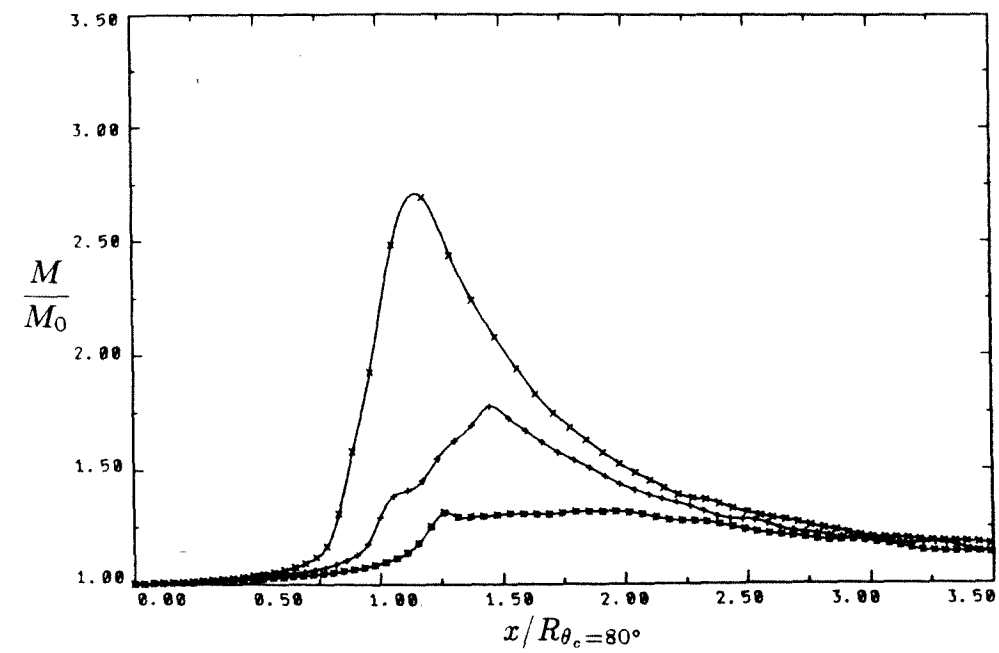

(b) $M_0 = 1.1$: × for $\theta_c = 80°$, + for $\theta_c = 70°$ and ▪ for $\theta_c = 60°$.

FIGURE 2.22. Mach number versus distance on the axis of symmetry for profile 2 with $b/a = 1$.

stem forms initially and propagates downstream without narrowing in this last case.

CHAPTER 3

Shock Propagation in Non-uniform Media

3.1 Introduction

We now wish to consider shock wave propagation in non-uniform media. In this case, the shock bends and distorts as it adjusts to the fluid non-uniformities as well as being affected by the curvature of the shock and the presence of walls. The latter two effects were the only ones present in the previous chapter for shock propagation in a uniform medium. In this chapter, we will stress the effects of the fluid non-uniformities on the propagating shock. The motion of the shockfront will be determined using the approximate theory of the geometrical shock dynamics. This theory is generalized to treat the case of shock propagation in non-uniform media by including the differential A-M relation (2.2.10) derived in part (a) of section 2.2.

A numerical scheme is developed to calculate the successive shockfronts. This scheme is an extension of the basic numerical scheme described in section 2.3 for the propagation of shocks in a uniform medium. The only added feature for non-uniform media is the numerical treatment of the differential A-M relation. As before, we approximate the shockfront by a discrete set of points. Each point is propagated along its normal to the shockfront with a speed specified by the generalized A-M relation. We determine the propagation speed for each point by a simple numerical integration of the A-M relation along rays. We describe the appropriate changes to the basic numerical scheme in section 3.2.

The special case of shock wave refraction at a planar interface separating two gases with different constant sound speeds was considered by Catherasoo & Sturtevant [1983]. On either side of the interface, where the fluid properties are uniform, they determine the shockfronts using the characteristic formulation of the equations of geometrical shock dynamics and the jump conditions at a shock-shock. At the contact discontinuity, Catherasoo & Sturtevant derive jump conditions based on the generalized equations of geometrical shock dynamics for non-uniform media. These conditions relate the Mach number and ray inclination angle on either side of the interface given the jump in sound speed across the interface. For the special case of shock refraction at a planar interface, the solutions are self-similar and are composed of centered expansion fans and jumps in M and θ along the refracted shock. The 'expansion fans' here refer to expansions in M and θ along the shock and should not be confused with the usual expansion fans discussed in gas dynamics. These similarity solutions may be constructed using characteristics along with the jump conditions at shock-shocks and at the interface. This is the method used by Catherasoo & Sturtevant. Catherasoo & Sturtevant compare their results with experimental data obtained by Jahn [1956], Abd-el-Fattah, Henderson & Lozzi [1976] and Abd-el-Fattah & Henderson [1978]. They find good agreement in all cases considered. We compare results obtained using the general numerical method of section 3.2 with Catherasoo & Sturtevant's solutions in section 3.3.

The presence of precursor waves has been observed experimentally for planar shock wave refraction at an inclined planar interface. For example, if the sound speed across the interface is greater than the sound speed in front, the shock-front bends forward as it crosses the interface. Depending on the incident shock strength and interface inclination angle, the shock wave across the interface may 'detach' from the incident shock. A precursor wave is then generated to connect

the shock across the interface to the incident shock. (See figures 3.6d–e.) Photographs and a discussion of these precursor waves may be found in Abd-el-Fattah & Henderson [1978], for example. We find the same precursor-shock wave patterns using geometrical shock dynamics, and these were not obtained from the theory previously.

Other interesting results were found experimentally by Haas & Sturtevant [1986] for shock wave refraction at cylindrical and spherical interfaces separating two different gases. Depending on the gas properties, the shock converged or diverged in the cylindrical or spherical region. Shockfronts determined using geometrical shock dynamics have not been found previously for this problem. We find that the shockfronts calculated using our numerical scheme compare well with the experimental results in both of these cases.

3.2 Numerical Scheme

In this section, we shall generalize the basic numerical scheme presented in section 2.3 to account for possible non-uniformities in the fluid properties ahead of the shockfront. The overall time marching procedure is basically unaltered by this generalization. We describe the shockfront by a discrete set of points. The normal direction to the shockfront is calculated at every point. We then propagate the shockfront along its normal with local velocity $U = a_0 M$, where the Mach number M is determined by numerically integrating the A-M relation (2.2.10) along rays. The integration of (2.2.10) is the only added feature to the numerical scheme. Recall that for a uniform medium, (2.2.1) gives M in terms of M_0 and A/A_0 independent of the ray path. The method of point removal and insertion and the smoothing scheme described in section 2.3 are also used. A helpful sketch of the basic numerical scheme is shown in figure 2.3.

The derivation of the time marching scheme follows the prescription given in section 2.3. Points $\mathbf{x}$ on the shockfront move along rays with velocity $U = a_0 M$. Therefore,

$$\frac{\partial}{\partial t}\mathbf{x}(\beta,t) = a_0(\beta,t)\, M(\beta,t)\, \mathbf{n}(\beta,t), \tag{3.2.1}$$

where $\mathbf{n} = (\cos\theta, \sin\theta)$ is the normal to the shockfront and β refers to the particular ray.

Discretization of (3.2.1) in space yields a system of N ordinary differential equations for the discete shockfront positions $\mathbf{x}_j(t)$, $j = 1,\ldots,N$. We then integrate the system of O.D.E.'s in time using the two-step leap-frog scheme

$$\mathbf{x}_i(t+\Delta t) = \mathbf{x}_i(t-\Delta t) + 2\Delta t\, a_{0i}(t)\, M_i(t)\, \mathbf{n}_i(t), \qquad i = 1,\ldots,N, \tag{3.2.2}$$

where $t = n\Delta t$ for $n = 0,\ldots,T/\Delta t$ and $a_{0i}(t)$, $M_i(t)$ and $\mathbf{n}_i(t)$ are the discrete sound speed, Mach number and shockfront normal at $\mathbf{x}_i(t)$, respectively.

The Mach number $M_i(t)$ in (3.2.2) is determined by numerically integrating the A-M relation (2.2.10) along rays. The independent variable x in (2.2.10) gives the position of the shock in the channel. It is convenient to replace this variable with t, the time at which a point on the shock has traveled a distance x along its ray. We then obtain $M_i(t)$ from the integral

$$\int_0^t \left\{ \frac{M\lambda}{M^2-1}\frac{\partial M}{\partial t} + \frac{1}{A}\frac{\partial A}{\partial t} + \frac{g}{a_0}\frac{\partial a_0}{\partial t} + \frac{h}{p_0}\frac{\partial p_0}{\partial t} + k\frac{\partial \gamma}{\partial t} \right\} dt = 0 \tag{3.2.3}$$

evaluated along the ray $\mathbf{x} = \mathbf{x}_i(t)$ for $i = 1,\ldots,N$. For simplicity, we take p_0, γ = constant. Equation (3.2.3) then becomes

$$-\log\frac{f(M_i(t))}{f(M_i(0))} + \log\frac{A_i(t)}{A_i(0)} + \int_0^t \frac{g(M(t))}{a_0(t)}\frac{\partial a_0}{\partial t}dt = 0 \qquad \text{for } i = 1,\ldots,N, \tag{3.2.4}$$

where $f(M)$ is given by (2.2.2) and $g = g(M)$ is given by (2.2.11). We appproximate the remaining integral in (3.2.4) using the simple scheme

$$\begin{aligned}\int_0^t \frac{g\big(M(t)\big)}{a_0(t)}\frac{\partial a_0}{\partial t}dt &= \sum_{k=1}^{n}\int_{(k-1)\Delta t}^{k\Delta t}\frac{g\big(M(t)\big)}{a_0(t)}\frac{\partial a_0}{\partial t}dt,\\ &\approx \sum_{k=1}^{n} g\Big(M_i\big((k-1)\Delta t\big)\Big)\int_{(k-1)\Delta t}^{k\Delta t}\frac{1}{a_0(t)}\frac{\partial a_0}{\partial t}dt,\\ &= \sum_{k=1}^{n} g\Big(M_i\big((k-1)\Delta t\big)\Big)\,\log\frac{a_{0i}(k\Delta t)}{a_{0i}\big((k-1)\Delta t\big)},\\ &\equiv \log I_i(t,0), \qquad (3.2.5)\end{aligned}$$

for $i = 1,\ldots,N$. We then use (3.2.5) in (3.2.4) to find

$$M_i(t) = f^{-1}\left(f\big(M_i(0)\big)\,I_i(t,0)\,\frac{A_i(t)}{A_i(0)}\right) \qquad \text{for } i = 1,\ldots,N. \qquad (3.2.6)$$

The approximate area $A_i(t)$ is given by (2.3.7) and (2.3.8) for two-dimensional flow and by (2.3.9) for axisymmetric flow.

The integral in (3.2.4) may be approximated in a number of ways. The approximation given by (3.2.5) is convenient since the same numerical procedure used to invert (2.3.6) may be used to invert (3.2.6). This is possible since $M_i(t)$ does not appear in the definition of $I_i(t,0)$. The approximation in (3.2.5) is that we take $g(M)$ = constant on each interval from $(k-1)\Delta t$ to $k\Delta t$. Other more complicated schemes may be used. However, since $g(M)$ varies 'slowly' for $M \in [1,\infty)$, the approximate evaluation (3.2.5) gives sufficient accuracy provided the change in a_{0i} between time steps is not too large. This will be a consideration for problems involving a sharp change in a_0 used to approximate a contact discontinuity. (See later.)

Equation (3.2.6) holds under the assumption that p_0, γ = constant. If p_0 is not constant, another approximate integral similar to $I_i(t,0)$ is simply added to (3.2.6). However, if we generalize further and let γ vary, then all but the

second term in (3.2.3) must be treated approximately. We point out that this generalization is not particularly difficult to handle. However, we will use (3.2.6) for simplicity in the present work.

We refer to section 2.3 for the remaining details of the numerical scheme. The shockfront normal $\mathbf{n}_i(t)$ in (3.2.2) is calculated by differentiating cubic splines fitted to the data $\big(s_j(t), x_j(t)\big)$ and $\big(s_j(t), y_j(t)\big)$, where $s_i(t)$ is given by (2.3.8) and then $\mathbf{n}_i(t)$ is given by (2.3.10). If wall boundaries are present, we require the shockfront to be normal to the wall in the numerical scheme. In expansive regions of the shockfront, points tend to spread out, and in compressive regions, the points tend to cluster. We check the point spacing and insert or delete points according to the scheme described in section 2.3. High frequency numerical fluctuations in the shockfront position $\mathbf{x}_i(t)$ accumulate in time. We use the smoothing scheme (2.3.11) to control these numerical errors.

3.3 Shock Wave Refraction

The numerical scheme described in section 3.2 is used to calculate shock waves propagating in non-uniform media. We first examine the case of shock wave refraction at a planar interface separating two gases with different constant sound speeds. This case was also considered by Catherasoo & Sturtevant [1983]. We compare results found using the present numerical scheme with the results of Catherasoo & Sturtevant. Their solutions were constructed using characteristics as discussed in section 3.1. We find good agreement between the two sets of results. This gives independent confirmation of the accuracy of shockfronts calculated using the numerical scheme of section 3.2. Furthermore, the case of shock wave refraction at a planar interface is interesting in its own right and we compare the results obtained using geometrical shock dynamics with the actual propagating shock waves observed experimentally.

In the second half of this section, we discuss the shockfronts calculated for the case of shock wave refraction by cylinders and spheres. We know of no other theoretical results for this problem. The shockfronts obtained numerically are compared with experimental observations reported by Haas & Sturtevant [1986]. Many of the flow features observed experimentally are also seen in the shock dynamics calculations. We find good agreement with these flow features.

(a) Shock Wave Refraction at a Planar Interface

The geometry of the first problem considered is shown in figure 3.1. The interface **I** is composed of two planar parts. The lower part is vertical, and the upper part is inclined at an angle δ_I. The incident planar shockfront **S** travels towards the interface with constant Mach number M_1. The sound speed in this region is a_{01}. After contact with the interface, the shockfront **S′** bends to adjust to the different sound speed a_{02} on the opposite side of the interface. The curved central portion of **S′** originates from the refraction at the interface corner. At a sufficient distance away from the central portion, **S′** remains planar traveling with constant Mach number M_1 in the upper part and M_2 in the lower part. The case shown in figure 3.1 is for $a_{02} > a_{01}$.

The portion of the interface behind the leading shockfront is deflected as a result of the moving gas behind. This deflection is not shown in the plots. We show only the position of interface at the point the shockfront meets it, since we are interested primarily in the motion of the shockfront, not in the motion of the gas behind.

Solutions obtained by Catherasoo & Sturtevant assume a discontinuous jump in sound speed at the interface. They obtain jump conditions that relate M and θ on either side of the interface in terms of interface inclination angle δ_I. The jump conditions involve a differential equation which determines M across the interface,

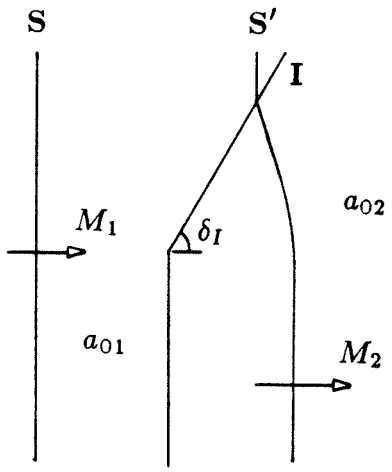

FIGURE 3.1. Interface geometry.

given the conditions in front and a_{02}. The geometric constraint that the shockfront remains continuous determines θ across the interface. Shockfronts calculated using our numerical scheme do not assume a discontinuous jump in sound speed. Instead, we model the contact discontinuity by a continuous distribution of sound speed with a sharp change from a_{01} to a_{02} at the interface. The width of our interface is such that a minimum of approximately 10 time steps are required for the shockfront to traverse the interface. This minimum restriction is needed for an accurate integration of the A-M relation (3.2.5). We note that the numerical integration of the A-M relation for each point as it crosses the interface is equivalent to a numerical integration used by Catherasoo & Sturtevant to obtain their jump conditions.

In figure 3.2, we display the shockfronts calculated using the present numerical scheme. The five different values of the interface inclination angle shown, $\delta_I = 60°$, $45°$, $30°$, $0°$ and $-45°$, are chosen to correspond to five of the many cases obtained by Catherasoo & Sturtevant. For all five plots, $M_1 = 5.0$ and $a_{02}/a_{01} = 2.0$. For

$\delta_I = 60°$, the incident planar shock wave meets the inclined interface and bends sharply forward to adjust to the larger sound speed on the other side. The refracted shockfront across the interface is composed of three regions of constant M and θ separated by two centered expansion fans in M and θ along the shockfront. We indicate the two expansion fans in figure 3.2a by the dotted lines. (These lines are determined by the change in θ along the shock and are not explicitly calculated in the present numerical scheme.) The two expansion fans are of different type, one belonging to C_+ and the other to C_- in equation (2.2.14). Two expansion fans are required in this case as waves travel in both directions on the shockfront away from the interface corner. The sharp bend in the shockfront seen at the inclined interface calculated using geomectrical shock dynamics is interpreted as *regular refraction* of the actual shock wave. As δ_I decreases, the C_+ expansion fan meets the interface. A further decrease in δ_I results in the formation of a shock-shock in front of the inclined interface. The locus of shock-shock positions is denoted by the dashed lines in each figure. The presence of shock-shocks are seen for $\delta_I = 45°$ and $30°$ (figures 3.2b and 3.2c). We interpret this shockfront pattern as *irregular refraction* for the actual shock wave. Finally, figures 3.2d and 3.2e show a second shock-shock above the interface for $\delta_I = 0°$ and $-45°$. This occurs after the C_- expansion fan meets the interface.

We point out one important difference between the present calculations for this problem and the calculations of Catherasoo & Sturtevant. The constant Mach number M_2 in figure 3.1 is determined by the accumulation of $I_i(t,0)$ (equation (3.2.5)) in the numerical scheme for the present calculations. This method gives $M_2 = 3.56$ for $M_1 = 5.0$. Catherasoo & Sturtevant use the exact value of $M_2 = 3.43$ as given by one-dimensional gas dynamics. Using this added piece of exact information imposes an additional constraint on the shockfront across the interface not present in geometrical shock dynamics. The different treatment of

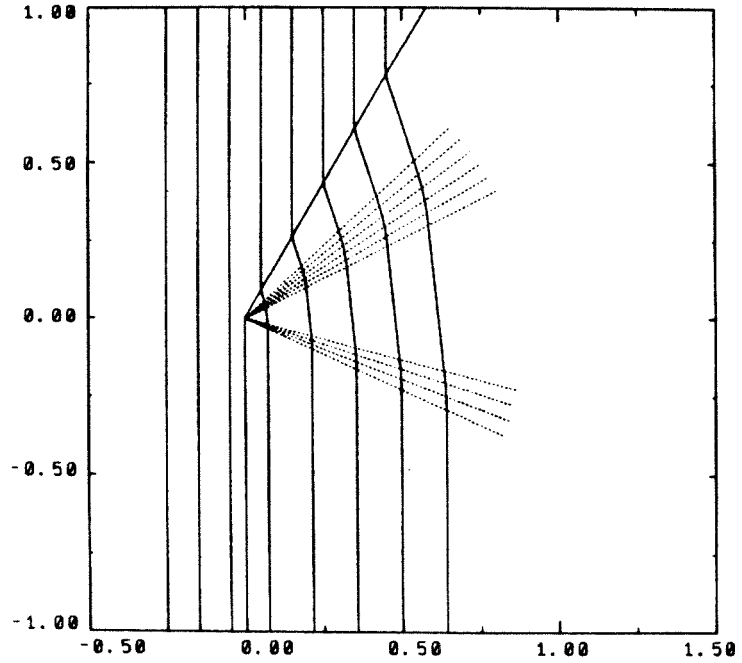

(a) $\delta_I = 60°$

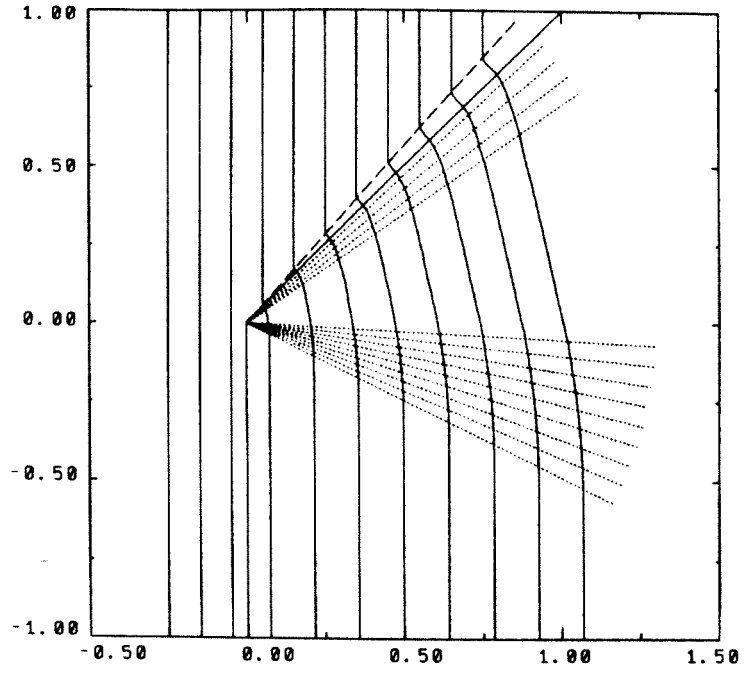

(b) $\delta_I = 45°$

FIGURE 3.2. Shock wave refraction at a planar interface for $M_1 = 5$ and $a_{02} = 2$.

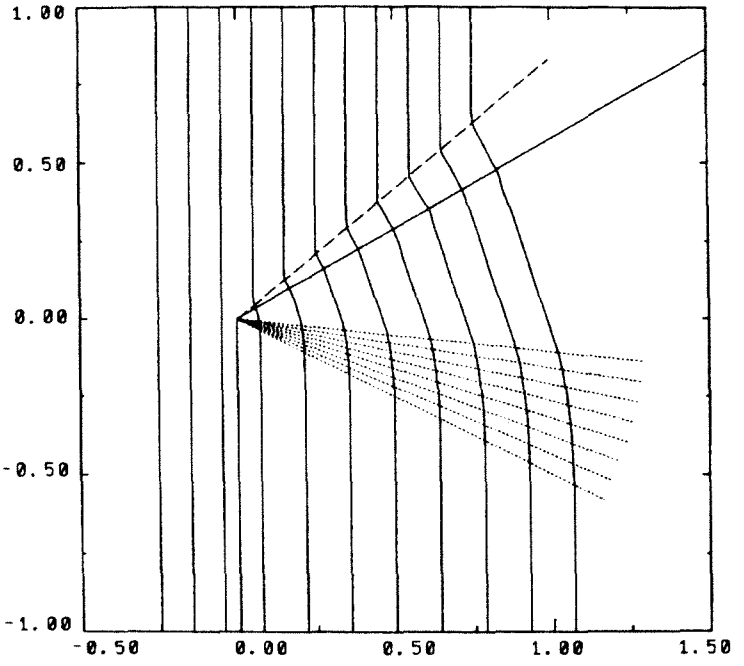

(c) $\delta_I = 30°$

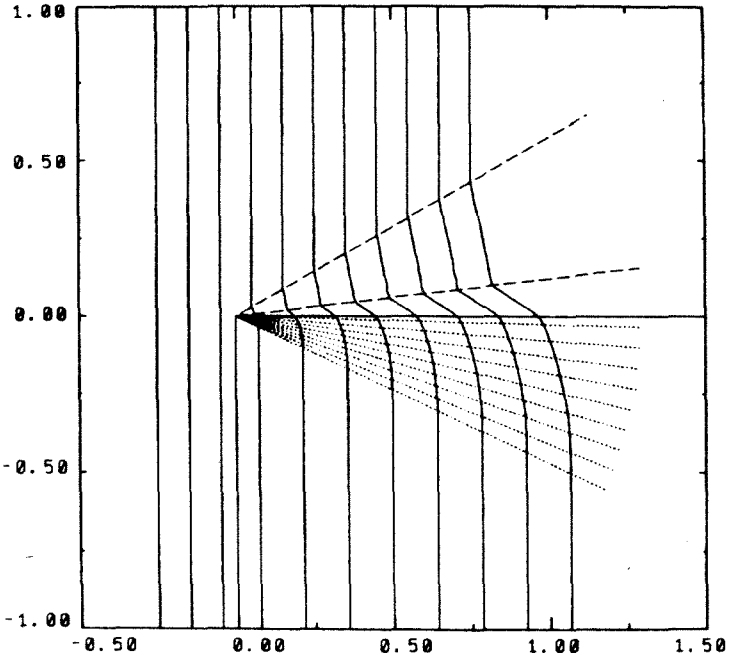

(d) $\delta_I = 0°$

FIGURE 3.2. (cont.). Shock wave refraction at a planar interface for $M_1 = 5$ and $a_{02} = 2$.

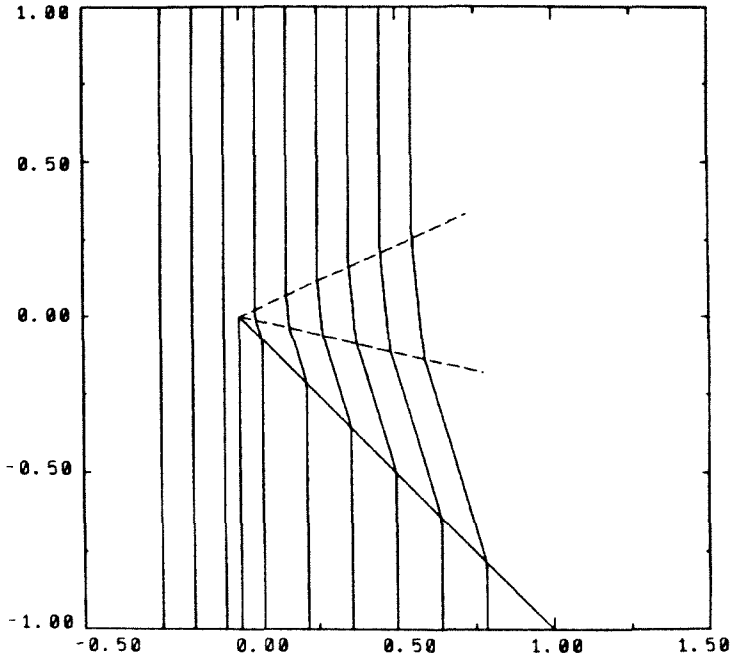

(e) $\delta_I = -45°$

FIGURE 3.2. (cont.). Shock wave refraction at a planar interface for $M_1 = 5$ and $a_{02} = 2$.

the shockfront across the boundary makes no difference in the qualitative picture of the shockfronts and little difference in any quantitative data. The only difference occurs for δ_I near the transition between regular and irregular refraction. In this region, Catherasoo & Sturtevant were unable to obtain a solution over a small range of δ_I. We note that for more complicated shock propagation problems, this extra information is not availible in general.

The position of the shock-shocks for a given interface inclination angle is perhaps the most interesting feature for this problem. These shock-shock positions are shown in figures 3.2b–e. We compare the angle between the shock-shock line and the x-axis with the results of Catherasoo & Sturtevant in table 3.3. The shock-shock angles χ_1 and χ_2 refer to the angles extracted from figures 3.2b–e, while χ_1' and χ_2' are the shock-shock angles given by Catherasoo & Sturtevant. The two

sets of data show reasonable agreement. We do not obtain exact agreement as a result of the different values of M_2 used across the interface.

δ_I	χ_1	χ_1'	χ_2	χ_2'
45°	48.7°	48.0°	—	—
30°	39.9°	38.9°	—	—
0°	29.9°	28.8°	6.9°	6.1°
−45°	25.0°	25.3°	−12.9°	−14.1°

TABLE 3.3. Comparison of shock-shock angles.

The transition from regular to irregular refraction arises naturally in the theory of geometrical shock dynamics for non-uniform media. This transition is seen in figures 3.2a and 3.2b as δ_I is decreased from 60° to 45°. The criterion for transition from regular to irregular refraction for this problem was given by Catherasoo & Sturtevant. Let the angle between the C_+ characteristic in the region just behind the inclined interface and the x-axis be denoted by δ_+. Regular refraction occurs for $\delta_I > \delta_+$. In this case, disturbances on the shockfront originating from the interface corner cannot propagate ahead of the C_+ expansion fan to the inclined interface. Thus, we have regions of constant M and θ on each side of the inclined interface separated by a sharp bend in the shockfront at the interface, implying the existence of regular refraction. For $\delta_I = \delta_+$, the edge of the C_+ expansion fan meets the inclined interface. Irregular refraction occurs for $\delta_I < \delta_+$ as a shock-shock forms ahead of the inclined interface.

In figure 3.2, we display only the refracted shockfronts for $a_{02} > a_{01}$. We do not discuss the case of $a_{02} < a_{01}$ for this simple problem, since the shockfront patterns for the two cases are similar and no new information is gained.

The geometry of the second problem we wish to study is shown in figure 3.4. This problem is similar to the previous problem except for the addition of a single

wall boundary. Thus, the effect of shock wave refraction by a planar interface on the propagating shockfront is now coupled with the effect of shock wave diffraction by a wedge previously considered in part (a) of section 2.4. The planar shock wave **S** travels along the wall with constant Mach number M_1. The planar interface **I** is inclined with an angle δ_I. The wedge angle is given by θ_w, and the Mach number along the inclined wall is denoted by M_w. The sound speed on either side of the interface is constant and given by a_{01} and a_{02} as before.

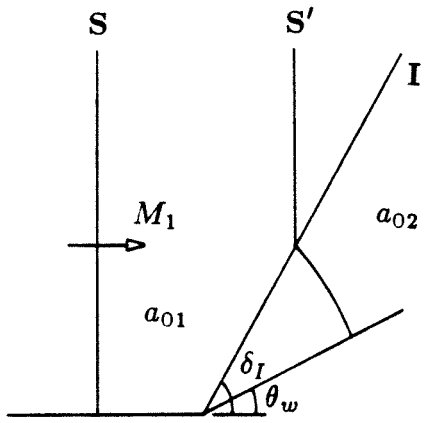

FIGURE 3.4. Interface-wall geometry.

Three typical examples of the shockfronts calculated for the second problem are given in figure 3.5. In all three cases, $a_{02} > a_{01}$. For $\delta_I = 60°$ and $\theta_w = 45°$, we see a sharp bend in the shockfront at the interface characteristic of regular refraction at the interface. The shockfront just behind the interface is planar with $M = 3.7$ and $\theta = 18.0°$. A shock-shock is present between the interface and the wall inclined at an angle $\chi = 56.6°$. These values agree with the values reported by Catherasoo & Sturtevant. It is also possible to compare these values with the curve given in figure 2.6 for strong shock diffraction by a wedge. The numerical results show that the refracted shockfront 'sees' a reduced wall angle

given by $45° - 18° = 27°$. This reduced value then gives $\chi = 57°$ from figure 2.6, which agrees with the calculated χ. The regular refraction seen in figure 3.5a is a local structure on the shockfront. If θ_w is decreased to 0° while holding δ_I fixed (figure 3.5b), we still have $M = 3.7$ and $\theta = 18°$ arcoss the interface. The shockfront adjustment to the wall, however, is not the same. We now find an expansion fan between the wall and the interface, instead of the shock-shock seen in figure 3.5a. In figure 3.5c, we observe irregular refraction similar to that which is seen in figure 3.2c, as δ_I is decreased to 30° and θ_w is increased to 15°.

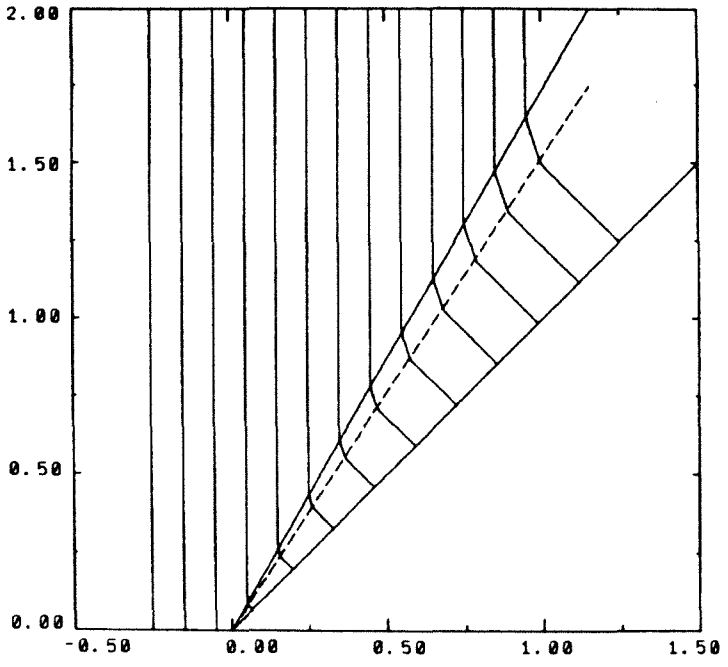

(a) $\delta_I = 60°$ and $\theta_w = 45°$

FIGURE 3.5. Shock wave refraction at a planar interface for $M_1 = 5$ and $a_{02} = 2$.

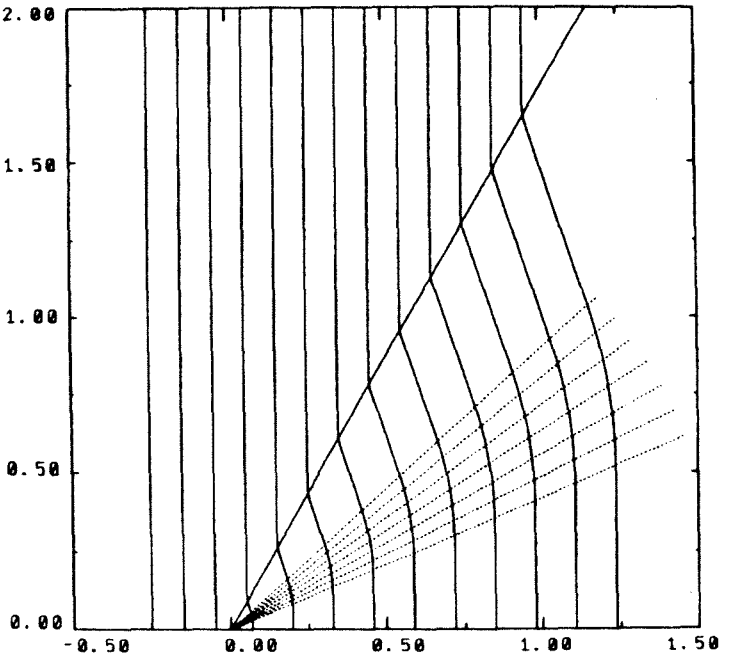

(b) $\delta_I = 60°$ and $\theta_w = 0°$

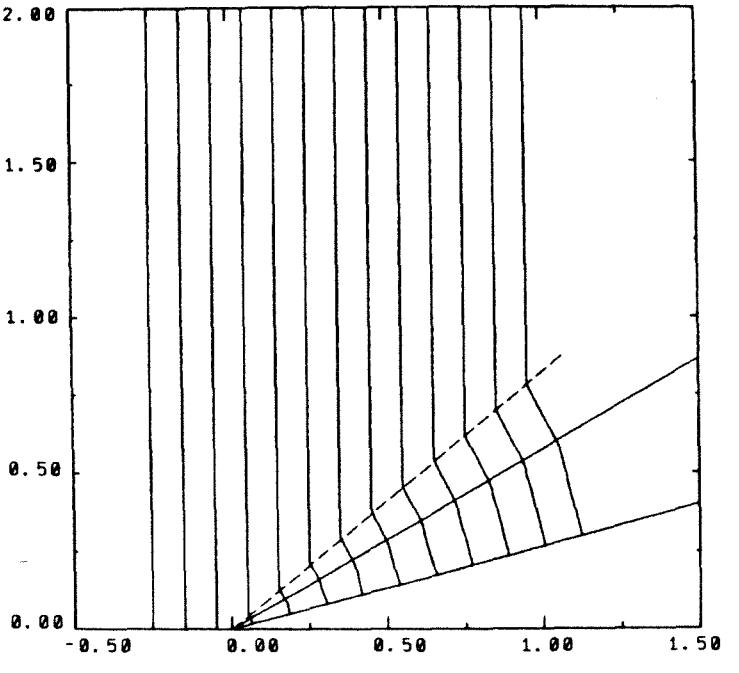

(c) $\delta_I = 30°$ and $\theta_w = 15°$

FIGURE 3.5. (cont.). Shock wave refraction at a planar interface for $M_1 = 5$ and $a_{02} = 2$.

In all cases considered so far, we have examined the behavior of the shockfronts for fixed initial shock strength and varying interface-wall geometry. It is also interesting to study the effect of decreasing the initial shock strength while holding the interface-wall geometry fixed. We display the effect of decreasing M_1 in figure 3.6. The particular interface-wall geometry chosen is $\delta_I = 30°$ and $\theta_w = 0°$. In figures 3.6a–c, a single shock-shock forms ahead of the interface. The shockfront behind the interface is composed of a centered expansion fan just behind the interface and planar shockfront at the wall. As M_1 is decreased, the expansion fan grows until it meets the wall for $M_1 = 1.75$. The wall Mach number also decreases from $M_w = 2.8$ for $M_1 = 5.0$ to $M_w \approx 1$ for $M_1 = 1.75$. A further decrease in the incident shock strength (figures 3.6d–e) results in the formation of a second shock-shock and a *precursor wave* just in front of the interface. The precursor wave connects the very weak shock (essentially a sonic circle) behind the interface with the incident shock wave ahead through a series of two shock-shocks.

The precursor shockfront pattern (figures 3.6d–e) calculated using the present numerical scheme was not found by Catherasoo & Sturtevant. They calculated shockfronts using the interface-wall geometry of figure 3.6 for M_1 between 5.0 and 1.77 in agreement with our results. For $M_1 < 1.77$, they were unable to construct a solution to the equations of geometrical shock dynamics. The method of constructing solutions used by Catherasoo & Sturtevant requires some initial 'quess' for the desired solution. An iteration procedure is then applied until all the equations (jump conditions and characteristic equations) are satisfied simultaneously. The present numerical scheme requires no prior knowledge of the solution. This exemplifies one advantage of using the general numerical scheme presented in section 3.2.

Overall, the refracted shockfronts found using geometrical shock dynamics are in good agreement with experimental results. A detailed comparison with

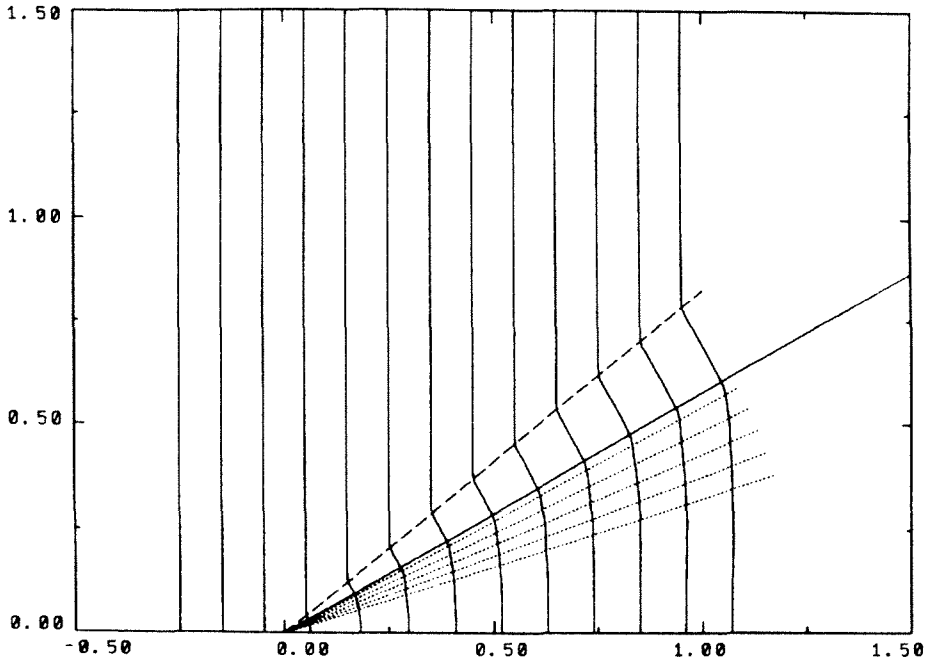

(a) $M_1 = 5.0$

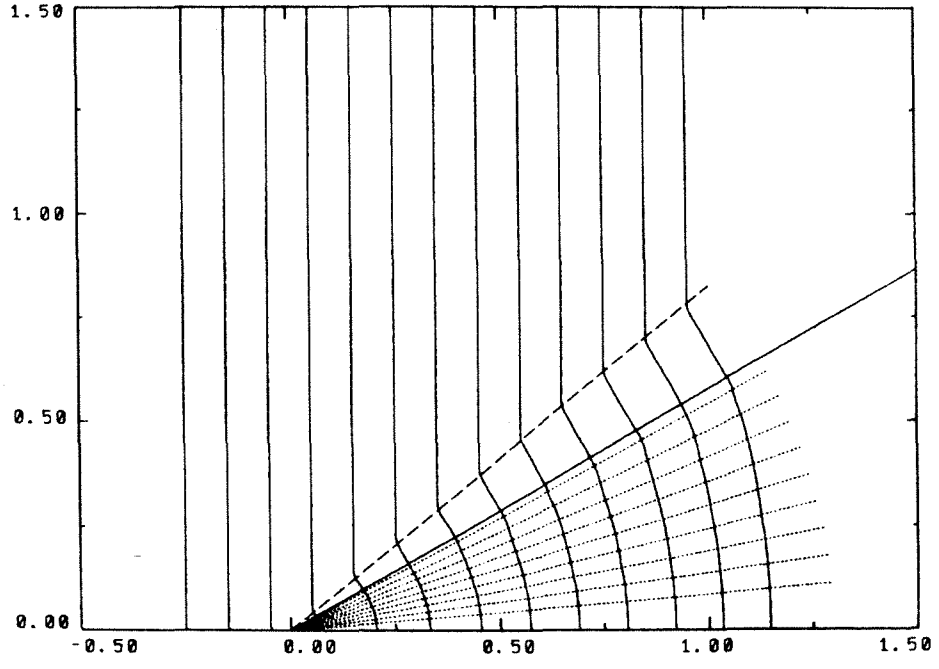

(b) $M_1 = 2.0$

FIGURE 3.6. Shock wave refraction at a planar interface for $\delta_I = 30°$, $\theta_w = 0°$ and $a_{02} = 2$.

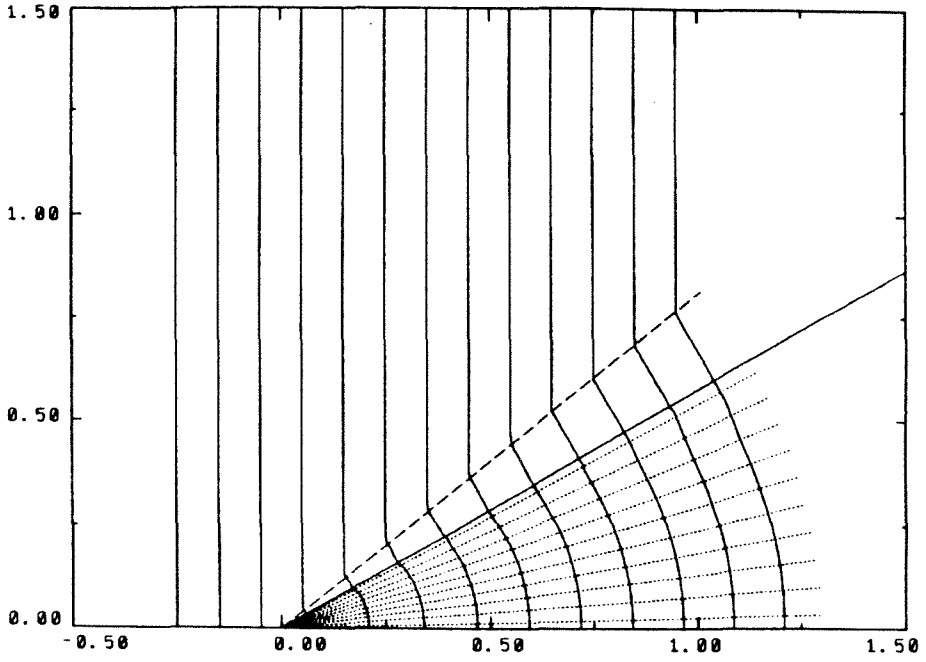

(c) $M_1 = 1.75$

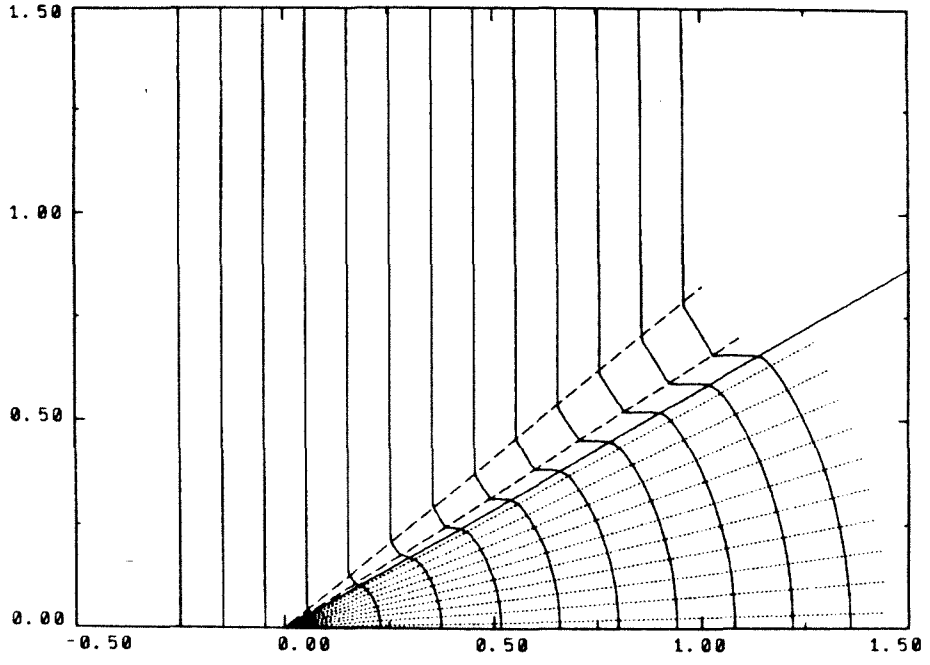

(d) $M_1 = 1.5$

FIGURE 3.6. (cont.). Shock wave refraction at a planar interface for $\delta_I = 30°$, $\theta_w = 0°$ and $a_{02} = 2$.

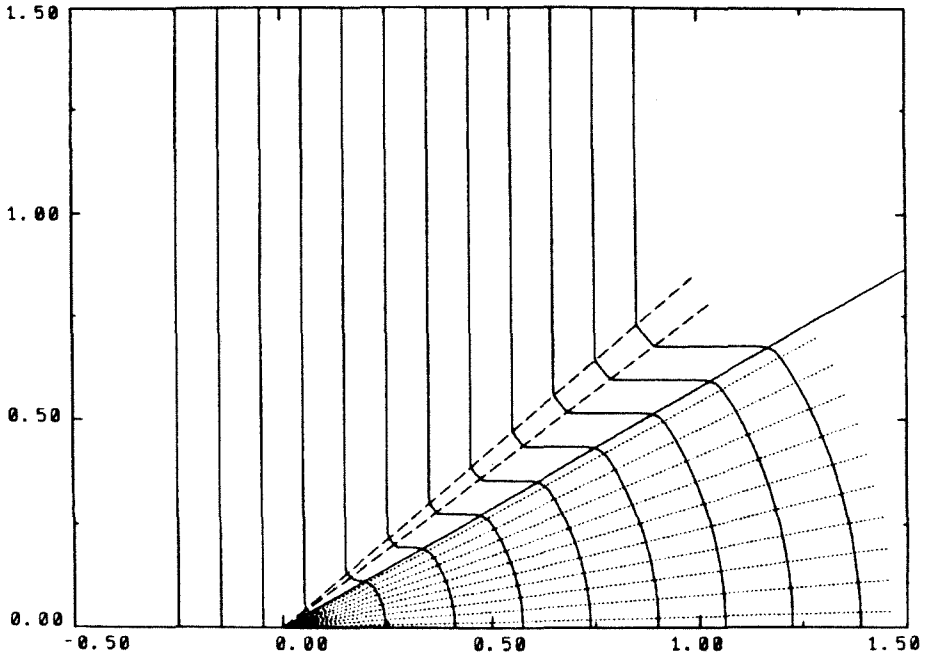

(e) $M_1 = 1.25$

FIGURE 3.6. (cont.). Shock wave refraction at a planar interface for $\delta_I = 30°$, $\theta_w = 0°$ and $a_{02} = 2$.

the experimental data of Jahn [1956], Abd-el-Fattah, Henderson & Lozzi [1976] and Abd-el-Fattah & Henderson [1978] may be found in Catherasoo & Sturtevant [1983]. Generally, Catherasoo & Sturtevant show that geometrical shock dynamics is able to predict the transition from regular to irregular refraction accurately as well as giving accurate triple-point (shock-shock) positions. Abd-el-Fattah & Henderson [1978] also report the same precursor-irregular refraction patterns as those shown in figures 3.6d–e.

Before moving on to the next problem, we display a representative picture of the refracted shockfronts for $a_{02} < a_{01}$ (figure 3.7). For the example shown, $\delta_I = 30°$, $\theta_w = 0°$ and $a_{02}/a_{01} = 0.5$. The shockfront bends sharply backwards at the interface as the shockfront enters the region of 'slower' gas. The adjustment to

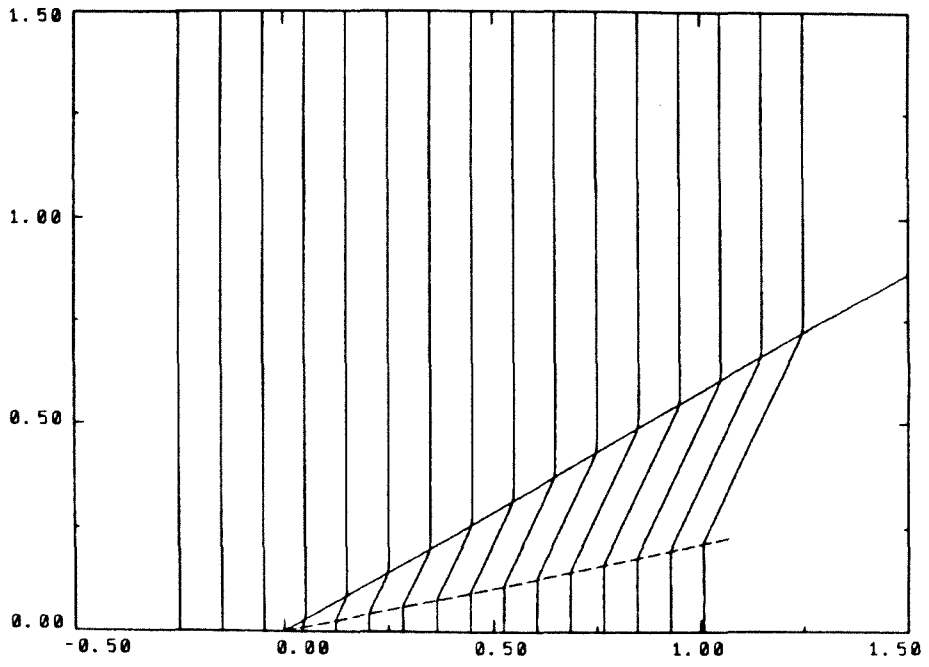

FIGURE 3.7. Shock wave refraction at a planar interface for $M_1 = 5$, $\delta_I = 30°$, $\theta_w = 0°$ and $a_{02} = 0.5$.

the boundary condition at the wall is made through a shock-shock. This pattern is characteristic of all the cases considered for $a_{02} < a_{01}$.

(b) Shock Wave Refraction by Cylinders and Spheres

In this subsection, we study the case of shock wave refraction at a gaseous interface of cylindrical or spherical geometry. These problems contain at least one length scale, namely, the radius of the cylinder or sphere, as opposed to the two self-similar problems previously considered. This fact presents no added difficulty for the numerical scheme of section 3.2. The method of constructing solutions using characteristics, however, is much more difficult, since there exist regions of nontrivial shock geometries and strengths. For this problem, we compare the results found using the present numerical scheme with experimental observations only. We know of no other theoretical solutions to this problem.

Haas & Sturtevant [1986] experimentally investigated the problem of shock wave refraction by cylinders and spheres. Cylindrical membranes or spherical bubbles were filled with helium or freon-22 and suspended in a shock tube. Weak planar shock waves (incident Mach number ≤ 1.25) were propagated down the shock tube. The shock wave refraction patterns and interface deflections were observed. For the present work, we are mainly interested in the shockfront patterns observed experimentally by Haas & Sturtevant. In the case of a helium-filled cylinder or sphere, the incident shockfront bulged foward as it crosed the interface, since the sound speed of helium (a_{He}) is greater than that of air (a_{air}). Regular refraction at the interface was observed during the first stages of the interaction. Later, transition to irregular refraction was seen as a triple-point (shock-shock) formed near the interface in the surrounding air. For the freon-filled cylinder or sphere, the refracted shockfront lagged behind the incident front, since $a_{freon} < a_{air}$. Regular refraction was always present at the interface. Inside the cylinder or sphere, strong internally diffracted shockfronts were observed. These waves focused and crossed as they neared the back of the cylinder or sphere.

We first treat the case of shock wave refraction by a cylindrical interface. We use the following distribution of sound speed for the present calculations:

$$a_0(r) = \begin{cases} 1 & \text{if } r - R \geq R_I; \\ \frac{1}{2}\left[(1 + a_{02}) + (1 - a_{02})\sin\left(\frac{\pi}{2}\frac{r-R}{R_I}\right)\right] & \text{if } |\, r - R\,| < R_I; \\ a_{02} & \text{if } r - R \leq -R_I, \end{cases} \tag{3.3.1}$$

where r is the radial distance from the center of the cylinder, R is the radius of the cylinder and R_I measures the width of the cylindrical interface. The sound speed inside the cylinder is a_{02}, and the sound speed outside is normalized to one. For the first set of results, we take $R_I = .01$ to compare with experimental observations where the cylindrical interface is thin. Later, we study shock wave refraction for varying R_I.

In figure 3.8, we show our results for the helium-filled cylinder. For helium, the normalized sound speed a_{02} in (3.3.1) is 2.9. The incident Mach number is 1.22, which was also used experimentally. Near the cylindrical interface, the behavior of the refracted shockfront is similar to those seen for the planar interface. Regular refraction is observed when the shockfront first meets the interface, since the interface inclination angle is large. As this angle decreases, transition to irregular refraction is observed. These flow features were also found experimentally by Haas & Sturtevant. The shockfront emerges from the cylinder convex forward. The helium-filled cylinder acts as a divergent lens for planar incident shock waves.

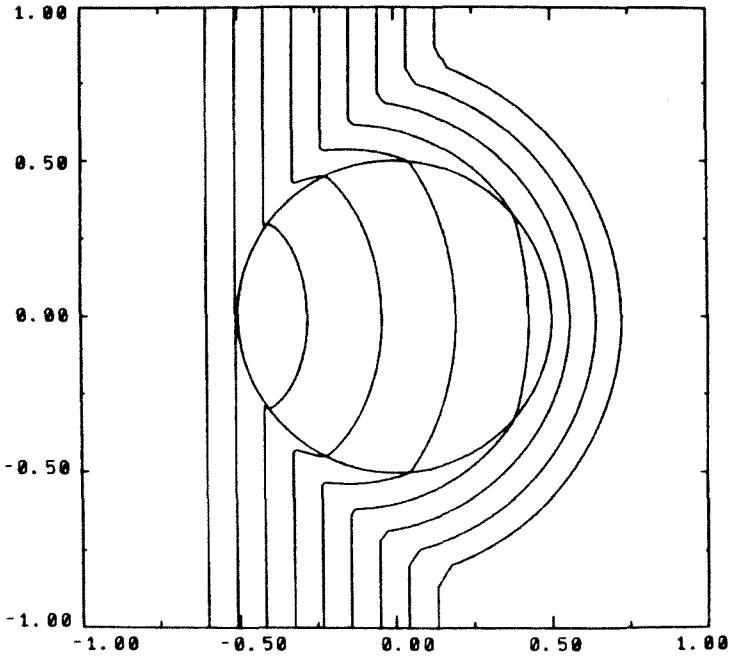

FIGURE 3.8. Shock wave refraction at a cylindrical interface for $a_{02} = 2.9$ (helium-filled cylinder) with $M_0 = 1.22$ and $R_I = .01$.

We display the calculations for the freon-filled cylinder in figure 3.9. For freon-22, $a_{02} = 0.53$, and we use $M_0 = 1.22$ as before. The freon-filled cylinder acts as a convergent lens in gas dynamics. The central portion of the incident shockfront

refracts at the cylindrical interface. The refracted shockfront is concave forward. The edges of the refracted front are turned more rapidly than the central portion by the faster traveling shockfront outside of the cylinder. As a result, two focusing shockfront systems (similar to the focusing shockfronts of section 2.4, part (c)) are seen inside the cylinder. If a_{02} is small enough, as is the case here, the shockfronts on the interface cross before the refracted shockfront reaches the back of the cylinder. All of these features are observed experimentally by Haas & Sturtevant. In particular, they note the strong internally diffracted waves predicted by geometrical acoustics (the 'dark' shocks in figure 3.11b). These waves are also given by geometrical shock dynamics. They are the rapidly turning edges of the refracted shockfront seen in figure 3.9.

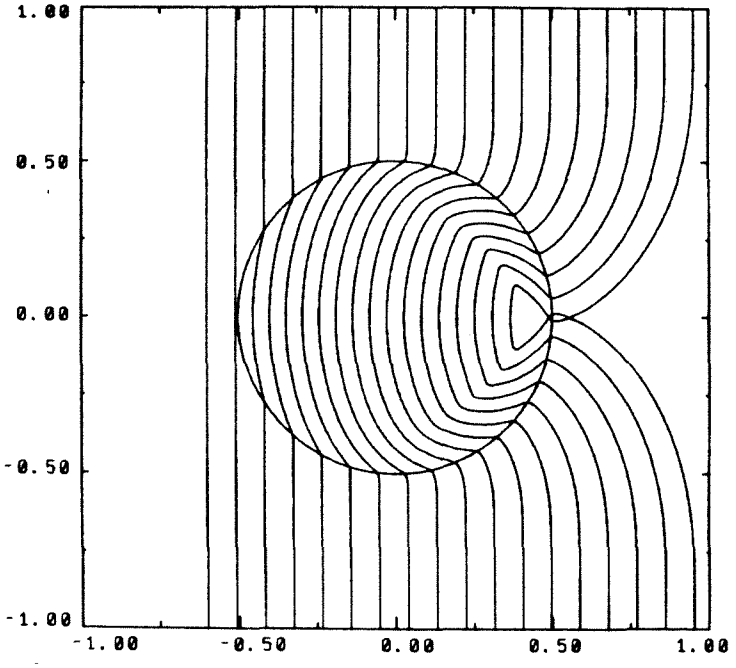

FIGURE 3.9. Shock wave refraction at a cylindrical interface for $a_{02} = .53$ (freon-filled cylinder) with $M_0 = 1.22$ and $R_I = .01$.

Shadowgraphs of the two cylinder cases considered are shown in figures 3.10 and 3.11. These pictures were obtained experimentally by Haas & Sturtevant [1986]. The shadowgraphs show the shock system and interface deflection at a particular instant in time, whereas our plots show the shockfronts at several instances in time. The helium-filled cylinder is displayed in figure 3.10 and the freon-filled cylinder is shown in figure 3.11. In general, we note the good agreement with shockfronts calculated using geometrical shock dynamics. It is also interesting to note the extremely complicated flow behind the shockfront.

A further study of the refraction process is obtained by varying the interface thickness R_I in equation (3.3.1). This study has not been performed experimentally. In figure 3.12, we vary R_I from $R_I = .1$ to $R_I = R = .5$. The incident Mach number is $M_0 = 1.22$ and the sound speed inside the cylinder is $a_{02} = 0.53$. The case of a sharp jump in sound speed at the cylindrical interface ($R_I = .01$) is shown in figure 3.9. In all three pictures, we plot a circle of radius R for reference. For $R_I = .01$ (figure 3.9), we noted the strong internally diffracted waves inside the cylinder. These waves crossed near the back of the cylinder. As R_I is increased, these waves are less pronounced, resulting in a weaker focus for the refracted shockfront near the back of the cylinder. The three different values of R_I shown in figure 3.12 give the three different types of focusing. For $R_I = .1$, the refracted shockfronts cross near the back of the cylinder. The refracted shockfronts for $R_I = .25$ emerge from the cylinder uncrossed and later focus to form a single shock-shock on the axis of symmetry. This focusing mechanism is similar to that discussed in section 2.4, part (c). The weakest focusing is observed for $R_I = R = .5$ (figure 3.12c) as the refracted front forms a Mach stem behind the cylinder.

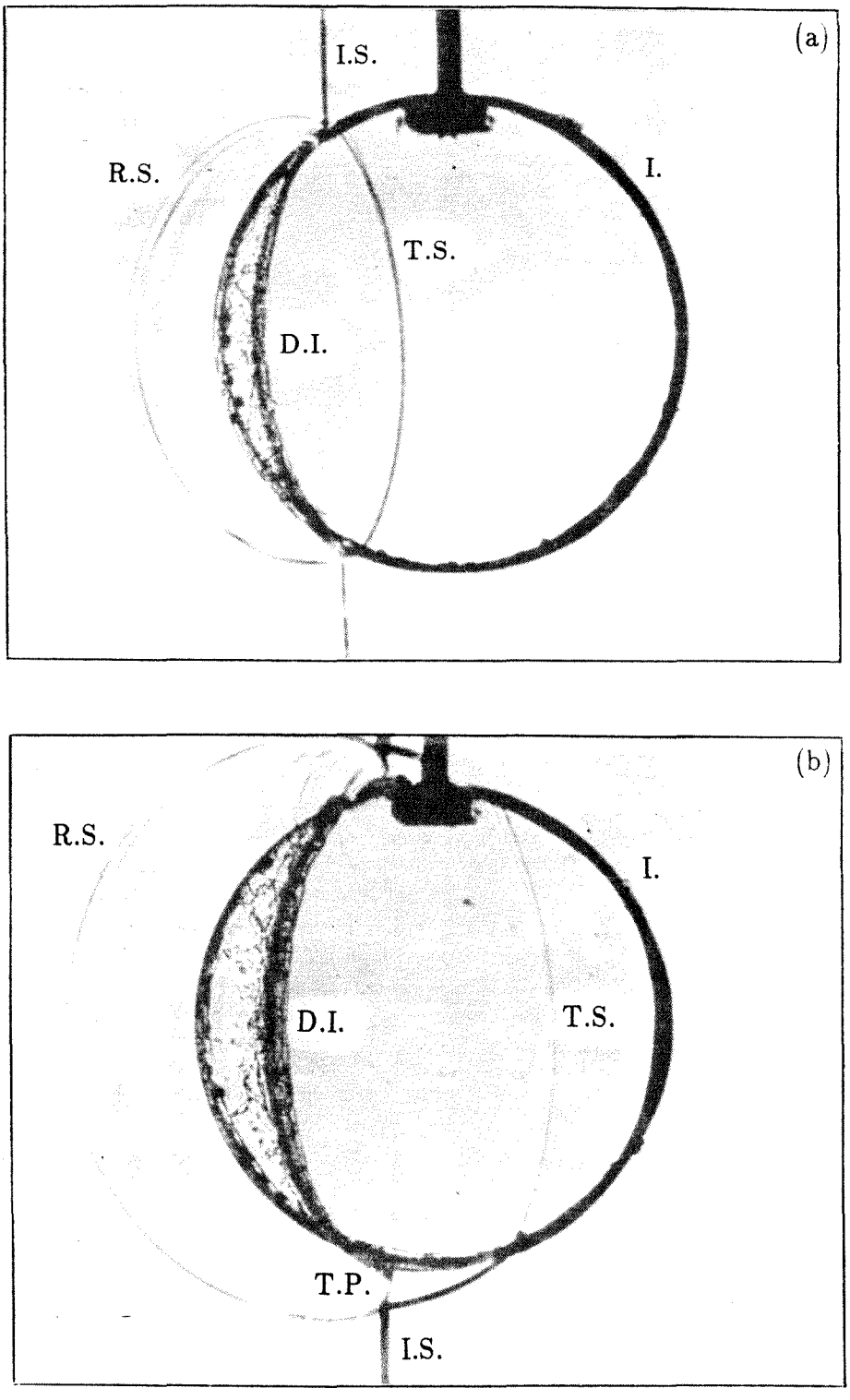

FIGURE 3.10. Shadowgraphs of shock wave refraction by a helium-filled cylinder, $M_0 = 1.22$: (a) time $= t_a$; (b) time $= t_b > t_a$. Notation: I., interface; D.I., deflected interface; I.S., incident shock; R.S., reflected shock; T.S., transmitted shock; T.P., triple-point. (Haas & Sturtevant, 1986).

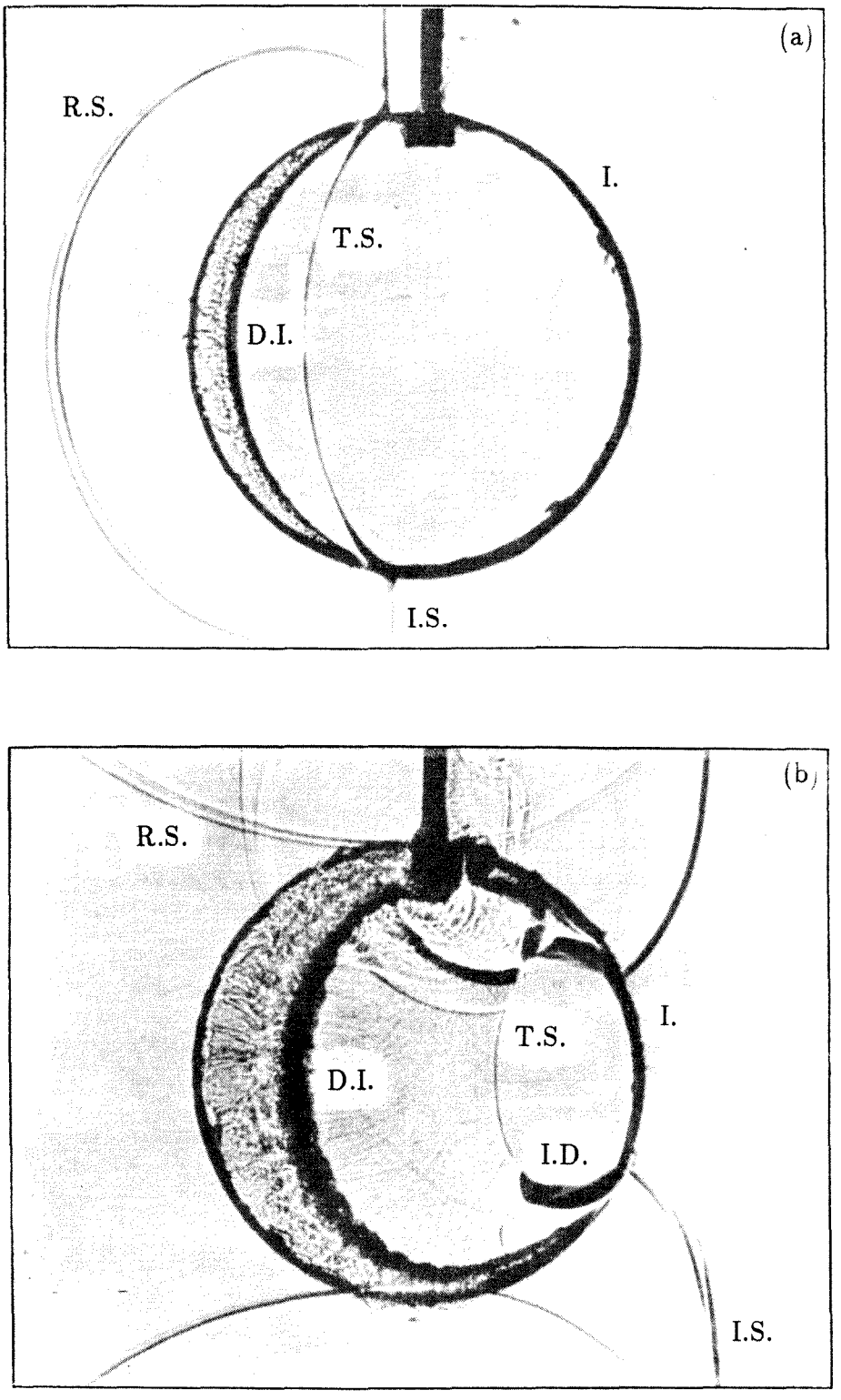

FIGURE 3.11. Shadowgraphs of shock wave refraction by a freon-filled cylinder, $M_0 = 1.22$: (a) time $= t_a$; (b) time $= t_b > t_a$. Same notation as figure 3.10 adding I.D., internally diffracted waves. (Haas & Sturtevant, 1986).

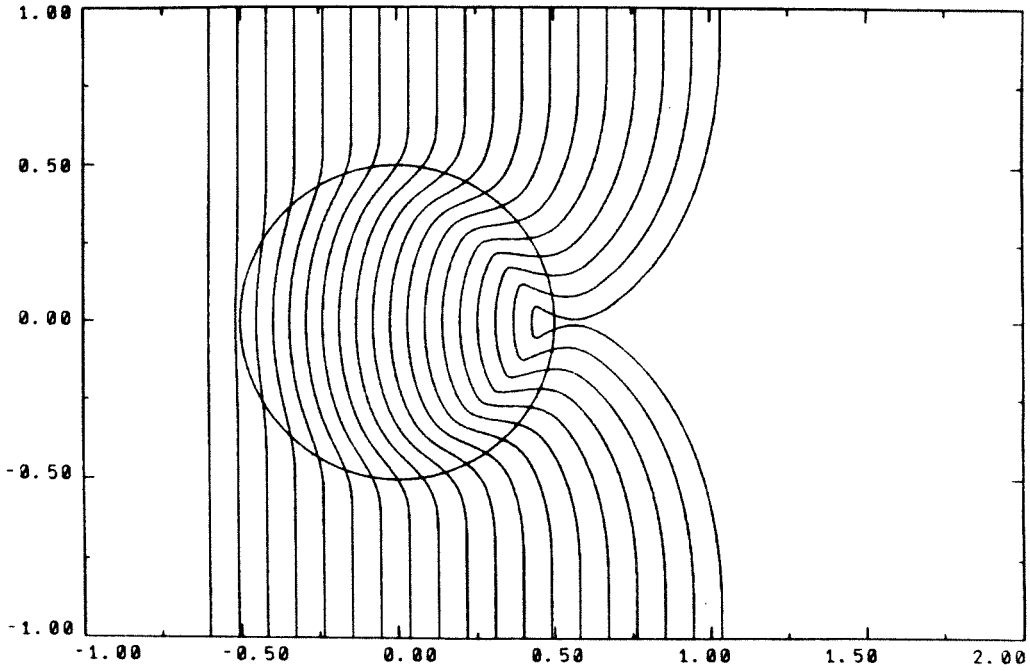

(a) $R_I = .1$

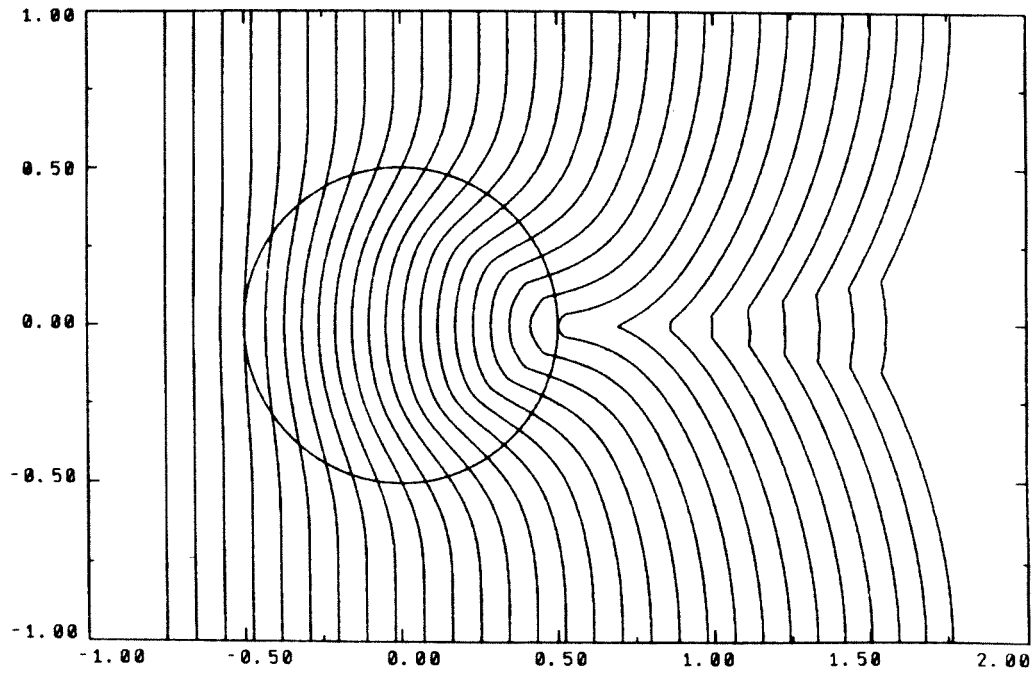

(b) $R_I = .25$

FIGURE 3.12. Shock wave refraction at a cylindrical interface for $M_0 = 1.22$ and $a_{02} = .53$.

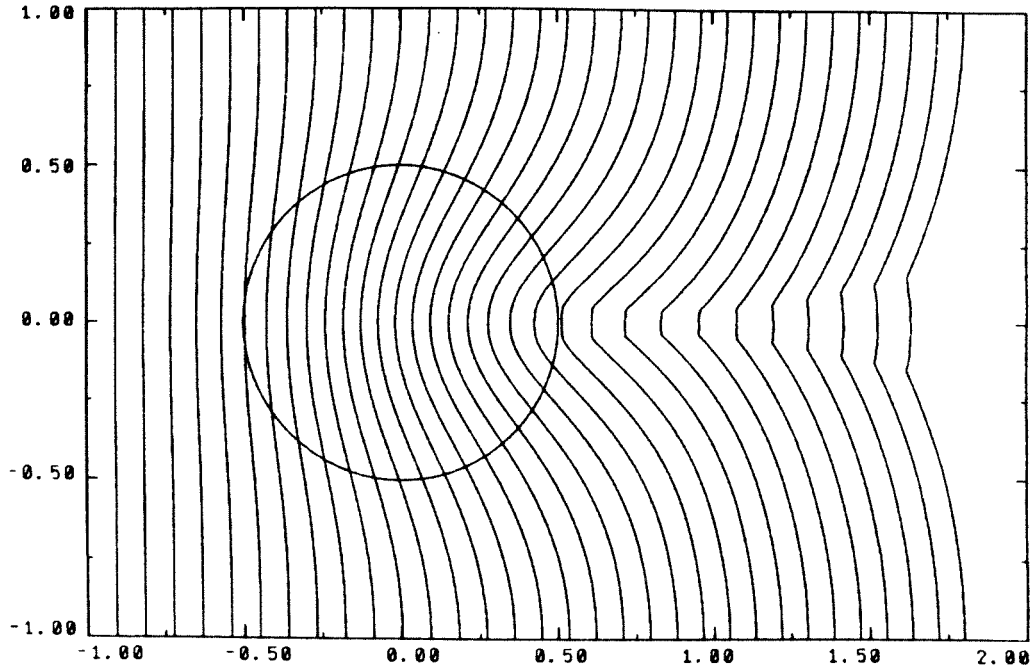

(c) $R_I = .5$

FIGURE 3.12. (cont.). Shock wave refraction at a cylindrical interface for $M_0 = 1.22$ and $a_{02} = .53$.

For completeness, we show the shock wave refraction patterns given at spherical interface. The variation in sound speed given by (3.3.1) for the cylinder case is also used here. The diverging case ($a_{02} = 2.9$) is displayed in figure 3.13a, and the converging case ($a_{02} = 0.53$) is given in figure 3.13b. We take $M_0 = 1.25$ for both plots. These cases were also considered experimentally by Haas & Sturtevant. The refraction process for the sphere is found to be very similar to that of the cylinder (figures 3.8 and 3.9). Photographs of the refraction process for the actual shock waves show this similarity as well.

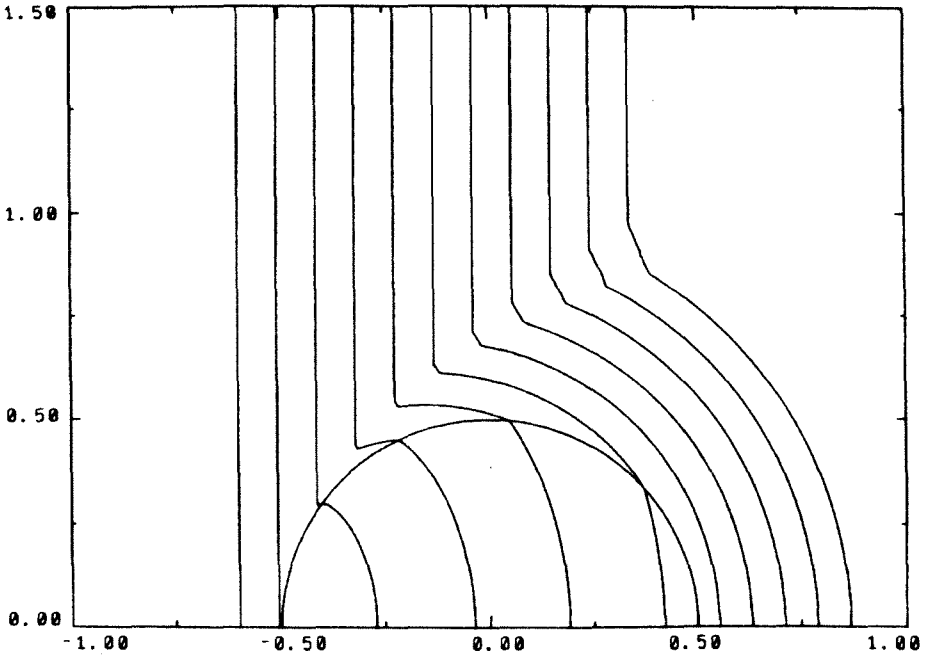

(a) $a_{02} = 2.9$ (helium-filled sphere)

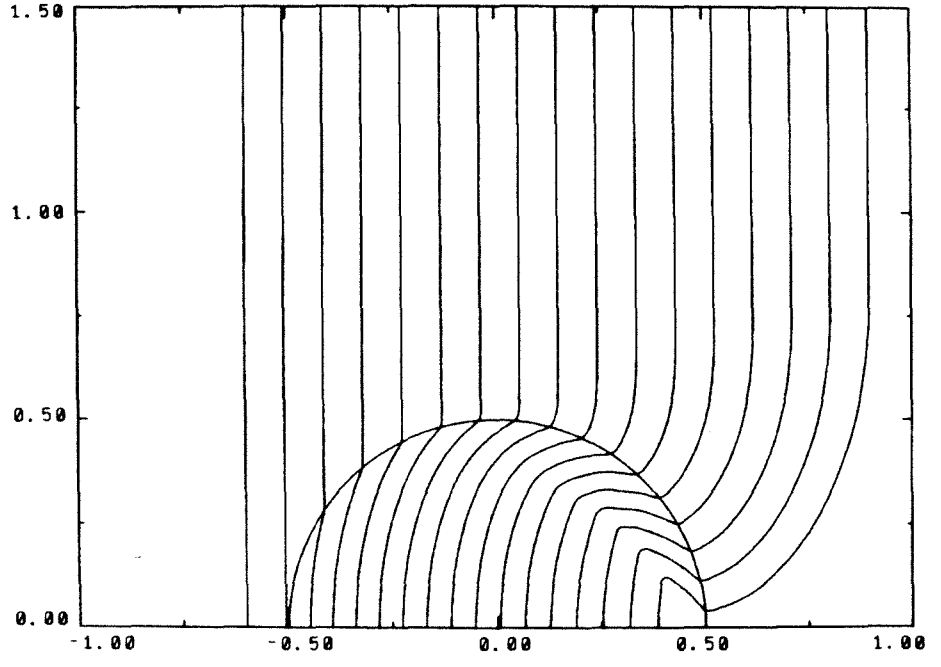

(b) $a_{02} = .53$ (freon-filled sphere)

FIGURE 3.13. Shock wave refraction at a spherical interface for $M_0 = 1.25$ and $R_I = .01$.

CHAPTER 4

Three-dimensional Shock Propagation

4.1 Introduction

In this chapter, we turn our attention to the general problem of shock wave propagation in three space dimensions. As before, we use the approximate theory of geometrical shock dynamics to determine the motion of the shock. The ideas behind this approximate theory and the corresponding numerical scheme for shock propagation in two dimensions have been discussed in detail in the previous chapters. For three dimensions, the same ideas apply; only the numerical scheme becomes more complicated. The two-dimensional numerical scheme may be viewed as an approximate method for propagating small elements of the entire shock according to the rules of geometrical shock dynamics. The same view is taken in the development of the three-dimensional scheme, but now we approximate small pieces of the shockfront surface by triangular surface elements. The local triangular element construction is particularly convenient in that we can handle a variety of overall shockfront geometries. Also, the refinement on the shockfront surface (i.e., merging or splitting triangular elements), needed especially as shock-shocks develop, may be handled using the triangular element construction.

We present the numerical scheme used to calculate successive shockfronts for the general three-dimensional problem in section 4.2. The shockfront surface is approximated by a discrete set of points, where each point belongs to an adaptive mesh composed of triangular elements. The numerical scheme propagates each

point along its surface normal with a speed given by the discrete version of the A-M relation. A mesh refinement scheme is employed to maintain a relatively even point spacing on the triangulated shock surface. This refinement scheme automatically inserts points (splits triangles) in expansive regions of the shockfront and deletes points (merges triangles) in compressive regions of the shockfront. Shock-shocks are fitted in compressive regions of the shockfront by deleting points. The shockfront surface is smoothed periodically in order to dampen high frequency numerical fluctuations.

Two fundamental shock propagation problems are considered in section 4.3 primarily to demonstrate the use of the numerical scheme in three dimensions. The first problem we examine is shock wave focusing. We perform a numerical test of the accuracy of the numerical scheme presented in section 4.2 by first considering an axisymmetric focusing problem. We compare the results obtained using the new three-dimensional scheme with the assumed solution calculated using the axisymmetric version of the two-dimensional numerical scheme. We then move on to general three-dimensional focusing cases and discuss the results. The second problem we study is shock wave propagation around a 90° bend in a pipe with circular cross section. This problem is an extension of the two-dimensional channel problems considered in section 2.4, part (b). The pipe problem requires the numerical treatment of walls, which is an added feature of the numerical scheme not tested in the previous focusing problem. We find interesting shock diffraction effects in the pipe not seen in the two-dimensional channel.

As in two dimensions, the shockfronts may develop shock-shocks; i.e., discontinuities in Mach number and normal direction. In three dimensions, the shock-shock are curves on the shock surface. As before, they signal the formation of a Mach stem and reflected shock for the actual shock.

We assume that the gas ahead of the moving shock is uniform and at rest for all the problems considered in this chapter. The extension to problems of non-uniform media discussed in Chapter 3 could be included in the three-dimensional numerical scheme. Clearly, the extension affects only the Mach number calculation and is independent of the number of dimensions. In order to demonstrate the use of the new numerical scheme for three-dimensional shock propagation problems, we need consider only uniform media.

4.2 Numerical Scheme

We now discuss in detail the numerical scheme developed to calculate successive shockfronts in three dimensions. Overall, the scheme is analogous to the numerical scheme developed for shock wave propagation in two space dimensions (section 2.3). The components of the three-dimensional scheme are new, however, and we will need to describe each in detail.

An illustration of the numerical time marching procedure used to calculate the shockfront surfaces is shown in figure 4.1. The shockfront at time t is described by a discrete set of points. Each point on the mesh is advanced along its surface normal with a speed specified by the discrete version of the A-M relation. In order to monitor the point spacing and calculate the Mach number and surface normal at $\mathbf{x}_i(t)$, it is convenient to introduce an adaptive mesh composed of triangular elements. (See later.) Points are inserted or deleted on the shockfront surface in order to maintain a relatively even point spacing. Also, as shock-shocks form in compressive regions of the shockfront, points are deleted in order to fit the shock-shocks into the front. A smoothing procedure is applied periodically to dampen high frequency numerical errors in the shockfront position.

We approximate the shockfront surface by a discrete set of points $\mathbf{x}_i(t), i = 1, \ldots, N$. The assumption in the theory of geometrical shock dynamics that each

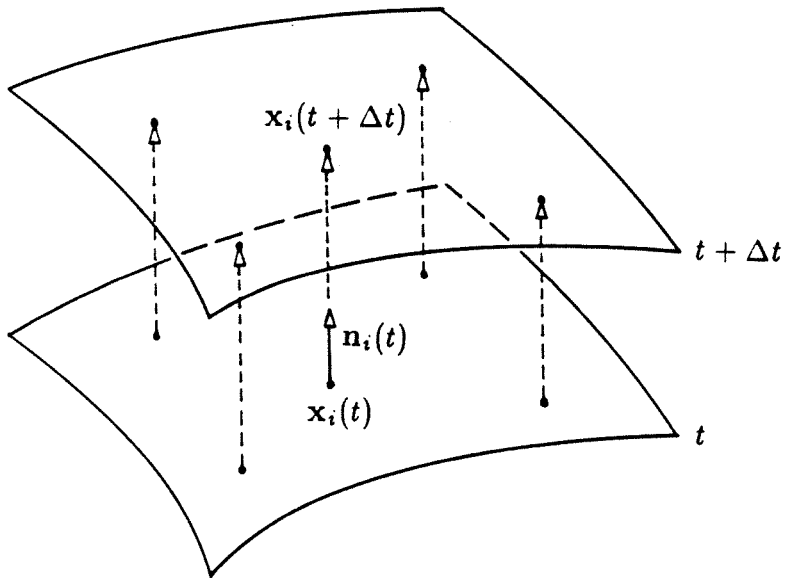

FIGURE 4.1. Three-dimensional time marching scheme. Shock surfaces at t and $t+\Delta t$ and approximate rays (dashed lines).

point on the shockfront propagates along rays normal to the shockfront surface gives immediately

$$\frac{d}{dt}\mathbf{x}_i(t) = a_0\, M_i(t)\, \mathbf{n}_i(t), \qquad i = 1,\ldots,N, \tag{4.2.1}$$

where $M_i(t)$ and $\mathbf{n}_i(t)$ approximate the Mach number and unit surface normal at $\mathbf{x}_i(t)$, respectively. We choose to integrate the system of O.D.E.'s in (4.2.1) numerically using the leap-frog scheme

$$\mathbf{x}_i(t+\Delta t) = \mathbf{x}_i(t-\Delta t) + 2\Delta t\, M_i(t)\, \mathbf{n}_i(t) \qquad i = 1,\ldots,N, \tag{4.2.2}$$

where $t = n\Delta t$, $n = 0,\ldots,T/\Delta t$ and we normalize a_0 to one. The time marching scheme in (4.2.2) is the same scheme used to propagate the shockfronts in two dimensions and the advantages for using (4.2.2), discussed in section 2.3, apply here as well.

It is convenient to introduce an adaptive mesh on the shockfront surface composed of triangular elements. A sketch of the triangulated mesh in the vicinity of the point $\mathbf{x}_i(t)$ is provided in figure 4.2. The triangular mesh construction allows for a relatively simple calculation of $M_i(t)$ and $\mathbf{n}_i(t)$. These quantities are required in the time marching scheme (4.2.2). The point $\mathbf{x}_i(t)$ lies at the vertex of $m_i(t)$ triangles. The number $m_i(t)$ is allowed to change in time as the mesh adapts to the expanding or compressing surface of the shockfront. The necessary mesh refinement, discussed in detail later, is also possible for this particular mesh. A further advantage in using the triangulated mesh is its ability to handle general initial shockfront shapes. This point is demonstrated in the shock propagation problems considered in section 4.3.

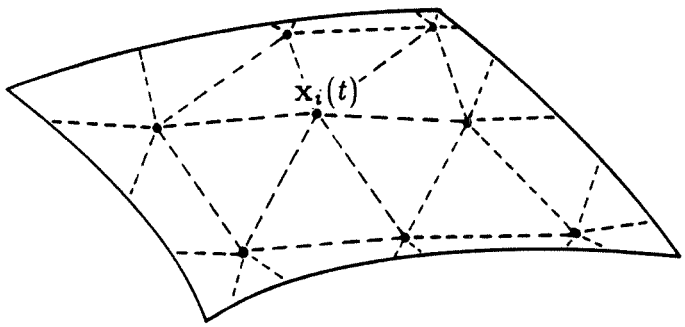

FIGURE 4.2. Triangulated mesh on the shock surface.

The triangulated mesh is defined via two integer functions which locally connect points with their bordering triangles and vice versa. Each point is numbered from $i = 1, \ldots, N$ and each triangle is numbered from $j = 1, \ldots, J$. Overall, we have $J \approx 2N$. Let $\mu(k, i)$, $k = 1, \ldots, m_i(t)$ give the number of the k^{th} triangle with one vertex at the point $\mathbf{x}_i(t)$. Conversely, we let $\nu(l, j)$, $l = 1, 2, 3$ give the number of the three points at the vertices of the j^{th} triangle. Clearly, the two

functions are not independent and only one is necessary to define the mesh. In practice, however, we find it useful to work with both μ and ν. This gains speed in the numerical scheme (fewer index searches are required) at the expense of increased integer storage requirements.

The Mach number $M_i(t)$ in (4.2.2) is determined by solving the discrete version of the A-M relation

$$\frac{A_i(t)}{A_i(0)} = \frac{f\big(M_i(t)\big)}{f\big(M_i(0)\big)} \qquad \text{for } i = 1, \ldots, N. \tag{4.2.3}$$

Equation (4.2.3) specifies $M_i(t)$ implicitly in terms of $M_i(0)$ and the area ratio $A_i(t)/A_i(0)$. In the limit of weak shocks or strong shocks, we find $M_i(t)$ explicity using (2.2.3) and (2.2.4), respectively. For weak shocks

$$M_i(t) = 1 + (M_i(0) - 1)\left(\frac{A_i(0)}{A_i(t)}\right)^{1/2} \qquad \text{for } i = 1, \ldots, N, \tag{4.2.4}$$

and for strong shocks

$$M_i(t) = M_i(0)\left(\frac{A_i(0)}{A_i(t)}\right)^{1/n} \qquad \text{for } i = 1, \ldots, N, \tag{4.2.5}$$

where $n = 5.0743$ for air ($\gamma = 1.4$). The approximate ray tube area $A_i(t)$ is determined by averaging the areas of the $m_i(t)$ triangles bordering the point $\mathbf{x}_i(t)$. We find

$$A_i(t) = \frac{1}{m_i(t)} \sum_{k=1}^{m_i(t)} S_{\mu(k,i)}(t), \tag{4.2.6}$$

where the area of each triangle is given by

$$S_j(t) = \frac{1}{2}\left|\big(\mathbf{x}_{\nu(2,j)}(t) - \mathbf{x}_{\nu(1,j)}(t)\big) \times \big(\mathbf{x}_{\nu(3,j)}(t) - \mathbf{x}_{\nu(1,j)}(t)\big)\right|. \tag{4.2.7}$$

The surface normal $\mathbf{n}_i(t)$ at the point $\mathbf{x}_i(t)$ may be found by calculating an appropriately weighted average of the bordering triangle normals. The union of the triangular surface elements about the point $\mathbf{x}_i(t)$ approximately maps out a narrow ray tube in time. We therefore wish to obtain an expression for the normal

about the center of the ray tube. Let $\mathbf{v}_j(t)$ be the normal of the j^{th} triangle weighted by its area. It then follows that

$$\mathbf{v}_j(t) = \frac{1}{2}\big(\mathbf{x}_{\nu(2,j)}(t) - \mathbf{x}_{\nu(1,j)}(t)\big) \times \big(\mathbf{x}_{\nu(3,j)}(t) - \mathbf{x}_{\nu(1,j)}(t)\big). \tag{4.2.8}$$

By averaging the vectors $\mathbf{v}_j(t)$ belonging to the triangles bordering $\mathbf{x}_i(t)$, we may calculate a second-order accurate normal about the center of the ray tube. We find $\mathbf{n}_i(t)$ using

$$\mathbf{n}_i(t) = \frac{\mathbf{u}_i(t)}{|\mathbf{u}_i(t)|}, \qquad \text{where} \qquad \mathbf{u}_i(t) = \sum_{k=1}^{m_i(t)} \mathbf{v}_{\mu(k,i)}(t). \tag{4.2.9}$$

The initial conditions are given by prescribing the shockfront position $\mathbf{x}_i(0)$ and Mach number $M_i(0)$ at time $t = 0$. The average point spacing Δs_{avg} and time step increment Δt are chosen following the general rules discussed in section 2.3. However, we are now approximating a shock surface as opposed to a shock curve, which implies $N \sim 1/\Delta s_{avg}^2$. This gives an increased number of points for a given Δs_{avg}. In general, we take $\Delta s_{avg} \leq .025$. In order to begin the two-step leap-frog scheme, we must calculate the shockfront at $t = \Delta t$. This is done by the use of a one-step explicit scheme.

Appropriate boundary conditions must be imposed in the numerical scheme for problems with wall boundaries. Geometrical shock dynamics assumes that rays coincide with particle paths. This implies that the shock must be normal to the wall surface. A portion of the triangulated shock surface near a wall boundary is shown in figure 4.3. The leap-frog scheme is used to propagate the interior points. The point at the boundary is determined such that the line segment between the interpolated point Q and its associated wall point P is normal to the wall at P. The point Q is given by a linear interpolation between the points $\mathbf{x}_i(t)$ and $\mathbf{x}_j(t)$.

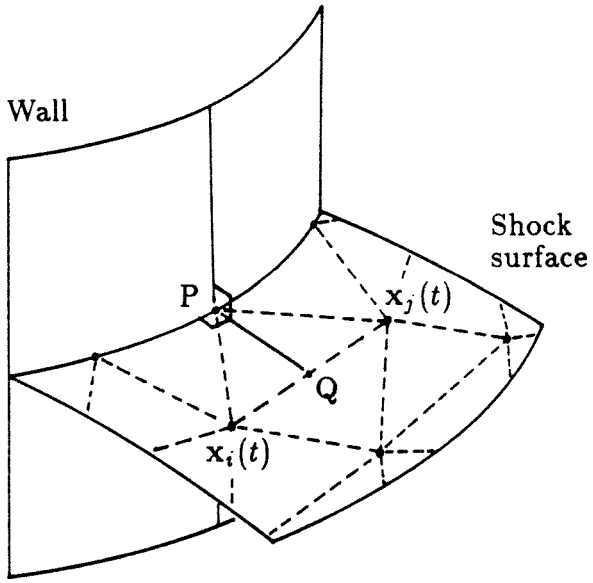

FIGURE 4.3. Numerical boundary conditions at a wall surface. Line segment PQ is normal to the wall surface at point P.

This numerical boundary condition is an extension of the boundary condition imposed in the two-dimensional scheme.

A mesh refinement scheme is performed periodically. The scheme is composed of three fundamental actions on triangle pairs. These actions are displayed in figure 4.4. We describe briefly each action before we explain the tests performed to decide which action, if any, is appropriate. If the distance between points $\mathbf{x}_i(t)$ and $\mathbf{x}_j(t)$ becomes too small, the two points may be merged into one point $\mathbf{x}'_i(t)$. The new point is given by the linear interpolation

$$\mathbf{x}'_i(t) = \frac{1}{2}\big(\mathbf{x}_i(t) + \mathbf{x}_j(t)\big). \tag{4.2.10}$$

This action (shown in figure 4.4a) is performed frequently in the vicinity of shock-shocks. The second action shown in figure 4.4b adds a point $\mathbf{x}_n(t)$ between the neighboring four points. The point $\mathbf{x}_n(t)$ is found by the bilinear interpolation

$$\mathbf{x}_n(t) = \frac{1}{4}\big(\mathbf{x}_i(t) + \mathbf{x}_j(t) + \mathbf{x}_k(t) + \mathbf{x}_l(t)\big). \tag{4.2.11}$$

The third action (shown in figure 4.4c) guards against a triangle becoming too elongated. In this case, the point connections are exchanged.

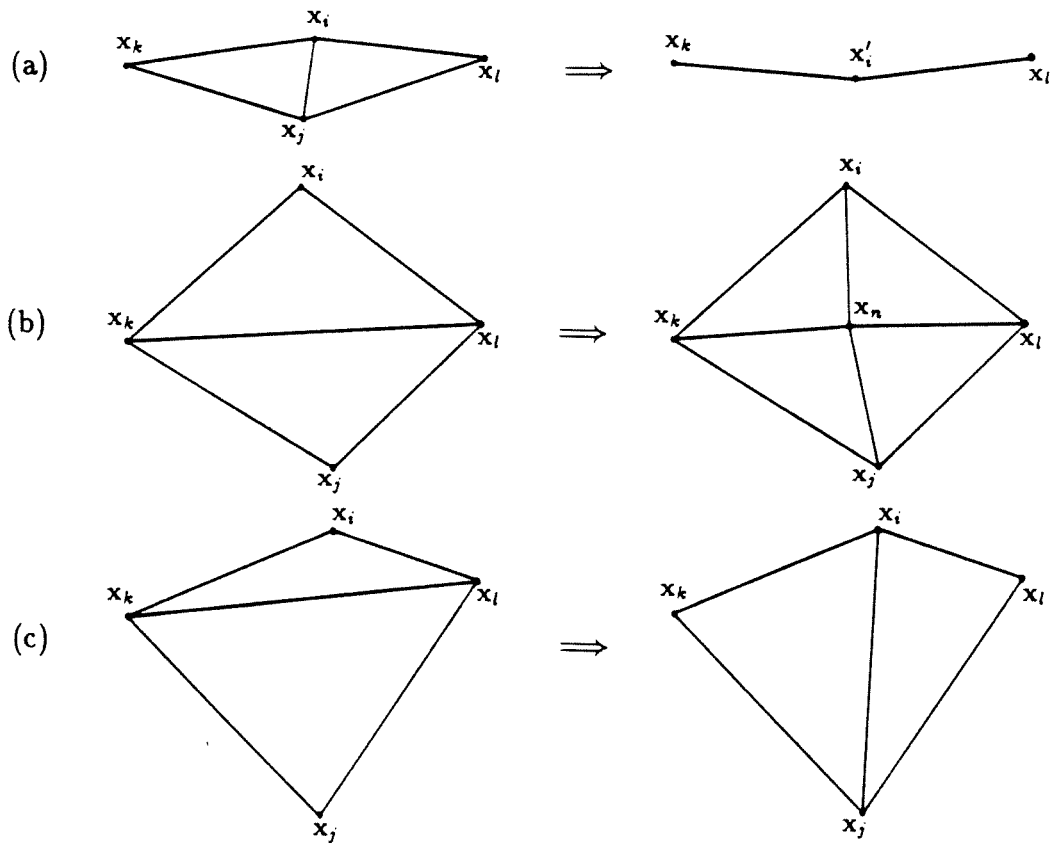

FIGURE 4.4. Mesh refinement. Three basic actions on triangle pairs: (a) merge points $\mathbf{x}_i(t)$ and $\mathbf{x}_j(t)$; (b) add point $\mathbf{x}_n(t)$; (c) exchange point connections.

The refinements displayed in figure 4.4 are performed only on interior triangles in general. Similar actions are performed on triangle pairs as well as on individual triangles near the boundary. Special care, however, must be taken for mesh refinement near the boundary in order to preserve the special mesh construction at the boundary (see figure 4.3). For example, if the distance between the points $\mathbf{x}_i(t)$ and $\mathbf{x}_j(t)$ becomes too small, the two points may be merged into one point. This action is shown in figure 4.5 where the points $\mathbf{x}_i(t)$ and $\mathbf{x}_j(t)$ are adjacent to the

boundary. As a result of the merging, the boundary point $\mathbf{x}_l(t)$ associated with the points $\mathbf{x}_i(t)$ and $\mathbf{x}_j(t)$ is removed in order to preserve the prescribed mesh construction near the boundary.

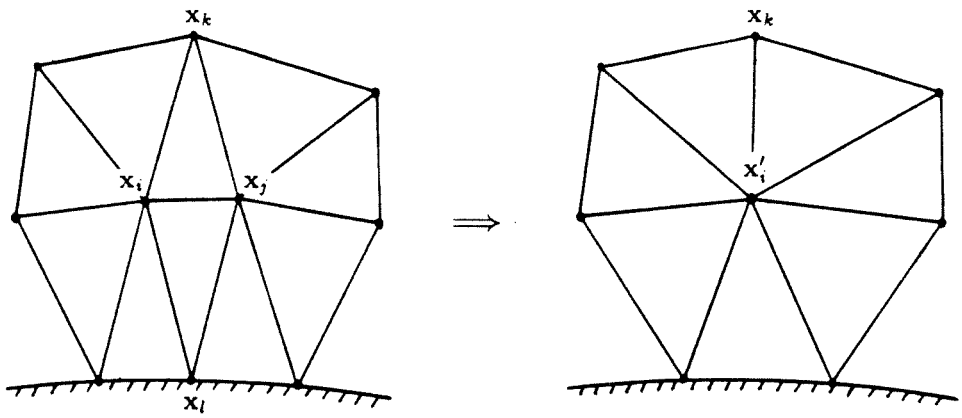

FIGURE 4.5. An example of mesh refinement near the boundary.

It remains to be decided when to perform a specific action and in what order to examine the triangle pairs. These are important aspects of the mesh refinement scheme. Unfortunately, we know of no theory that answers these questions. Thus, we rely on a combination of intuition and experience. For each triangle pair, we calculate the following relative distances:

$$\Delta s_{ij}(t) \equiv \frac{|\mathbf{x}_i(t) - \mathbf{x}_j(t)|}{\Delta s_{avg}}, \tag{4.2.12}$$

$$\Delta s_{km}(t) \equiv \frac{|\mathbf{x}_k(t) - \mathbf{x}_m(t)|}{\Delta s_{avg}}, \tag{4.2.13}$$

$$\Delta s_{lm}(t) \equiv \frac{|\mathbf{x}_l(t) - \mathbf{x}_m(t)|}{\Delta s_{avg}}, \tag{4.2.14}$$

where $\mathbf{x}_m(t) \equiv \frac{1}{2}\big(\mathbf{x}_i(t) + \mathbf{x}_j(t)\big)$. These distances are tested against a minimum allowable distance d and a maximum allowable distance D. Usually, we take $d = 1/2$ and $D = 3/2$. The following basic tests are performed on each triangle pair :

$$\Delta s_{ij} < d \quad \Longrightarrow \quad \text{merge points } \mathbf{x}_i(t) \text{ and } \mathbf{x}_j(t), \tag{T1}$$

$$\Delta s_{ij} > D \quad \text{and} \quad \Delta s_{km} > d \quad \text{and} \quad \Delta s_{lm} > d \quad \Longrightarrow \quad \text{add point } \mathbf{x}_n(t), \tag{T2}$$

$$\Delta s_{km} < d \quad \text{or} \quad \Delta s_{lm} < d \quad \Longrightarrow \quad \text{exchange point connections.} \tag{T3}$$

If none of these tests are violated, then no action is taken. One important restriction during the mesh refinement is that we impose a minimum and maximum tolerance on the number of triangles bordering the point $\mathbf{x}_i(t)$. That is, we require

$$m_{min} \leq m_i(t) \leq m_{max} \qquad \text{for all } i = 1, \ldots, N \text{ and } t, \tag{C1}$$

where we take $m_{min} = 4$ and $m_{max} = 14$, usually. Condition (C1) is easily satisfied provided the triangles remain fairly regular.

It is also important to specify the order in which actions on triangle pairs are performed. The action on a triangle pair may affect whether or not an action is taken on a neighboring pair. It is possible to examine each triangle pair, then operate on the pairs according to some measure of 'badness.' For simplicity, we operate on each triangle pair immediately after it is tested, and the order in which the pairs are tested is arbitrary.

It should be noted that the basic tests (T1), (T2) and (T3) are usually, but not always, enough to insure an approximately uniform mesh. Further tests are required, in general. For example, if points $\mathbf{x}_i(t)$ and $\mathbf{x}_j(t)$ are merged, then all of the triangles bordering the new point $\mathbf{x}_i'(t)$ are changed. After merging, it is possible that one or more of these triangles becomes degenerate or nearly degenerate (i.e., the three points at its vertices become colinear). It is also possible

that a triangle normal switches direction. These, and similar problems, are tested for before an action may be performed.

Eventually, enough of the triangles on the shock surface become irregular to the point that the numerical scheme breaks down. In all of the problems considered in section 4.3, the important features of the problems are obtained before this event occurs. This was the case for the two-dimensional scheme as well. However, in two dimensions, it was possible to propagate the shock numerically for a longer time. This fact is not surprising. A more complicated mesh refinement scheme could be developed which would allow for longer calculations. Another possibility is to retriangulate the shock surface occasionally. For the shock propagation problems considered, these improvements are not necessary.

The final element of the numerical scheme is a smoothing procedure, which is applied periodically to dampen high frequency numerical errors in the shock position. We scan the interior points on the mesh and set

$$\mathbf{x}_i(t) \leftarrow \mathbf{x}_i(t) + \left\{ \frac{1}{m_i(t)} \sum_{k=1}^{m_i(t)} \left(\mathbf{x}_{k,i}(t) - \mathbf{x}_i(t)\right) \cdot \mathbf{n}_i(t) \right\} \mathbf{n}_i(t), \tag{4.2.15}$$

where $\mathbf{n}_i(t)$ is given by (4.2.9) and the points $\mathbf{x}_{k,i}(t)$ are the $m_i(t)$ points immediately connected to the point $\mathbf{x}_i(t)$. We arrive at (4.2.15) by considering a local coordinate system (ξ, η, ς) about the point $\mathbf{x}_i(t)$, where ς is in the direction of $\mathbf{n}_i(t)$ and (ξ, η) lie in the plane whose normal is $\mathbf{n}_i(t)$. The points $\mathbf{x}_i(t)$ and $\mathbf{x}_{k,i}(t)$ are given the heights ς_i and $\varsigma_{k,i}$ in the local system. The quantity

$$\left\{ \frac{1}{m_i(t)} \sum_{k=1}^{m_i(t)} \left(\mathbf{x}_{k,i}(t) - \mathbf{x}_i(t)\right) \cdot \mathbf{n}_i(t) \right\} \tag{4.2.16}$$

in (4.2.15) is the average of heights $\varsigma_{k,i}$. We replace the height ς_i by the averaged height in order to calculate the smoothed point $\mathbf{x}_i(t)$. This procedure is similar to

the one Jacobi iteration used to smooth the shock position in the two-dimensional numerical scheme.

4.3 Some Examples

We demonstrate the use of the numerical scheme presented in section 4.2 by considering two general shock wave propagation problems in three dimensions. We first study a class of shock focusing problems similar to the two-dimensional focusing problems considered in section 2.4, part (c). In the second half of this section, we examine shock waves traveling around a bend in a circular pipe. This problem is an extension of the two-dimensional channel problems considered in section 2.4, part (b). Another motivation for studying these problems is to show some three-dimensional shock propagation effects and we discuss these as well.

(a) Shock wave focusing in three dimensions

The first problem we wish to consider is shock wave focusing in three dimensions. In each case, we calculate the focusing shockfronts using a general class of initially curved shockfront surfaces as initial conditions. At $t = 0$, we let

$$z = \frac{\sigma}{1 + (x/\alpha)^2 + (y/\beta)^2}, \tag{4.3.1}$$

where $\mathbf{x} = (x, y, z)$ and α, β and σ are constants. The Mach number is taken to be constant initially. For σ negative, the surface given by (4.3.1) obtains a minimum of $z = \sigma$ at the origin and asymptotes to a maximum of $z = 0$ as $|x| + |y| \to \infty$. We also have the principal radii of curvature for the initial shock surface at the origin given by

$$R_x = -\frac{\alpha^2}{2\,\sigma} \qquad \text{and} \qquad R_y = -\frac{\beta^2}{2\,\sigma}. \tag{4.3.2}$$

In the special case when $\alpha = \beta$, the surface given by (4.3.1) is axisymmetric about the line $x = y = 0$. We then write (4.3.1) as

$$z = \frac{\sigma}{1 + (r/\alpha)^2}, \tag{4.3.3}$$

where $r^2 = x^2 + y^2$. In this case, we have the following two independent numerical schemes availible to calculate the successive shockfronts: scheme 1, the axisymmetric version of the numerical scheme presented in section 2.3 and scheme 2, the three-dimensional numerical scheme developed in section 4.2. Scheme 1 assumes axisymmetry and calculates a slice of the shockfront surfaces along a radial line. Scheme 2 is more general and does not assume any symmetry; however, the numerical scheme should produce an axisymmetric solution given axisymmetric initial conditions and boundary conditions. We assume that scheme 1 gives accurate results based on the numerical evidence accumulated over the numerous examples considered in previous sections (in particular, section 2.4). We may then perform two tests on the shockfronts calculated using scheme 2. By comparing slices of the shockfront surfaces along various radial lines, we can check that the shockfronts calculated using scheme 2 are axisymmetric. A second test is performed by comparing a slice of the shockfronts calculated using scheme 2 with the solution obtained using scheme 1.

The successive shockfronts calculated using scheme 2 (the three-dimensional numerical scheme) are shown in figure 4.6. The initial conditions for this axisymmetric case are given by (4.3.3) with $\sigma = -.2$ and $\alpha = .2$ for x and y on the interval between $-1/2$ and $+1/2$. We assume that the initial shock is strong and we use the approximate discrete A-M relation given by (4.2.5) in the numerical scheme. There are no wall boundaries present in this calculation (or any other focusing problem in this section). The shockfront surfaces at the five time intervals shown are plotted on a rectangular mesh. This is done so that existing surface

plotting software may be used. The shock surfaces on the rectangular mesh are obtained from the shock surfaces on the triangulated mesh using a linear interpolation scheme. We stress that the actual shockfronts are calculated using the triangulated mesh described in section 4.2.

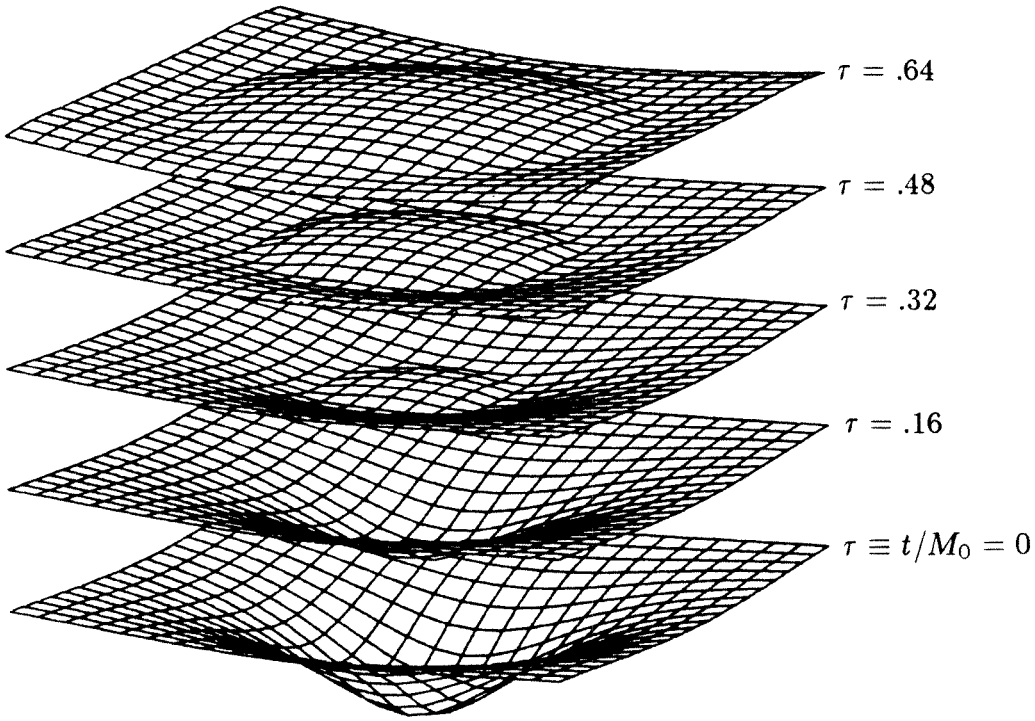

FIGURE 4.6. Focusing shock surfaces for $M_0 \gg 1$, $\sigma = -.2$ and $\alpha = \beta = .2$.

The accuracy and symmetry of the shock surfaces calculated using scheme 2 (figure 4.6) is demonstrated in figure 4.7. Two radial slices of the shockfront surfaces, one for $x > 0$ and $y = 0$ and the other for $x = 0$ and $y > 0$, are compared with the solution determined using scheme 1 (the axisymmetric numerical scheme). All three sets of curves are plotted in figure 4.7, whereas only one set is visible. The agreement between two radial slices of the shock surfaces illustrates the symmetry of the shockfronts. The further agreement between the two radial slices and the

solution provides numerical evidence that the three-dimensional scheme presented in section 4.2 calculates accurate solutions to the equations of geometrical shock dynamics.

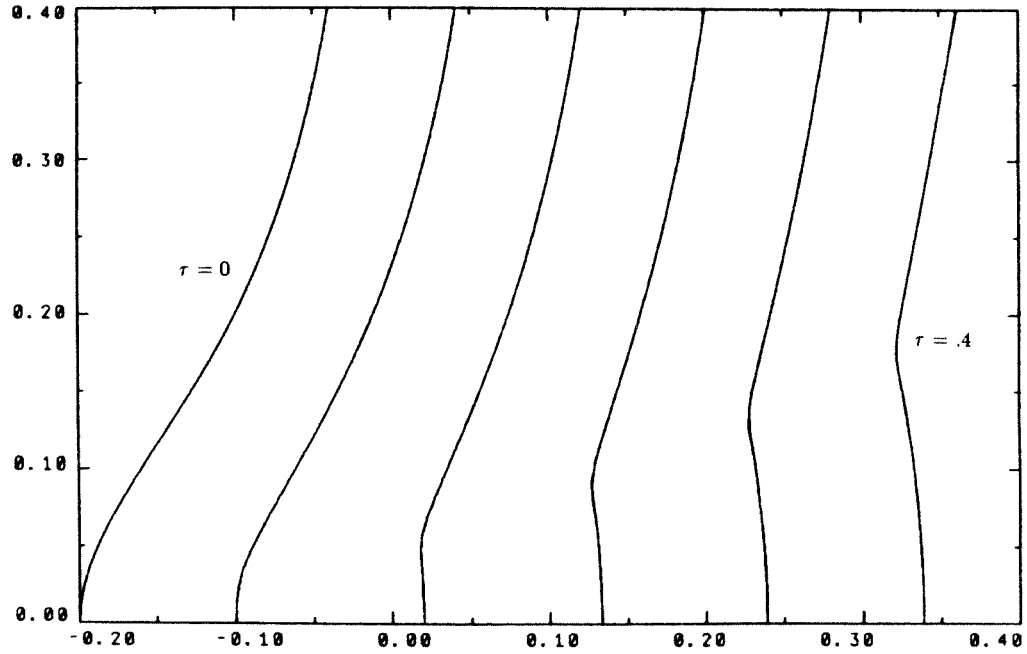

FIGURE 4.7. Two radial slices for $x > 0$, $y = 0$ and $x = 0$, $y > 0$ from scheme 2 and the solution given by scheme 1.

We found that the minimum radius of curvature of the initial shockfront and the initial Mach number determined the different focusing mechanisms observed in our previous study of shock wave focusing in two dimensions (section 2.4, part (c)). For a smaller minimum radius curvature or a weaker initial shock, a single shock-shock formed as the shockfront focused. The actual shock wave, in this case, focused to form a crossed and folded front as in geometrical acoustics. We interpreted the single shock-shock for geometrical shock dynamics as the crossing point of the actual shock. For a larger minimum radius of curvature or stronger initial shocks, two shock-shocks formed as the shock focused with a Mach stem-like shock between the shock-shocks. The latter focusing process is seen in figures 4.6

and 4.7 for the strong axisymmetric shock. These two focusing systems were studied experimentally for weak shocks by Sturtevant & Kulkarny [1976]. In part (c) of section 2.4, we found that the shockfronts calculated using geometrical shock dynamics showed good agreement with the experimental results.

In three dimensions, we have an additional basic parameter that affects the focusing process. This additional parameter is the ratio of principal radii of curvature R_x/R_y, where we let R_y denote the minimum radius of curvature of the initial shock surface. For our particular shock surface given by (4.3.1), $R_x/R_y = (\alpha/\beta)^2$. We have already considered the two limiting cases. As $R_x/R_y \to \infty$, we recover the two-dimensional case and for $R_x/R_y = 1$, we have the axisymmetric case. We now wish to investigate the focusing process for R_x/R_y between the two limits.

We use the initial shock surface given by (4.3.1) with $\alpha \neq \beta$ to gain some feeling for how the focusing process is affected by R_x/R_y between 1 and ∞. Figure 4.8 shows a surface plot of the focusing shockfronts for $\sigma = -.25$, $\alpha = .30$ and $\beta = .15$. This choice of constants gives $R_x/R_y = 4$. We also show slices of the shockfront surfaces in the orthogonal planes $x = 0$ and $y = 0$ in figure 4.9. For this particular case, we assume that the initial shock is strong ($M_0 \gg 1$). In the plane $x = 0$ (figure 4.9a), we see that two shock-shocks form as the shockfronts focus. The Mach stem between the shock-shocks grows and becomes convex forward as the shockfront travels downstream. This focusing process is commonly observed for strong shock focusing in two dimensions (see, for example, figure 2.21d in section 2.4). In fact, the focusing appears to be two-dimensional in the plane $x = 0$, where the initial shock curve attains the minimum radius of curvature. In the orthogonal plane $y = 0$ (figure 4.9b), the shockfront bulges forward at an earlier time than it would for two-dimensional focusing. This focusing process is easily explained. As the initial shockfront propagates, the center portion of the surface

compresses. Since the radius of curvature in the $x = 0$ plane is smaller, the compression is strongest in this plane. This produces focusing in the $x = 0$ plane first. As a result of the focusing in the $x = 0$ plane, the compression on the shock surface in the $y = 0$ plane is reduced, and thus the focusing in the $y = 0$ plane is reduced.

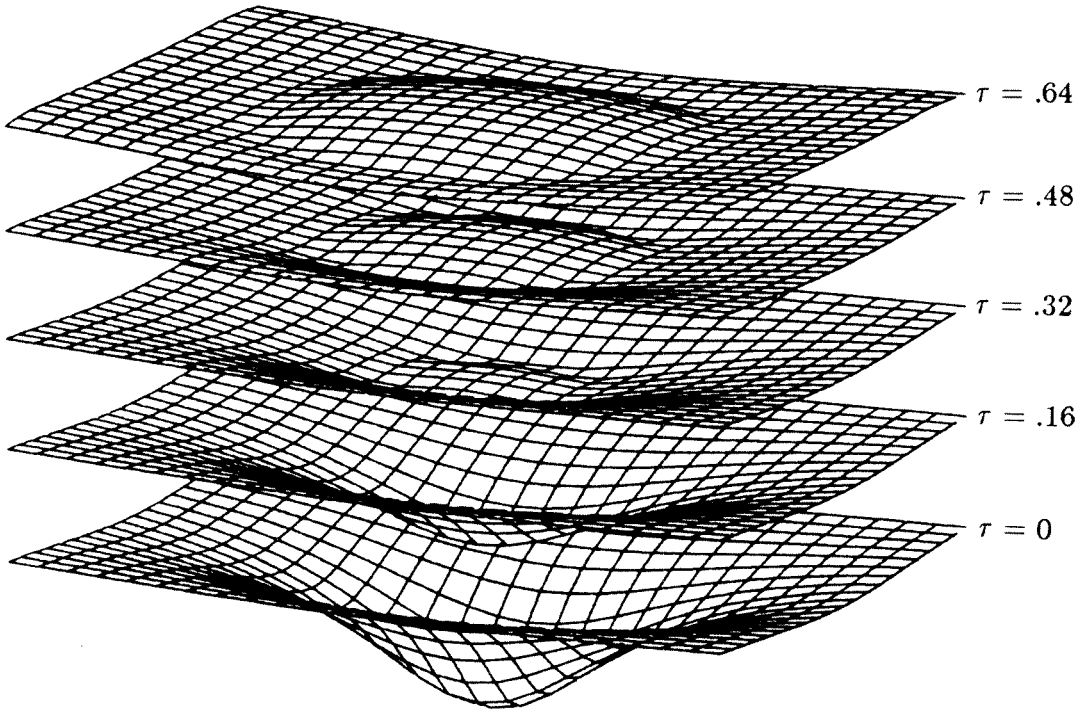

FIGURE 4.8. Focusing shock surfaces for $M_0 \gg 1$, $\sigma = -.25$, $\alpha = .3$ and $\beta = .15$.

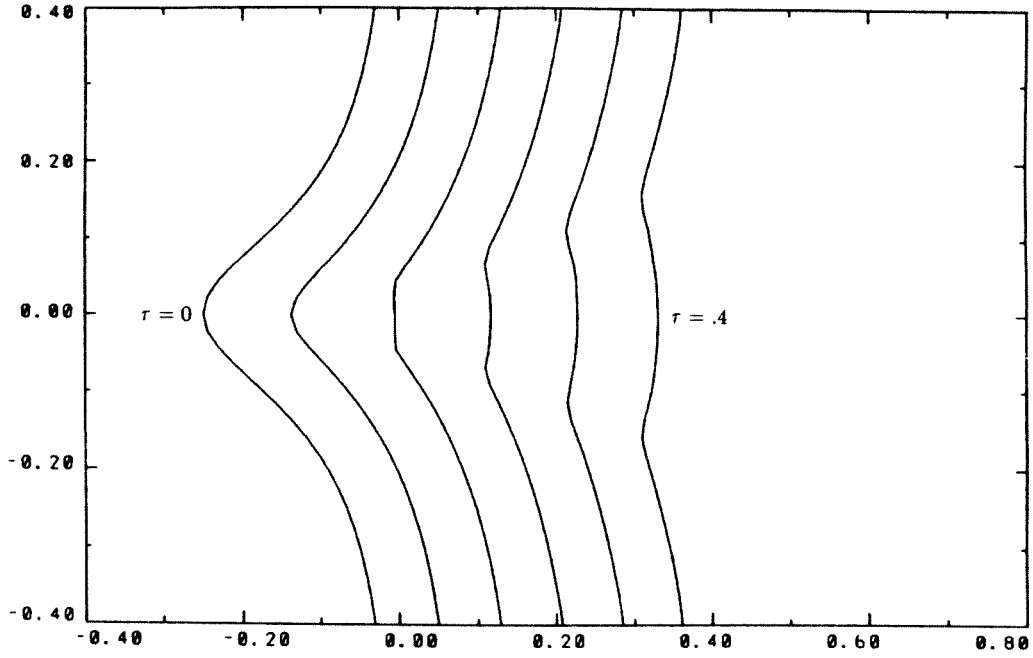

(a) Plane $x = 0$

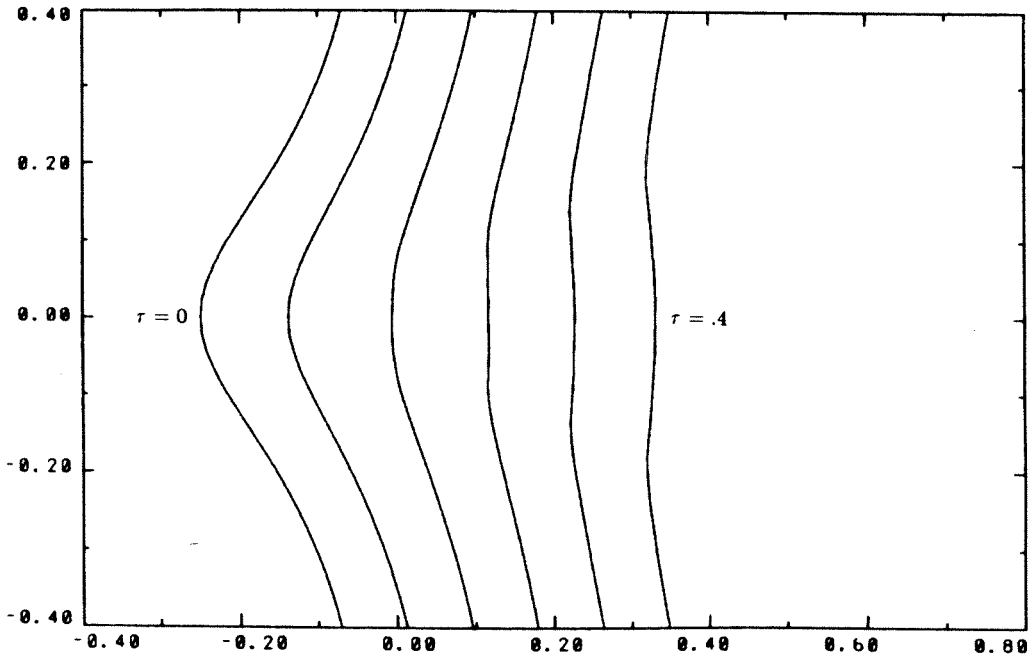

(b) Plane $y = 0$

FIGURE 4.9. Planar slices from surfaces given in figure 4.8.

We also studied the focusing of weak shocks in three dimensions. A typical example from this study is shown in figure 4.10. Again, we plot slices of the shockfront surfaces in the planes $x = 0$ and $y = 0$. For this case, $M_0 = 1.03$ and we use the approximate A-M relation for weak shocks given by (4.2.4). In the plane $x = 0$, a single shock-shock forms, indicating the actual shock wave has formed a crossed and folded pattern. This is a typical focusing pattern observed for weak shock focusing in two dimensions. As before, we do not see any focusing in the $y = 0$ plane as a result of the focusing process in the $x = 0$ plane.

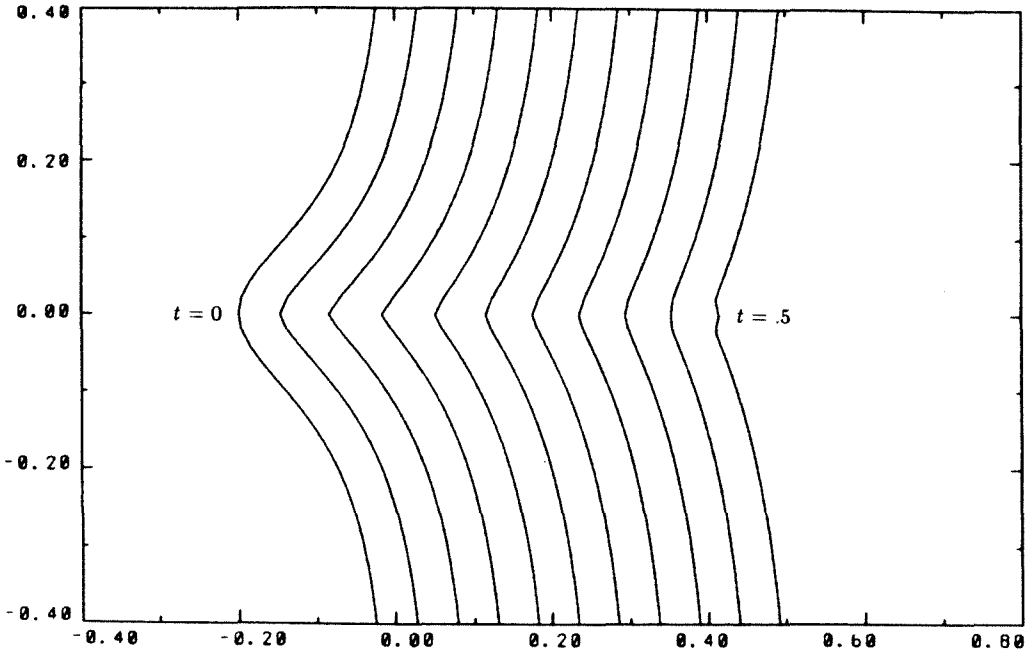

(a) Plane $x = 0$

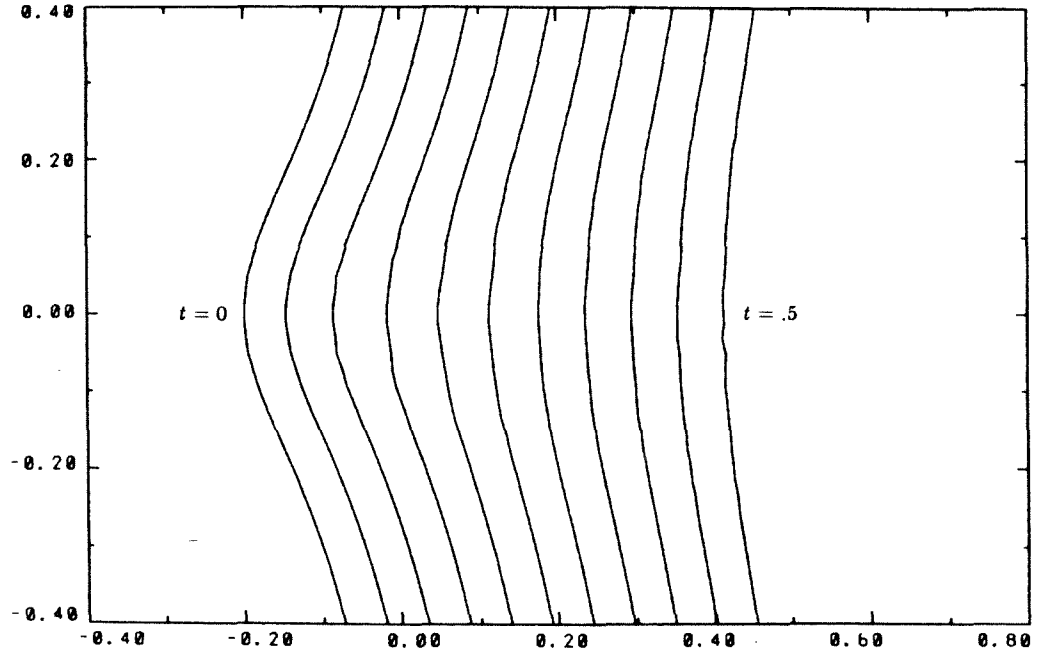

(b) Plane $y = 0$

FIGURE 4.10. Planar slices for weak shock focusing, $M_0 = 1.03$.

(b) Shock wave propagation in a curved pipe

The second problem we wish to consider is shock wave propagation around a 90° bend in a pipe with circular cross section. The geometry of the problem is shown in figure 4.11. We denote the radius of the circular bend by R. The radius of circular cross section of the pipe is r. For the particular pipe used in this study, we have $R/r = 3$. The initial shock is planar and we take $M_0 \gg 1$. Our primary reason for studying this problem is to illustrate the numerical treatment of the walls, which is an added feature of the numerical scheme not used in the focusing problem. We are also motivated in studying this problem as an extension of the two-dimensional channel problem discussed in section 2.4, part (b). The diffraction of the shockfronts in the three-dimensional pipe is more complicated and shows features not present in the channel problem. However, we find the channel results useful in interpreting the results obtained for the three-dimensional pipe. In particular, the analogous channel geometry is given by channel 1, where $R/r \approx 3$.

Slices of the shockfront surfaces in three different parallel planes are displayed in figure 4.12. We see that the successive shockfronts in the plane $x = 0$ (figure 4.12a) are qualitatively similar to the shockfronts produced in channel 1 (figure 2.12, section 2.4). The shockfront expands around the inner wall. The shockfront compresses and forms a shock-shock near the outer wall. When the expansion from the inner wall meets the shock-shock near the outer wall, the shock-shock is weakened and turned towards the inner wall. The shock-shock continues until it meets the inner wall at $t/M_0 \equiv \tau = 3.2$. (The initial Mach number enters the problem only as a scaling of time for strong shocks.) We show slices of the shockfronts away from the centerplane of the pipe in figures 4.12b and 4.12c. These two plots give an indication of the extent of the shock-shock curve in the x-direction. In the plane $x = r/2$, a clear shock-shock does not form until the

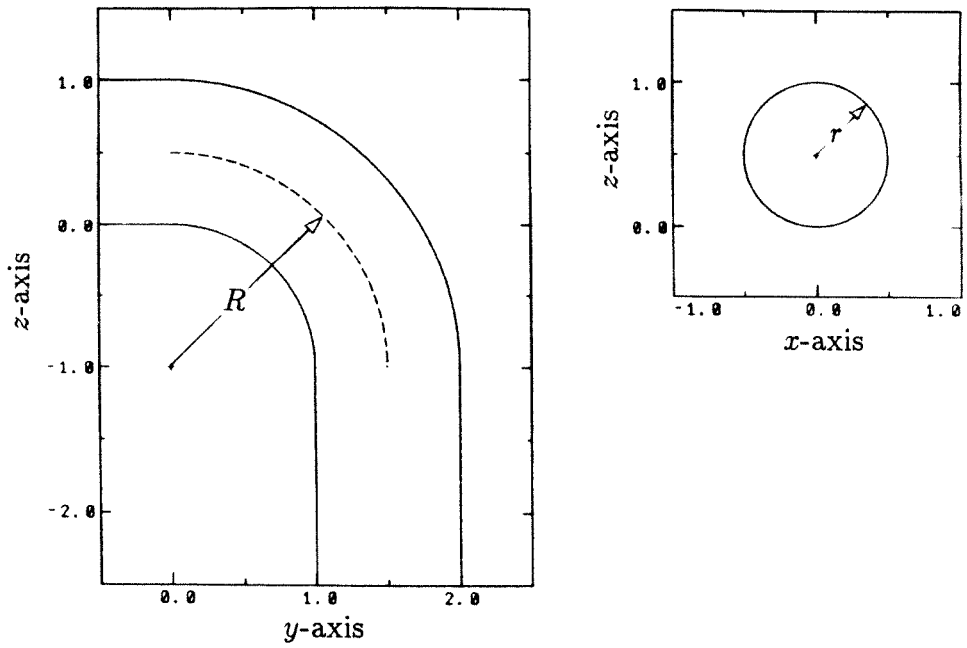

FIGURE 4.11. Curved pipe geometry, $R = 1.5$ and $r = .5$

shockfront is nearly around the bend. The shock-shock in the plane $x = 3r/4$ is not seen until the shockfront is in the straight portion of the pipe after the bend.

Further information on the diffracting shockfronts is gained via the sequence of surface plots provided in figure 4.13. The shock surfaces for $\tau = 1.2$, 1.8, 2.4 and 3.0 are shown in figure 4.13a. Enlargements of these shock surfaces are shown in figures 4.13b–c. Each plot shows one-half of the shock surface and the inside of the pipe for $x \leq 0$. We plot the shock surface using a polar mesh as opposed to using the actual triangulated mesh for ease in plotting (as discussed before). The view is looking down at the surfaces from a point located at $\mathbf{x}_{view} \approx (25, 0, 10)$. The curved boundary of each shockfront surface is on the inside wall of the pipe and the straight boundary is in the centerplane $x = 0$. In order to visualize these plots, we found the shockfronts in the plane $x = 0$ (figure 4.12a) helpful as a reference. The surface plots clearly show the diffraction of the shockfronts by the curved

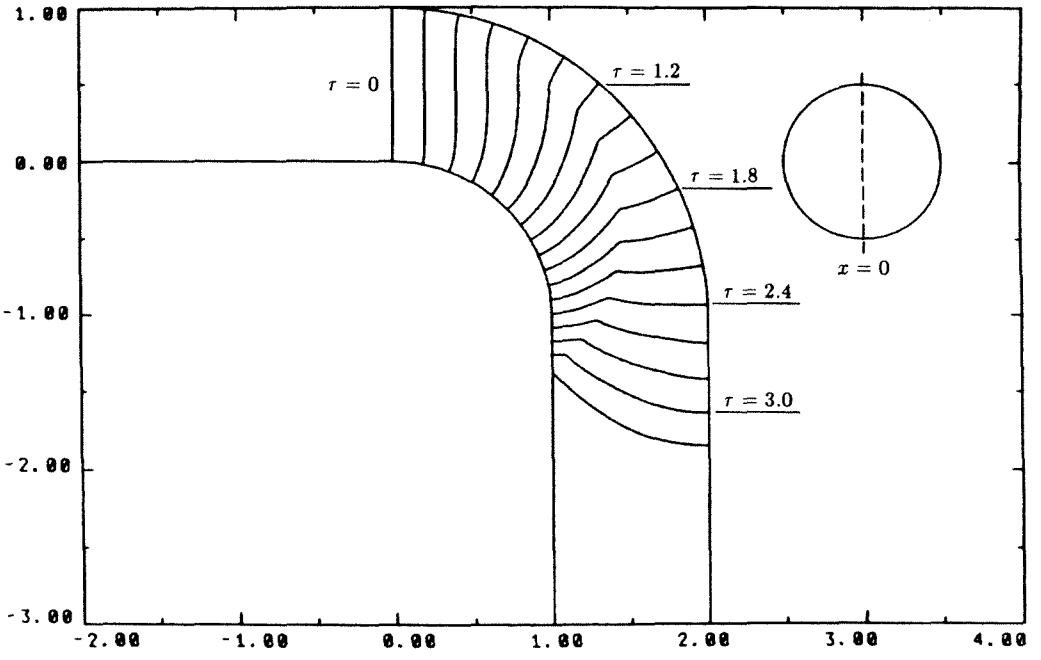

(a)

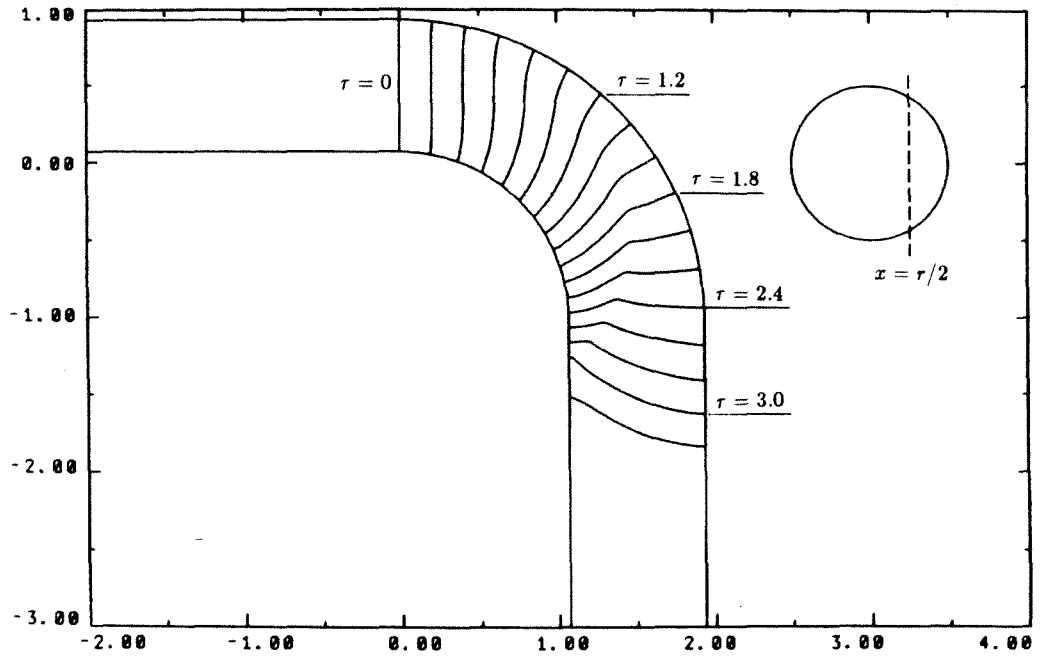

(b)

FIGURE 4.12. Shock wave diffraction in a curved pipe for $M_0 \gg 1$.

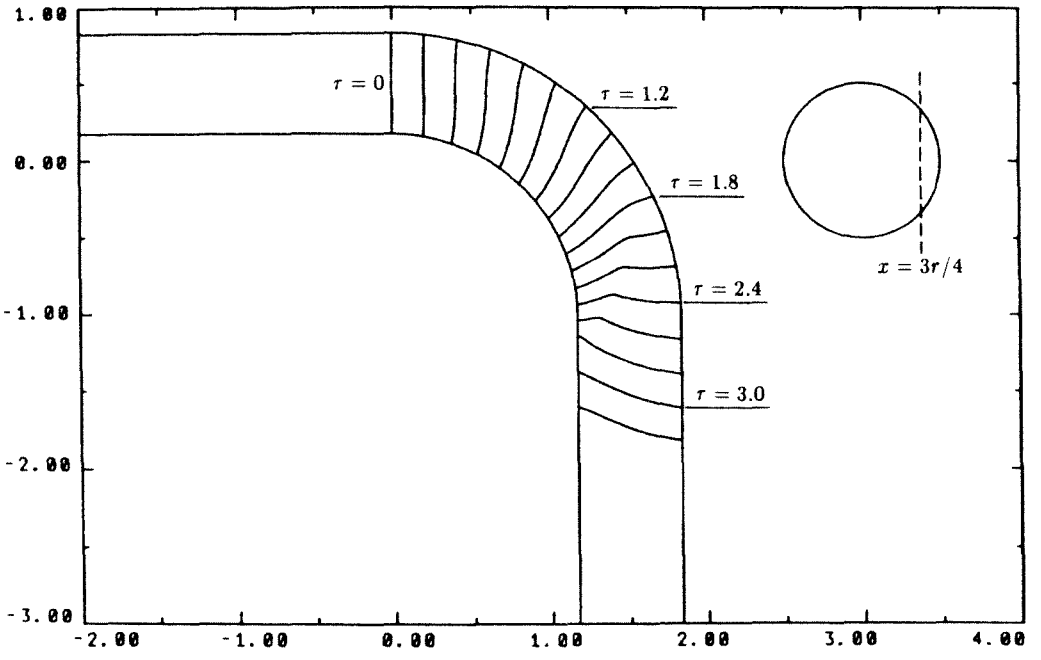

(c)

FIGURE 4.12. (cont.). Shock wave diffraction in a curved pipe for $M_0 \gg 1$.

pipe. We see the formation of a shock-shock curve at $\tau = 1.2$ (figure 4.13b). As the shockfront propagates, the shock-shock curve appears to be diffracted as well by the curved pipe wall. This diffraction occurs as the shock-shock moves along the curved pipe wall on the shock surface. The shock-shock near the wall is weak at first. By $\tau = 3.0$ (figure 4.13c), the shock-shock near the wall is much stronger (i.e., the 'kink' in the shock surface is more severe). The strengthening of the shock-shock curve by the wall is analogous to the strengthening of the shockfront by a single concave wall in two dimensions discussed in section 2.4, part (a). The motion of the shock-shock curve is an interesting feature of shock diffraction in three dimensions, which is not observed in the two-dimensional channel problems.

We also calculate the Mach number at various postions along the wall. We display these results in figure 4.14. The three plots of M_w/M_0 versus distance along

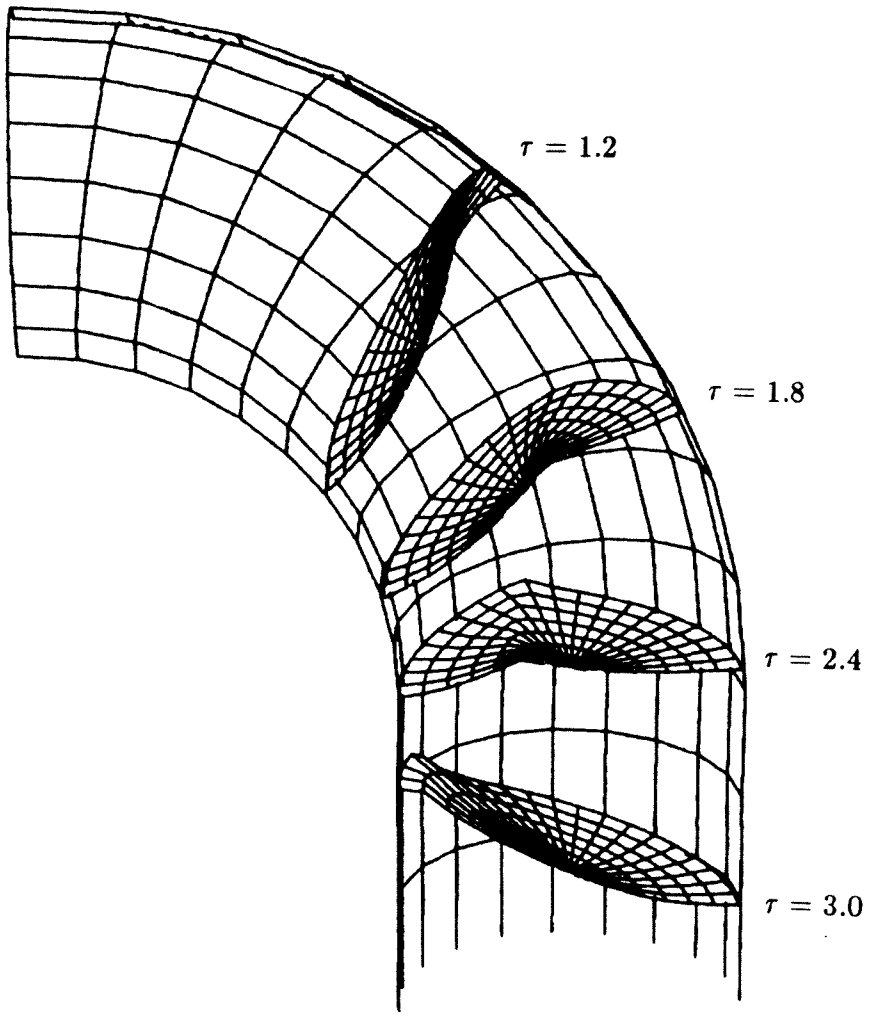

(a)

FIGURE 4.13. Shock wave diffraction in a curved pipe for $M_0 \gg 1$. View position is $\mathbf{x}_{view} \approx (25, 0, 10)$.

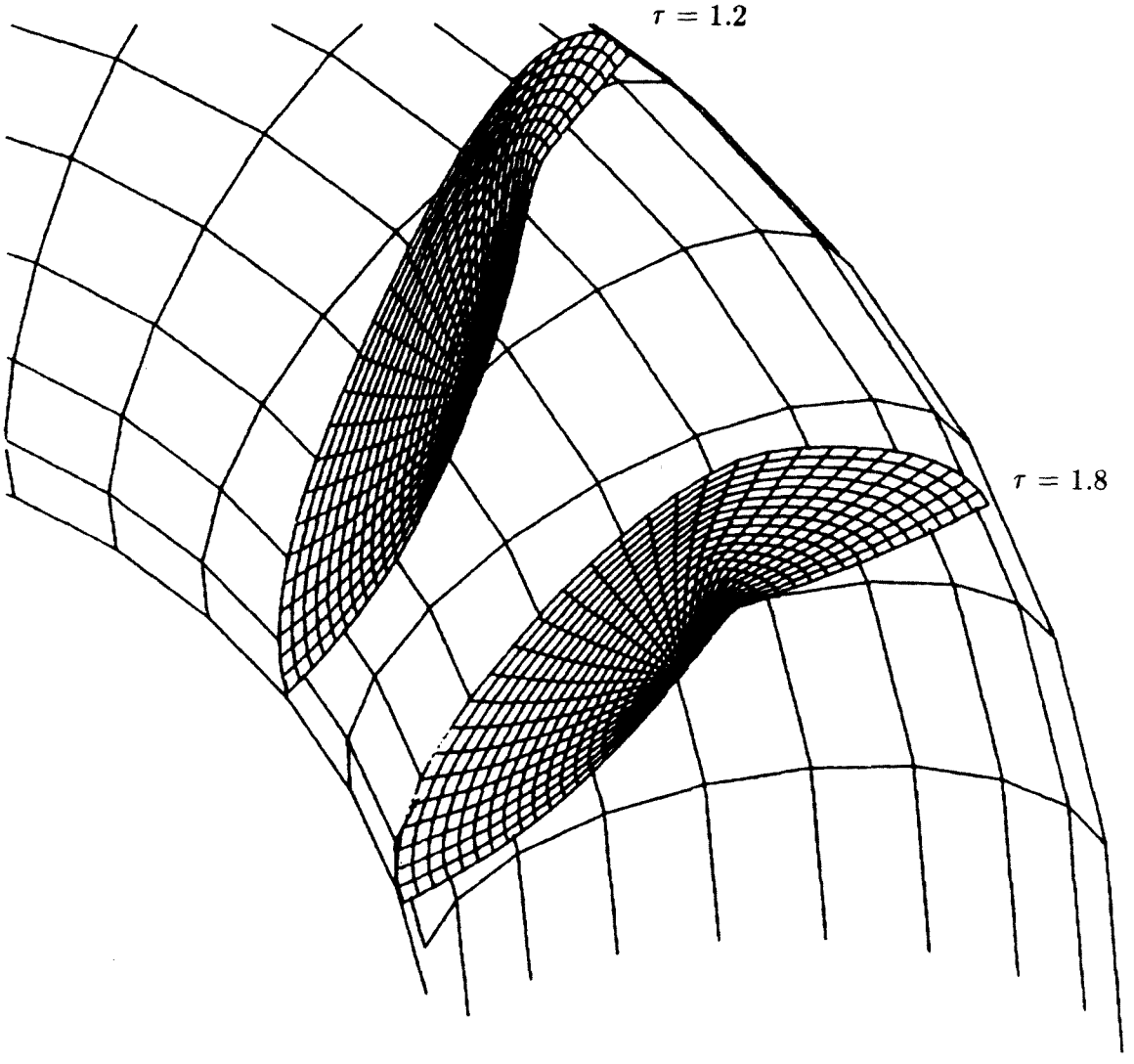

(b)

FIGURE 4.13. (cont.). Shock wave diffraction in a curved pipe for $M_0 \gg 1$. View position is $\mathbf{x}_{view} \approx (25, 0, 10)$.

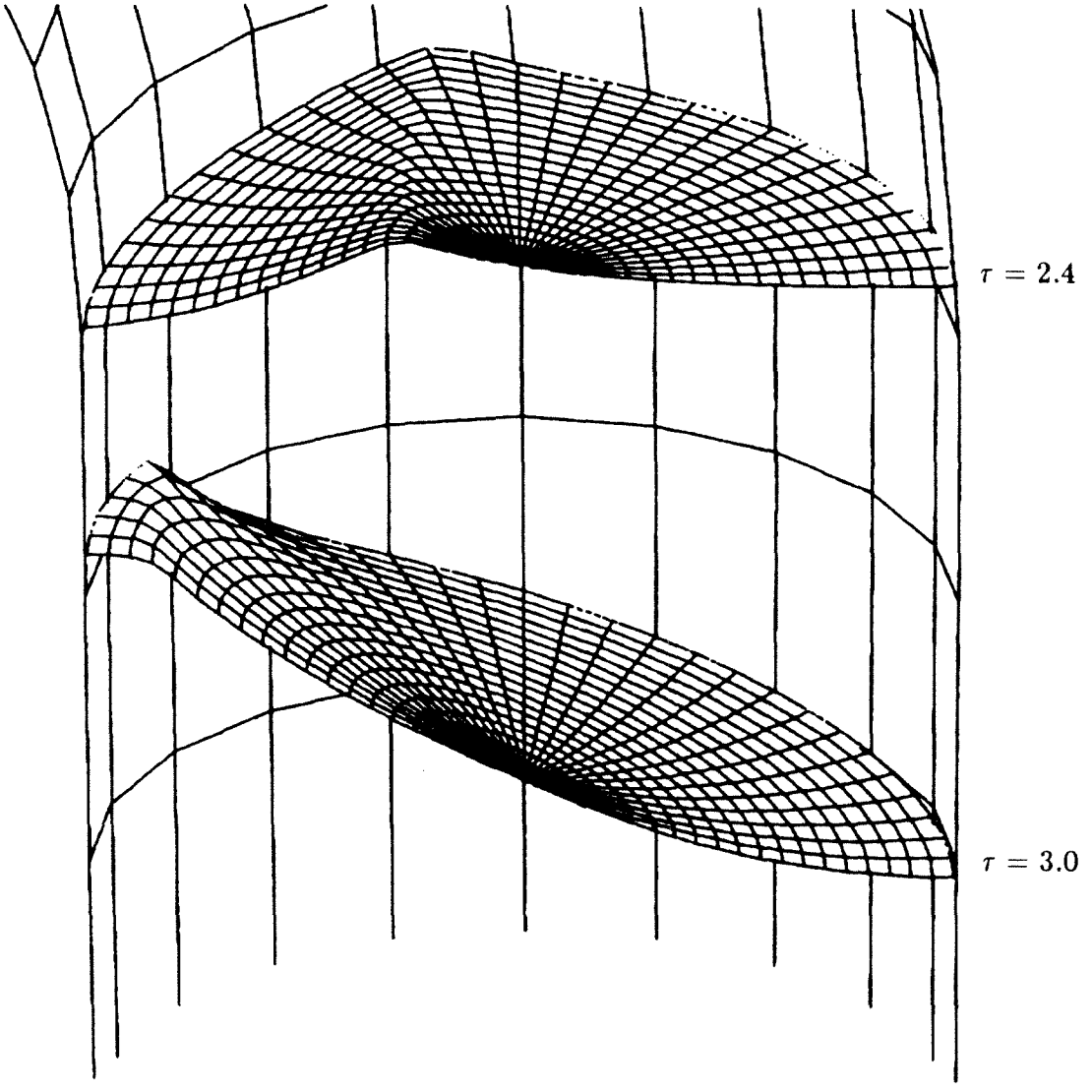

(c)

FIGURE 4.13. (cont.). Shock wave diffraction in a curved pipe for $M_0 \gg 1$. View position is $\mathbf{x}_{view} \approx (25, 0, 10)$.

the wall in figures 4.14a–c correspond to the shockfront plots in figures 4.12a–c for the planes $x = 0$, $x = r/2$ and $x = 3r/4$, respectively. In each wall Mach number plot, there are two curves. The curve for which $M_w/M_0 \geq 1$ is given by the Mach numbers on the outer wall and the the other curve is given by the Mach numbers on the inner wall. The Mach number along the outer wall increases initially before decreasing eventually in each plot. On the centerplane, M_w increases to $1.45\,M_0$ before decreasing. This is a slightly larger value than $1.40\,M_0$ given for channel 1 (see figure 2.14 in section 2.4). For the planes $x = r/2$ and $x = 3r/4$, M_w increases to $1.35\,M_0$ and $1.2\,M_0$, respectively. The Mach number on the inner wall decreases initially, then increases sharply at the position where the shock-shock meets the inner wall. The same qualitative results were obtained for the channel. For the pipe, however, the Mach number on the inner wall decreases to nearly $0.4\,M_0$, which is significantly lower than $0.6\,M_0$ found for channel 1. This lower value for the pipe implies that the shock-shock reflection at the inner wall is more severe than that observed for channel 1.

An important advantage of the triangulated mesh used for the three-dimensional calculations is its ability to handle a variety of shock geometries. The focusing problems are calculated in a rectangular domain. For the pipe problem, we require a mesh on a circular domain. The triangulated mesh is easily used in both of these cases. These two examples indicate the generality of the triangulated mesh.

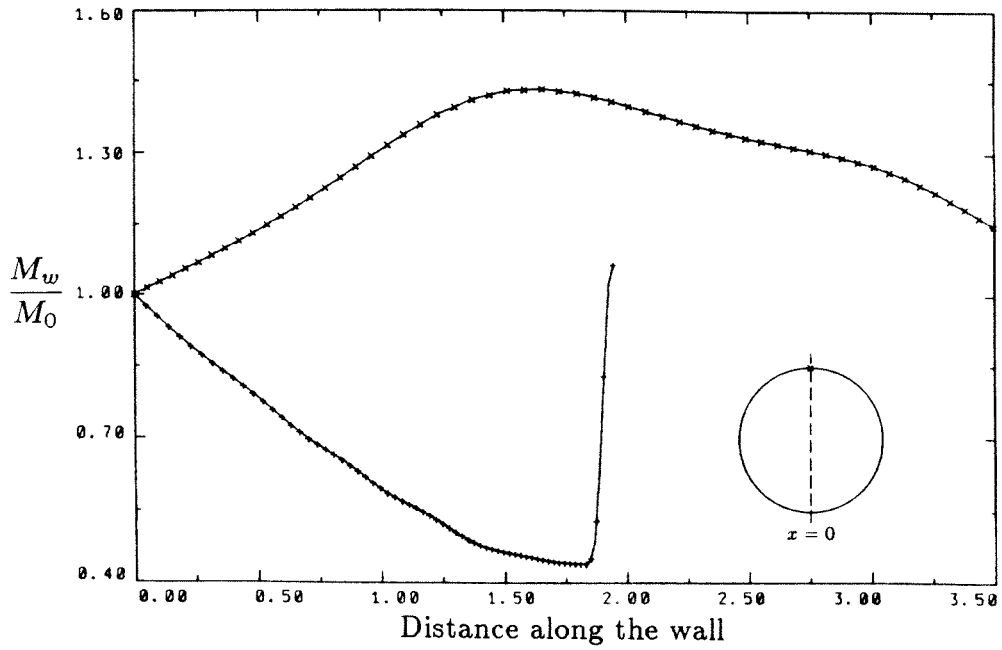

(a)

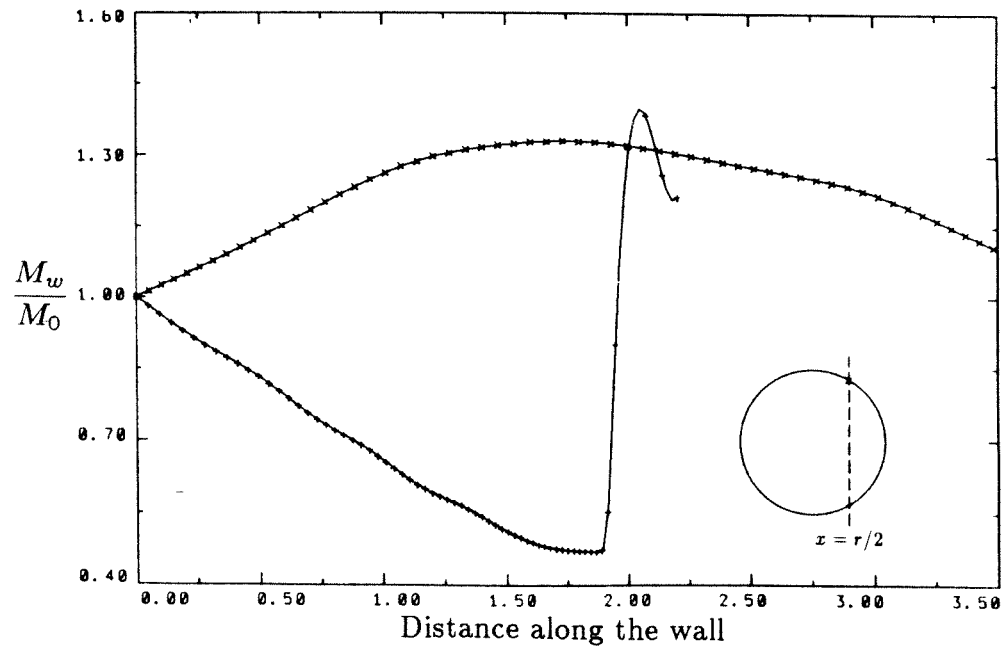

(b)

FIGURE 4.14. M_w/M_0 versus distance along the pipe wall.

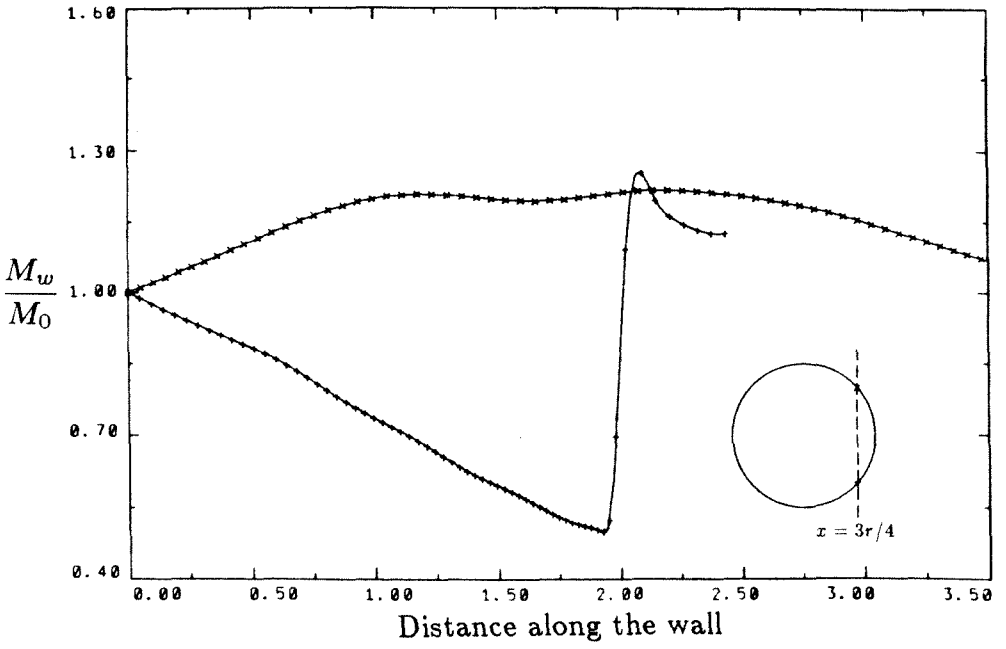

(c)

FIGURE 4.14. (cont.). M_w/M_0 versus distance along the pipe wall.

CHAPTER 5

Reflection of a Planar Shock Wave

5.1 Introduction

In Chapter 2, we considered some preliminary results for the two-dimensional focusing of shock waves as determined by geometrical shock dynamics. By comparing with the actual focusing shock waves found experimentally for weak shocks, we established that geometrical shock dynamics gives a good qualitative description of the focusing process. On the other hand, a comparison of quantitative measurements of the Mach number (and thus the pressure jump) of the focusing shockfront on the axis of symmetry showed some discrepancy with the experimental results of Sturtevant & Kulkarny [1976]. In our previous work on shock focusing (section 2.4, part (c)), it was not clear whether the chief source of error was the approximate theory (geometrcial shock dynamics) or the approximate initial conditions used in the calculations. If we can improve the initial conditions required for the calculations, we can better assess the accuracy of the approximate theory for the focusing of weak shocks.

In the experiments of Sturtevant & Kulkarny, curved shockfronts, which later focus, are produced by reflecting planar incident shocks from some curved wall. In order to calculate the subsequent motion of the reflected shock wave using geometrical shock dynamics, we require some initial approximation for the shockfront *after* it reflects from the curved wall. The accuracy of this initial approximation is important since our numerical experiments show that quantitative measurements

near the focus (for example, the Mach number on the axis of symmetry) are sensitive to the initial shockfront used in the calculations. Thus, to gain a better feeling for how well geometrical shock dynamics predicts the focusing of weak shocks, it would be useful to develop a method of determining the reflected shockfront for a given reflector geometry and incident shock strength.

The accuracy of geometrical shock dynamics for the motion of *weak* shock waves is useful to document since there was some indication that the approximation is not at its best for $M < 2$. The focusing mechanisms for weak shocks are particularly complicated and consequently a challenge for any simple approximate theory. Accordingly, any deficiencies found in this application would not necessarily be the case for stronger shocks. In fact, we find that geometrical shock dynamics performs surprisingly well for weak shocks.

In this chapter, we describe how the initial reflection at the reflector surface can be incorporated into the theory of geometrical shock dynamics to improve the focusing calculations of section 2.4. It is necessary for the method developed here to assume that the shock wave approaching the reflector is planar. Thus, the motion of the gas behind the incident shock is known to travel with a constant velocity given by the normal shock relations. The reflected shock wave is determined using geometrical shock dynamics in a reference frame moving with the gas behind the incident shock. This is a convenient frame of reference since the gas ahead of the reflected shock is at rest. The boundary conditions for the reflected shockfront at the reflector surface are given by the usual theory of regular reflection, which specifies the Mach number and ray inclination angle of the reflected shock in terms of the Mach number of the incident shock and the slope of the wall. These reflection conditions are embedded in the theory of geometrical shock dynamics by considering a modified A-M relation similar to that discussed for shock-shocks in

section 2.2. We supply the necessary results from regular reflection and discuss the details of its application in section 5.2.

Only minor modifications in the basic numerical scheme of section 2.3 are required to calculate the motion of the shockfront. These changes and additions to the scheme are discussed is section 5.3. In general, we propagate the points belonging to the incident shock and points belonging to the reflected shock independently using the basic leap-frog time marching scheme. The discrete version of the modified A-M relation is used to determine the speed of the shockfront. As points on the incident shock meet the wall, the points are transferred to the reflected shock using reflection conditions given by regular reflection.

It is interesting to compare the previous approximate reflected shockfront used as initial conditions for shock wave focusing (section 2.4) with the reflected shockfront calculated using the method of section 5.3. For weak incident shock waves, the reflected shockfront shape given by geometrical acoustics is an obvious first approximation to the actual reflected shockfront. This was the basic shape used in section 2.4, part (c) to study the focusing of shock waves reflected by a parabolic reflector. The reflected shock wave is known to have a variable shock strength. However, a constant shock strength was used in the previous calculations for simplicity. The reflected shockfront calculated using the improved method of section 5.3 shows significant deviation in both the shockfront geometry and strength from the approximations of section 2.4. We discuss these differences in detail in section 5.4.

Finally, we calculate successive shockfronts for the case of a planar incident shock wave reflected by a parabolic reflector and again compare with experimental data. The improved method described in section 5.2 is found to give more accurate qualitative and quantitative results.

5.2 Combined Theory

We consider the problem of a planar incident shock reflected by a curved reflector. The conditions given by regular reflection at a planar wall may be used locally at the curved reflector surface to determine boundary conditions for the reflected shockfront. The motion of the shock away from the reflection point is basically given by the approximate theory of geometrical shock dynamics as originally described by Whitham [1957] and presented in section 2.2. We refer to the diagram in figure 5.1 for the components of the problem considered. The incident shock $\mathbf{S}_I$ travels with constant Mach number M_I in the lab frame of reference. The gas behind $\mathbf{S}_I$ is uniform and moves with constant Mach number M_1 given by the normal shock relation

$$M_1 = \frac{2}{\gamma+1}\frac{M_I^2-1}{M_I}. \tag{5.2.1}$$

The incident shock is reflected by the curved reflector at the point P. The reflected shock $\mathbf{S}_R$ propagates with a Mach number M_R back into the uniform gas entrained by the incident shock. The position of the reflector surface is known and given by the equation, $x = x_w(y)$.

The shock system in the vicinity of the reflection point is shown in figure 5.2. We approximate the curved reflector locally by the planar wall $\mathbf{W}$ with slope given by dx_w/dy. The angle ω_I is then given by

$$\omega_I = \tan^{-1}\left(\frac{dx_w}{dy}\right). \tag{5.2.2}$$

In figure 5.2a, the point P moves down the wall with Mach number $M_I \cot\omega_I$. The equivalent shock system for which P is at rest is shown in figure 5.2b. The normal shock relations are applied across the incident and reflected shocks. The kinematic condition that the normal component of the velocity (or Mach number)

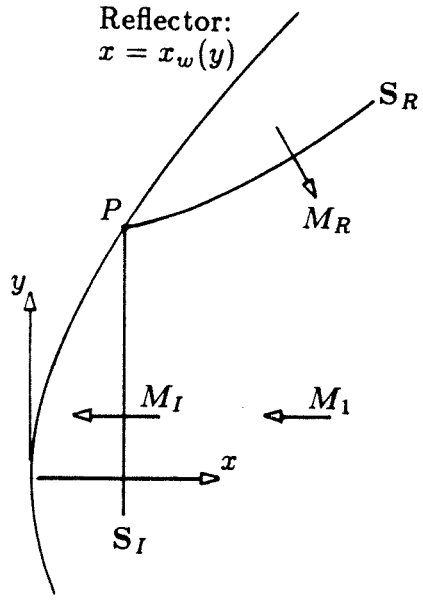

FIGURE 5.1. Reflector geometry.

in region 3 must vanish provides a functional relationship between M_I, ω_I and ω_R of the form

$$F(M_I, \omega_I, \omega_R) = 0. \tag{5.2.3}$$

The function F in (5.2.3) is known and determines the reflection angle ω_R implicitly in terms of the incident Mach number and the wall slope. The solution ω_R to (5.2.3) for various M_I and ω_I is well established (see Emmons [1958], for example). For M_I near one (a weak incident shock), a solution to (5.2.3) always exists for the range of ω_I used in the calculations (roughly ω_I between 0° and 40°). The condition that the incident and reflected shock remain attached at the point P gives

$$M_R = M_I \frac{\sin \omega_R}{\sin \omega_I}, \tag{5.2.4}$$

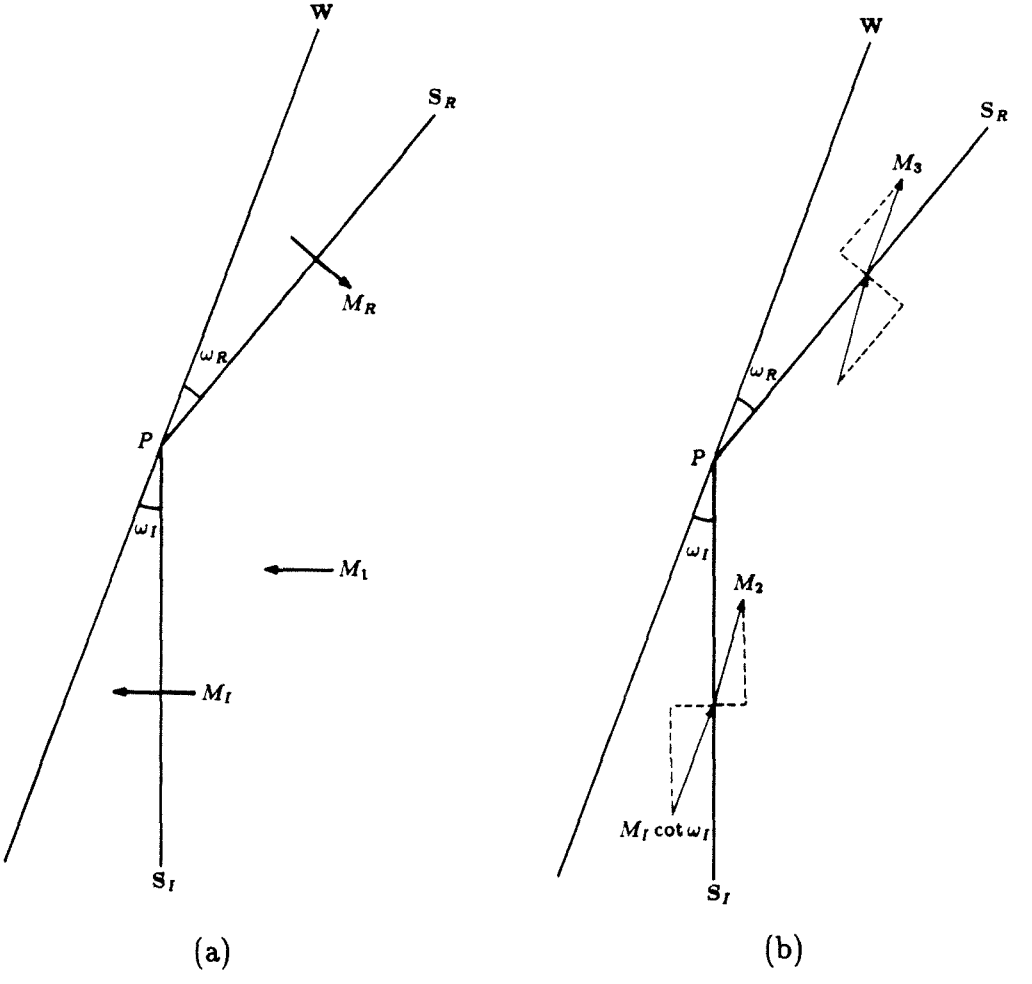

FIGURE 5.2. Regular reflection: (a) lab frame; (b) point P is at rest.

where M_R is the Mach number of the reflected shock.

We now describe how the conditions at the reflector surface given by regular reflection may be incorporated into the approximate theory of geometrical shock dynamics. Let us consider a small portion of the shockfront moving towards the the reflector surface in a reference frame moving with gas behind the incident shock as shown in figure 5.3. The area of the incident shock is A_I and it travels with constant Mach number $M_I - M_1$. The wall is moving towards the incident shock with constant Mach number M_1. The ray tube area after reflection is given by A_R

and the Mach number of the reflected shock is M_R. We assume that ω_R and M_R are given in terms of ω_I and M_I by the regular reflection conditions (5.2.3) and (5.2.4).

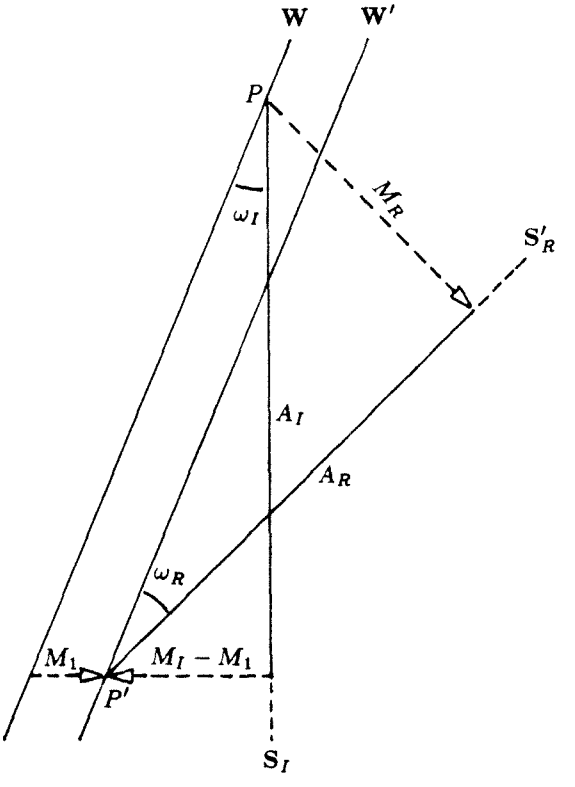

FIGURE 5.3. Area adjustment given by regular reflection.

The A-M relation presented in section 2.2 is modified to account for the reflection conditions at the reflector surface. The new relation is

$$\frac{A}{A_I} = k(\beta)\frac{f(M)}{f(M_0)}, \tag{5.2.5}$$

where $M_0 = M_I - M_1$ and $f(M)$ is given by (2.2.2). The modified A-M relation (5.2.5) varies along the shockfront through the function $k(\beta)$, where $k(\beta) = 1$ for the motion of $\mathbf{S}_I$ and

$$k(\beta) = \frac{A_R}{A_I}\frac{f(M_0)}{f(M_R)} \tag{5.2.6}$$

for the motion of $\mathbf{S}_R$. The coordinate β refers to the particular ray. The area ratio in (5.2.6) is found from the geometry in figure 5.3 and is given by

$$\frac{A_R}{A_I} = \frac{(M_R - M_1 \cos\omega_I \sec\omega_R)\cot\omega_R}{M_I \cot\omega_I}. \tag{5.2.7}$$

The new A-M relation in (5.2.5) is the only modification to the theory of geometrical shock dynamics needed to describe the motion of the shockfront. The propagation of the shockfront prior to reflection is known trivially. The point of reflection and the value of $k(\beta)$ for all points on the shockfront may also be found prior to reflection. These facts are simplifications that rely on the assumption that the incident shock is planar and travels with constant Mach number. After reflection, we use the new A-M relation along with the kinematic relations (2.2.12) to propagate the shock.

5.3 Numerical Scheme

We calculate the successive shockfronts using a numerical scheme which is a modification of the basic numerical scheme presented in section 2.3. Away from the reflector surface, we numerically propagate the shock as before except that the discrete version of the modified A-M relation (5.2.5) is used to determine the local Mach number of the shockfront. Near the reflector, we apply the conditions given by regular reflection numerically to determine the shock position. In this section, we will describe only the new aspects of the numerical scheme; a detailed description of the basic numerical scheme may be found in section 2.3.

We approximate the shockfront by a discrete set of points $\mathbf{x}_j(t)$, $j = 1, \ldots, N$, where $\mathbf{x} = (x, y)$. Let $J_I(t)$ be the set of all points belonging to the incident shock $\mathbf{S}_I(t)$ at time t. Similarily, we let $J_R(t)$ be the set of all points belonging to

the reflected shock $\mathbf{S}_R(t)$. Each point is propagated using the two-step leap-frog time marching scheme

$$\mathbf{x}_i(t+\Delta t) = \mathbf{x}_i(t-\Delta t) + 2\Delta t\, M_i(t)\, \mathbf{n}_i(t), \qquad i = 1,\ldots,N, \tag{5.3.1}$$

where $t = n\Delta t$, $n = 0,\ldots,T/\Delta t$. The shockfront normal $\mathbf{n}_i(t)$ in (5.3.1) is known trivially for all points in $J_I(t)$. For the points in $J_R(t)$, we find $\mathbf{n}_i(t)$ by differentiating two cubic splines fitted to the data $\big(s_j(t), x_j(t)\big)$ and $\big(s_j(t), y_j(t)\big)$, $j \in J_R(t)$. We determine the Mach number in (5.3.1) by solving the discrete A-M relation

$$\frac{A_i(t)}{A_i(0)} = k_i \frac{f\big(M_i(t)\big)}{f\big(M_0\big)} \qquad \text{for } i = 1,\ldots,N, \tag{5.3.2}$$

where k_i is the exact value of $k(\beta)$ for each point on the shockfront determined using (5.2.6). The approximate ray tube area $A_i(t)$ is given by (2.3.7).

As each point on $\mathbf{S}_I$ meets the wall, a numerical procedure is needed to transfer the points to $\mathbf{S}_R$. The numerical procedure developed to perform this transfer is shown in figure 5.4. In general, the point $\mathbf{x}_i$ meets the wall at a time t_i^* between time steps t and $t+\Delta t$ as shown in figure 5.4a. The time t_i^* is known initially and is given by

$$t_i^* = \frac{x_i(0) - x_w\big(y_i(0)\big)}{M_I}. \tag{5.3.3}$$

The angle between $\mathbf{n}_i$ and the tangent to the wall is also known initially using (5.2.2). For $\mathbf{x}_i$, we have

$$\omega_i = \tan^{-1}\left(\frac{dx_w}{dy}\right)\bigg|_{y=y_i(0)}. \tag{5.3.4}$$

The incident Mach number is constant along $\mathbf{S}_I$. The Mach number and ray inclination angle after reflection may be found using the regular reflection conditions (5.2.3) and (5.2.4). The point $\mathbf{x}_i'(t+\Delta t)$ is moved a distance $(t+\Delta t - t_i^*)M_R$ from the reflection point along its reflected ray as shown in figure 5.4b. This

procedure transfers the point to $\mathbf{S}_R$. A fictitious point $\mathbf{x}_i'(t)$ is positioned a distance $(t_i^* - t)M_R$ behind the wall, which provides the second point required by the two-step leap-frog time marching scheme.

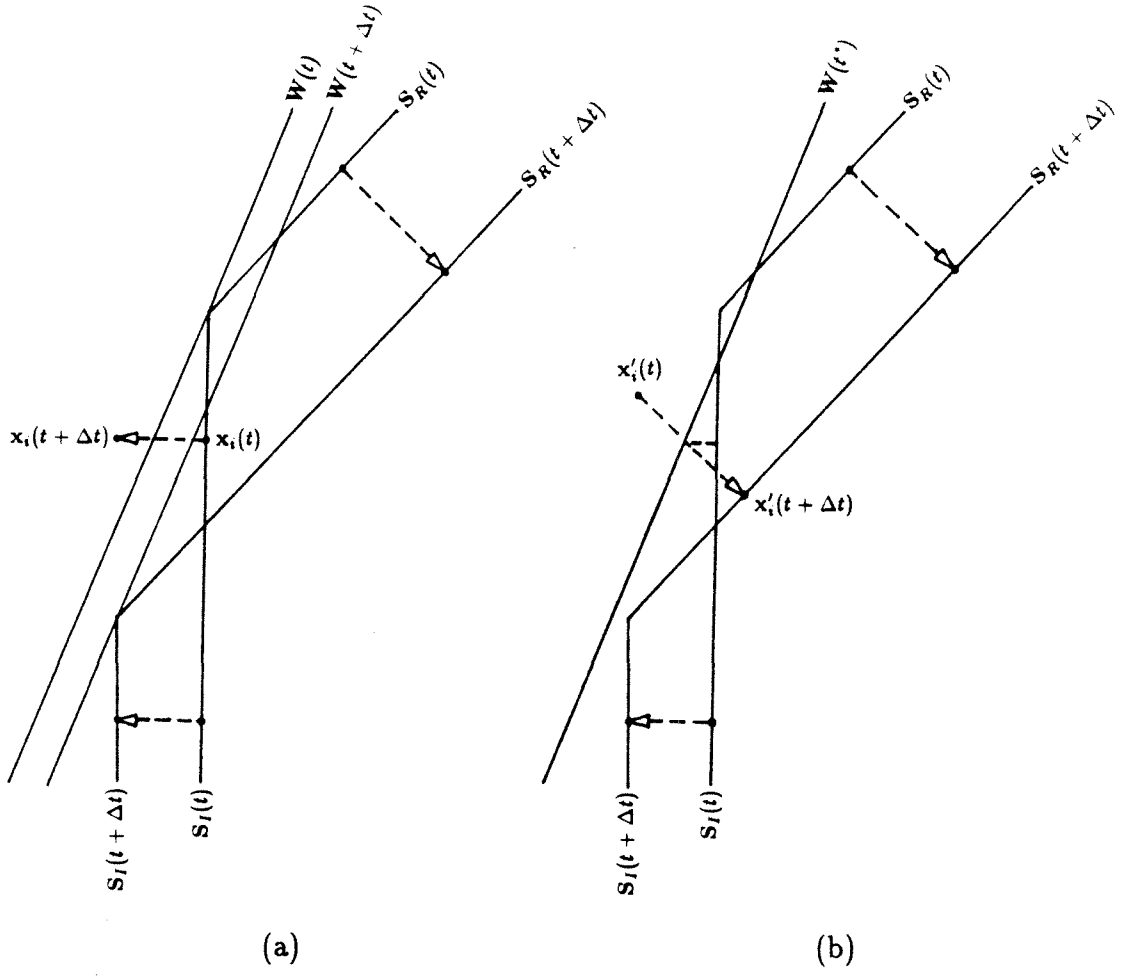

FIGURE 5.4. Numerical reflection: (a) point $\mathbf{x}_i(t + \Delta t)$ passes the reflector; (b) point $\mathbf{x}_i'(t + \Delta t)$ is tranferred to $\mathbf{S}_R$ and a fictitious point $\mathbf{x}_i'(t)$ is added.

We note that for a planar wall, the numerical scheme calculates the planar reflected shock predicted by regular reflection exactly. This fact is useful in testing for errors in the computer code before moving on to the desired calculations for curved walls.

5.4 Shock Reflection from a Parabolic Reflector

We consider the specific problem of a planar shock wave reflected from a parabolic reflector. The motion of the incident and reflected shocks are calculated using the numerical scheme presented in section 5.3. We are primarily interested in determining how well the focusing shockfronts calculated using the approximate theory predict the actual shocks. This determination will be made by comparing our results with experimental data obtained by Sturtevant & Kulkarny [1976] for similar initial shock strengths and reflector geometries.

The particular reflector geometry used for all the calculations in this section is given by

$$x_w(y) = \frac{1}{4R} \begin{cases} y^2, & \text{for } |y| < 1; \\ 1, & \text{for } |y| > 1, \end{cases} \tag{5.4.1}$$

where $x = R$ is the focus point predicted by geometrical acoustics. For $R = .596$, the reflector geometry in (5.4.1) corresponds to reflector number 1 with flat end baffles used by Sturtevant & Kulkarny. We display this reflector geometry in each shockfront plot for reference. The slope of the reflector given by (5.4.1) is discontinuous at $y = \pm 1$. In order to calculate the reflection conditions in the numerical scheme, we require a unique value of dx_w/dy at each point on the reflector surface. This problem is resolved by inserting an small circular arc (with a radius $\approx .01$) into the reflector surface at each corner.

In figure 5.5a, we illustrate the reflection process for an incident shock with $M_I = 1.1$. The incident shockfront is planar and is located at $x = .5$ initially. As the incident shock moves to the left, it meets the reflector surface and reflects according to the conditions given by regular reflection. The reflected shockfront is curved and travels to the right. In the last time frame, the shock has completed its interaction with the reflector and the subsequent motion of the reflected shock

can be determined entirely by geometrical shock dynamics. The views shown in figure 5.5a are typical of the reflection process for weak incident shocks.

A plot of the reflected shockfront as it just leaves the reflector surface is provided in figure 5.5b (solid curve). This shockfront is the same front shown in the last time frame in figure 5.5a. It is interesting to compare the reflected shockfront with the initial shockfront given by profile 2 (see figure 2.16 in section 2.4). The dashed curve in figure 5.5b is profile 2 with $\theta_c = 80°$ and $b/a = 1$. Profile 2 (with $b/a = 1$) is the reflected shockfront given by geometrical acoustics, which is a good first approximation to the actual reflected shock for weak incident shocks. In section 2.4, we argued that the actual reflected shockfront is flatter than the front given by geometrical acoustics. This is primarily due to the fact that points along the incident shock reflect off the reflector at different times and then travel back into the moving gas behind the incident shock. The additional parameter b/a for profile 2 was introduced to model the flattening of the actual reflected front.

Both shapes shown in figure 5.5b are approximations to the actual reflected shock wave. The shockfront calculated using the numerical scheme of section 5.3 (solid curve) is the better approximation for the following reasons. Normal shock reflection is produced by the top flat portion of the reflector and is given exactly by the solid curve. The middle section of the solid curve is the reflected front from the corner of the reflector. It has a larger radius of curvature than profile 2, which is more realistic since it is expanding and thus it is traveling more slowly than its neighboring sections. We see that both curves give a similar approximation for the portion of the shockfront near the axis of symmetry.

The reflected shock has a variable shock strength. We plot the Mach number of the reflected shock versus the distance in the y-direction away from the axis of symmetry in figure 5.6. The Mach number is measured relative to the moving gas behind the incident shock. The dashed line at $M = 1.13$ is the Mach number given

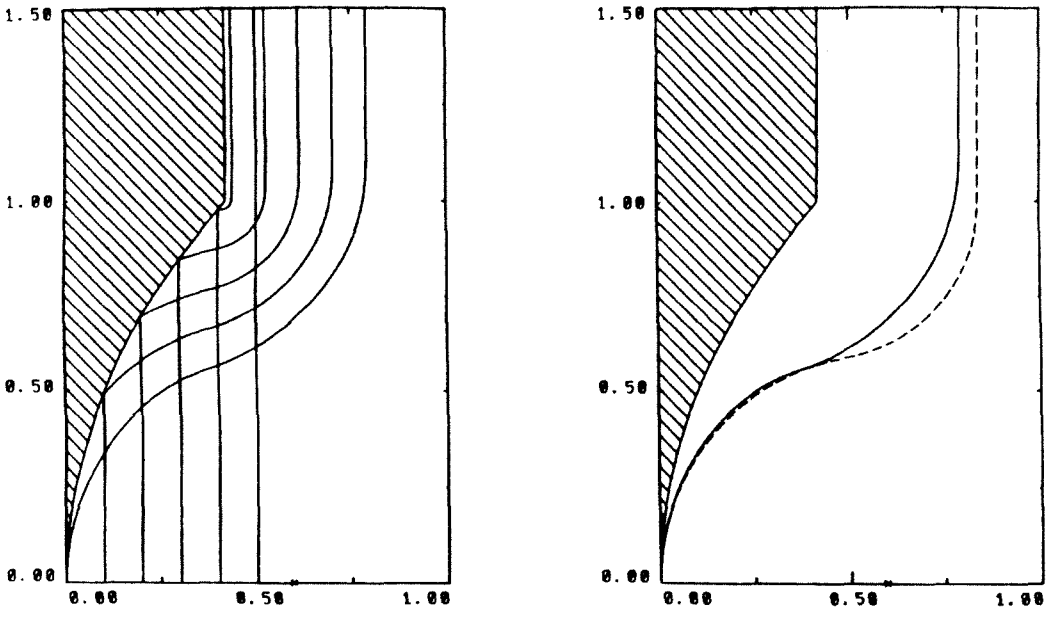

FIGURE 5.5. Shock wave reflection from a parabolic reflector, $M_0 = 1.1$ and $R = .596$: (a) Successive shockfronts; (b) Comparison with profile 2 for $b/a = 1$ (dashed curve).

by normal reflection. In this plot, we can easily identify three principal sections of the reflected front. The top section of the shockfront for which M = constant = 1.13 is given by normal reflection from the flat portion of the reflector. The decreased Mach number along the reflected front for y roughly between 0.5 and 1.1 is a result of the reflection from the corner of the reflector. The section of the shockfront where $M > 1.13$ is given by the reflection from the parabolic portion of the reflector. At $y = 0$, $dx_w/dy = 0$, and we recover $M = 1.13$ as expected. As y increases away from the axis of symmetry, dx_w/dy also increases. This effect gives an increased reflected Mach number as predicted by regular reflection.

One of most interesting quantitative results obtained from the focusing calculations is the Mach number of the shockfront on the axis of symmetry. This

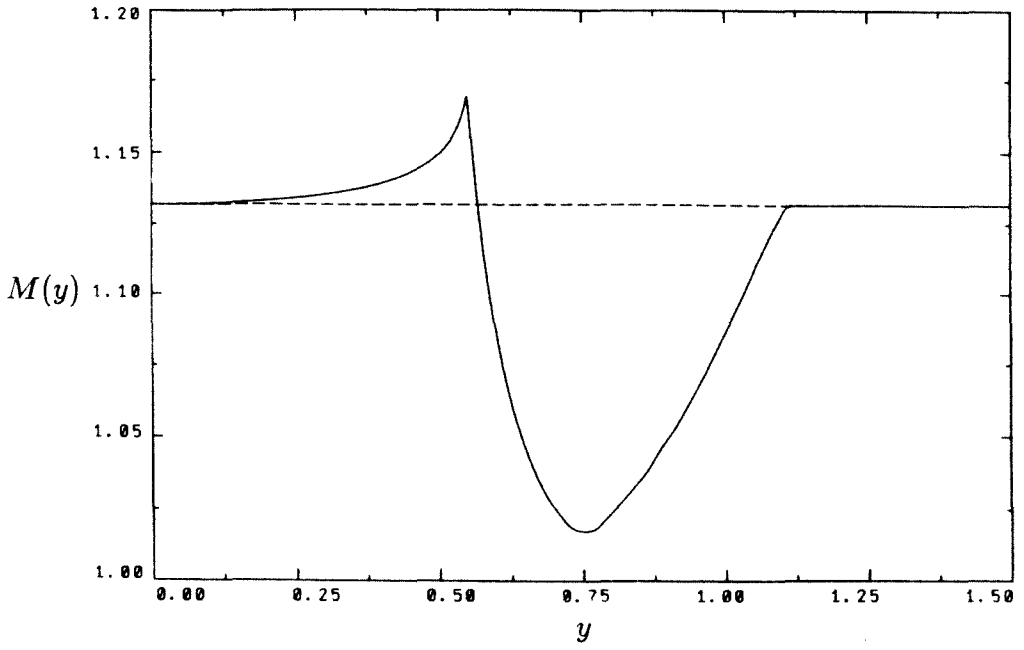

FIGURE 5.6. Local Mach number along the shockfront versus distance in the y-direction measured away from the axis of symmetry for $M_0 = 1.1$. For normal reflection, $M = 1.13$ (dashed line).

information yields the pressure jump across the shock and, in particular, the maximum pressure jump (or peak Mach number) at the focus. We find the relative pressure jump σ using

$$\sigma \equiv \frac{z(M)}{z(M_R)}, \qquad \text{where} \qquad z(M) = 1 + \frac{2\gamma}{\gamma+1}(M^2 - 1) \tag{5.4.2}$$

and M_R is the Mach number of the reflected shock for normal reflection. The reflected Mach number is found using the normal shock relations and is given by

$$\begin{aligned} M_R &= \frac{\gamma+1}{4}M_1 + \left\{ \left(\frac{\gamma+1}{4}\right)^2 M_1^2 + \left(\frac{a_1}{a_0}\right)^2 \right\}^{1/2}, \\ &\approx M_I + \frac{2(\gamma-1)}{\gamma+1}(M_I - 1), \end{aligned} \tag{5.4.3}$$

where a_1/a_0 is the ratio of the sound speeds on either side of the incident shock. The approximation in (5.4.3) is valid for weak incident shocks. The relative pressure jump defined in (5.4.2) is the same as that used by Sturtevant & Kulkarny

except for possibly a factor of a_1/a_0. Since $a_1/a_0 \approx 1$ for weak shocks, this factor is negligible.

In figure 5.7, we plot the Mach number ratio M/M_R versus the distance along the axis symmetry measured away from the reflector surface. This distance is normalized by R, so that $x/R = 1$ gives the focus point for geometrical acoustics. The curve for $M_I = 1.03$ is typical for the single shock-shock focus. This type of focus produces a large maximum pressure jump, which we measure to be $\sigma = 5.6$ for $M_I = 1.03$. Sturtevant & Kulkarny report a maximum pressure jump of $\sigma = 4.9$ found experimentally for the same type of focus. However, their value of $\sigma = 4.9$ was obtained for an incident shock with Mach number equal to 1.1. Lower maximum pressure jumps are observed both numerically and experimentally for increased M_I. For $M_I = 1.07$, the peak given by the single shock-shock focus is decreased to a value of $\sigma = 3.3$, and we see the beginning of a second peak for $x/R < 1$. For $M_I = 1.1$ and $M_I = 1.2$, the peak for $x/R < 1$ is the only peak present and is produced by the formation of a Mach stem near the focus. The transition from the single shock-shock focus to the Mach stem focus can be easily detected in this plot of Mach number versus distance along the axis of symmetry.

The motion of the shockfront after reflection is shown in figures 5.8a–d for the four cases considered in the Mach number plot. These pictures are qualitatively similar to the ones displayed for our previous focusing study (section 2.4). However, a closer study of the shockfronts calculated using the improved scheme shows some important features not present in the previous results. The most notable difference is seen in the shockfront curvature in the vicinity of the focus. For $M_I = 1.1$, we observe a flatter profile (larger radius of curvature) for the portion of the shockfront near the axis of symmetry just before the focus. This is the case for the other shockfront plots in figure 5.8 as well. Similar shockfront profiles in the vicinity of the focus are seen experimentally. In the shadowgraphs provided

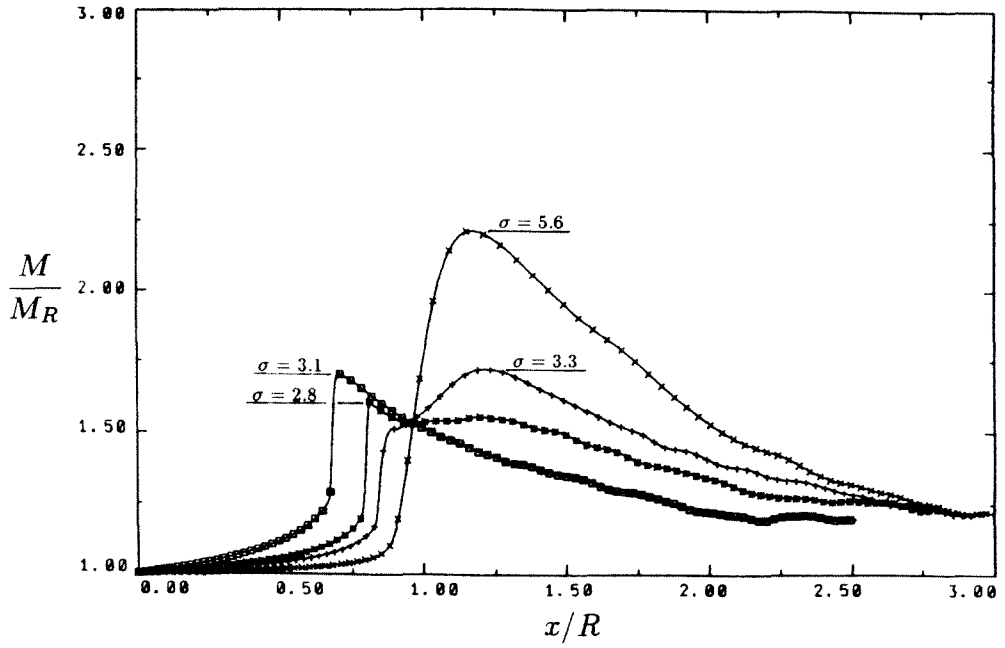

FIGURE 5.7. M/M_R versus distance along the axis of symmetry for $R = .596$: × for $M_0 = 1.03$, + for $M_0 = 1.07$, □ for $M_0 = 1.1$ and ■ for $M_0 = 1.2$.

by Sturtevant & Kulkarny, we note that this portion of the shockfront is bordered by two expansion waves present just behind the shockfront. The expansion waves are generated by the corners of the reflector and move towards one another as the reflected shockfront approaches the focus. These expansion waves are not present in the shock dynamics plots, although their presence is implied by the flattened reflected shockfront near the focus.

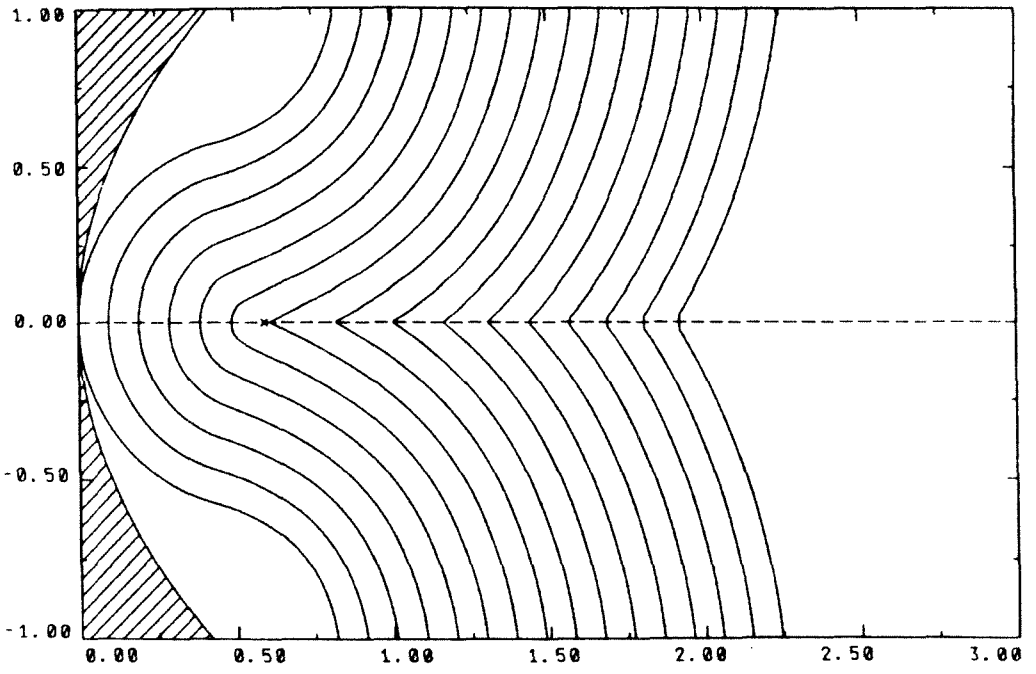

(a) $M_0 = 1.03$

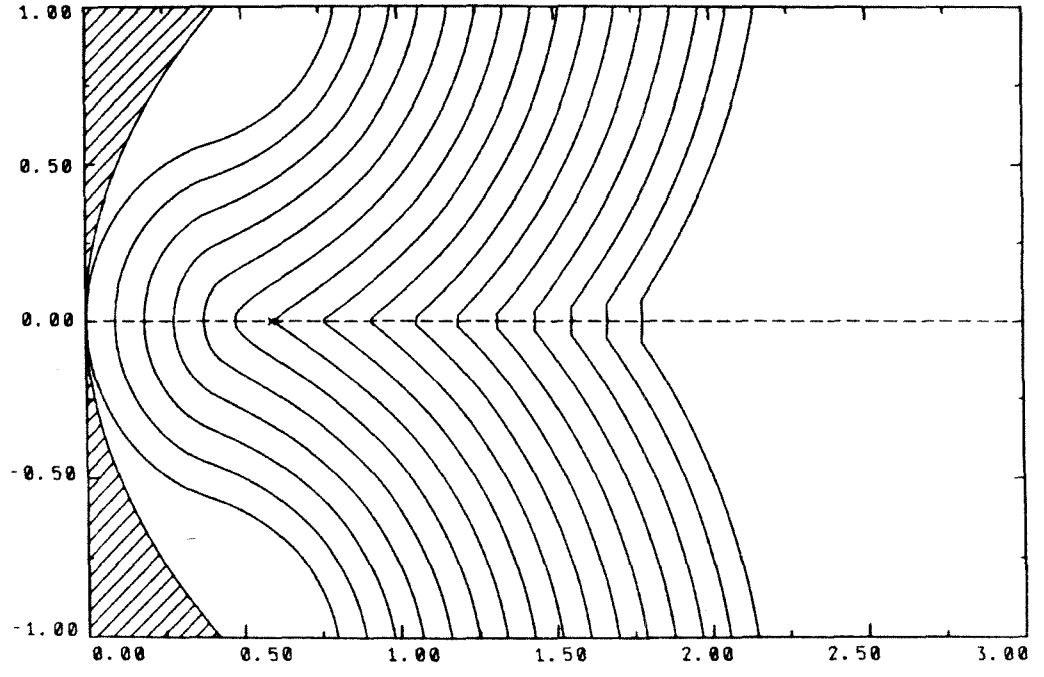

(b) $M_0 = 1.07$

FIGURE 5.8. Shock wave focusing after reflection for $R = .596$.

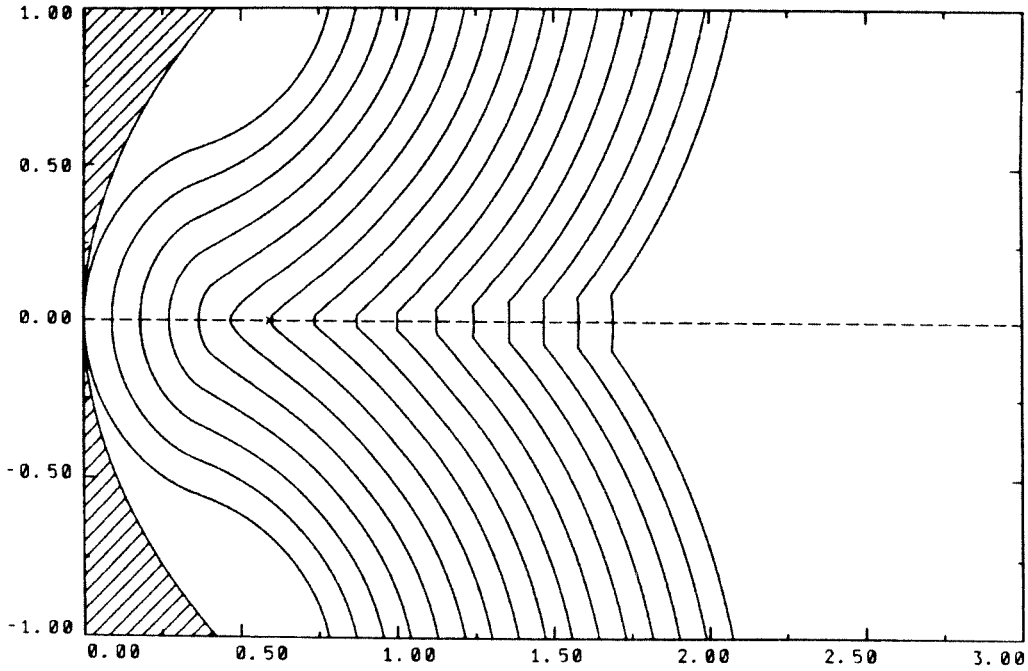

(c) $M_0 = 1.1$

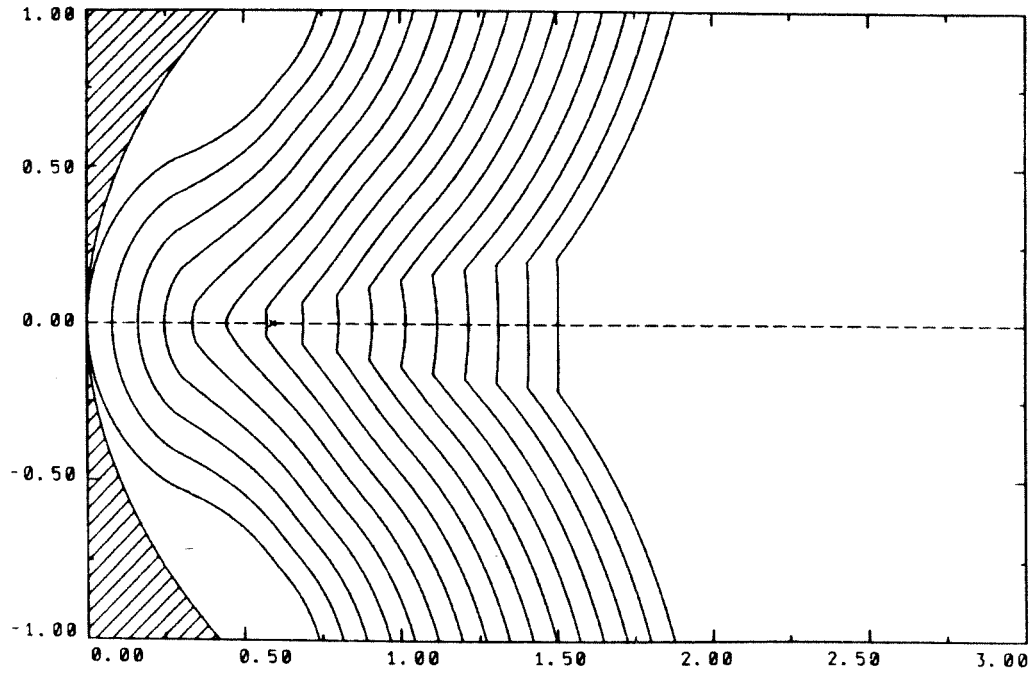

(d) $M_0 = 1.2$

FIGURE 5.8. (cont.). Shock wave focusing after reflection for $R = .596$.

References

A. M. Abd-el-Fattah and L. F. Henderson, *Shock Waves at a Slow-fast Interface*, J. Fluid Mech., **89**, pp. 79–95, 1978.

A. M. Abd-el-Fattah, L. F. Henderson and A. Lozzi, *Precursor Shock Waves at a Slow-fast Interface*, J. Fluid Mech., **76**, pp. 157–176, 1976.

A. E. Bryson and R. W. F. Gross, *Diffraction of Strong Shocks by Cones, Cylinders and Spheres*, J. Fluid Mech., **10**, pp. 1–16, 1961.

C. J. Catherasoo and B. Sturtevant *Shock Dynamics in Non-uniform Media*, J. fluid Mech., **127**, pp. 539–561, 1983.

I.-L. Chern, J. Glimm, O. McBryan, B. Plohr and S. Yaniv, *Front Tracking for Gas Dynamics*, J. Comp. Phys., **62**, pp. 83–110, 1986.

R. Collins and H. T. Chen, *Propagation of a Shock Wave of Arbitrary Strength in Two Half Plains Containing a Free Surface*, J. Comp. Phys., **5**, pp. 415–422, 1970.

R. Collins and H. T. Chen, *Motion of a Shock Wave Through a Non-uniform Media*, Proc. 2nd Int. Conf. on Numerical Methods in Fluid Dynamics (ed. M. Holt), Lecture Notes in Physics, **8**, pp. 264–269, Springer-Verlag: New York, 1971.

D. H. Edwards, P. Fearnley and M. A. Nettleton, *Shock Diffraction in Channels with* 90° *Bends*, J. Fluid Mech., **132**, pp.257–270, 1983.

H. W. Emmons (ed.), *Fundamentals of Gas Dynamics*, High Speed Aerodynamics and Jet Propulsion, Volume III, Princeton University Press: Princeton, 1958.

J. Glimm, E. Isaacson, D. Marchesin and O. McBryan, *Front Tracking for Hyperbolic Systems*, Adv. Applied Math., **2**, pp. 91–119, 1981.

J.-F. Haas and B. Sturtevant, *Interaction of Weak Shock Waves with Cylindrical and Spherical Gas Inhomogeneities*, J. Fluid Mech., 1986, to appear.

W. D. Henshaw, N. F. Smyth and D. W. Schwendeman, *Numerical Shock Propagation Using Geometrical Shock Dynamics*, J. Fluid Mech., 1986, to appear.

R. G. Jahn, *The Refraction of Shock Waves at a Gaseous Interface*, J. Fluid Mech., **1**, pp. 457–489, 1956.

J. W. Miles, *Obliquely Interacting Solitary Waves*, J. Fluid Mech., **79**, pp. 157–169, 1977.

J. W. Miles, *Resonantly Interacting Solitary Waves*, J. Fluid Mech., **79**, pp. 171–179, 1977.

B. Sturtevant and V. A. Kulkarny, *The Focusing of Weak Shock Waves*, J. Fluid Mech., **73**, pp. 651–671, 1976.

G. B. Whitham, *A New Approach to Problems of Shock Dynamics Part I Two-dimensional Problems*, J. Fluid Mech., **2**, pp. 145–171, 1957.

G. B. Whitham, *On The Propagation of Shock Waves Throught Regions of Non-uniform Area or Flow*, J. Fluid Mech., **4**, pp. 337–360, 1958.

G. B. Whitham, *A New Approach to Problems of Shock Dynamics Part II Three-dimensional Problems*, J. Fluid Mech., **5**, pp. 369–386, 1959.

G. B. Whitham, *Linear and Nonlinear Waves*, John Wiley and Sons: New York, 1974.